Evaluation of Bushing Dissipation Rates and Component Flexibility in the Dynamic Analysis of the DN101 Lower Control Arm Mounted on Nonlinear Elastic Bushings

Ragnar Ledesma
Center for Automotive Structural Durability Simulation

Evaluation of Bushing Dissipation Rates and Component Flexibility in the Dynamic Analysis of the DN101 Lower Control Arm Mounted on Nonlinear Elastic Bushings

Ragnar Ledesma
Center for Automotive Structural Durability Simulation
The University of Michigan
2216 G.G. Brown
Ann Arbor, MI 48109-2125

Abstract

This report contains a 2-part study on the DN101 lower control arm mounted on bushings which are modeled as nonlinear elastic forces in parallel with viscous dampers. The first part of this study describes the effect of the linear viscous bushing damping coefficient on the dynamic response of the rigid lower control arm mounted on nonlinear elastic bushings. The results of the study indicate that the linear viscous damping coefficient has a significant effect on the peak amplitudes of the dynamic response, and the proper selection of linear viscous damping coefficients is therefore important in dynamic loads prediction for subsequent durability studies. The second part of the study examines the capability and limitations of ADAMS/FEA in modeling component flexibility in the context of dynamic load prediction for subsequent durability analysis. The results of the study indicate that ADAMS/FEA does not correctly capture the effects of component flexibility in the dynamic analysis of the DN101 lower control arm mounted on bushings. The limitations of ADAMS/FEA are pointed out and recommendations for the best approach in implementing ADAMS/FEA are made.

1. Introduction

This report describes a 2-part study conducted at the Ford Center for Automotive Structural Durability Simulation. The first part of this report deals with the influence of linear viscous damping coefficients on the dynamic response of vehicle suspension system components that are supported by nonlinear elastic bushings. The motivation behind this study came from questions asked by Ford engineers on what should be the correct damping values to be used in modeling bushings with nonlinear elastic springs and linear viscous dampers. The second part of this report examines the adequacy or inadequacy of ADAMS/FEA in modeling flexible bodies in the dynamic analysis of flexible multibody systems. The findings of this study lead to the conclusion that the methods presently used in implementing ADAMS/FEA do not give correct results for the dynamic analysis of flexible bodies. The source of the errors are traced to the use of the discrete mass method of modeling flexible bodies, and a simple method for making the best use of ADAMS/FEA is proposed. The studies are undertaken using a very simple platform - the DN101 lower control arm supported by nonlinear elastic bushings and subjected to a typical chuckhole road load event. All dynamic anaylses are performed using the multibody dynamics code ADAMS.

1.1 *Description of the DN101 LCA - Bushing System*

The lower control arm (LCA) shown in Fig. 1 is a component of the DN101 front suspension system that is designed to transmit the fore-aft and lateral loads from the knuckle to the subframe. Two ends of the LCA are attached to the subframe through two bushings, namely, the front bushing and the rear bushing. The third end is attached to the knuckle through a ball joint (spherical joint). The geometry of the LCA is designed such that the loads in the fore-aft direction are transmitted from the knuckle to the subframe primarily through the front arm while the loads in the lateral direction are transmitted from the knuckle to the subframe primarily through the rear arm. In ADAMS terminology, a rigid body model of the LCA is represented by a *PART* and the nonlinear elastic bushings that are supporting the LCA are represented by *GFORCES*. The front and rear bushings are represented by three uncoupled force components, each of which are modeled by a nonlinear elastic spring and a linear viscous damper in parallel. The nonlinear elastic spring rates are based on the force-displacement curves obtained from separate quasi-static bushing tests in the axial and radial directions. The quasi-static spring rates for the front and rear bushings are shown in Figs. 2 and 3, respectively. The linear viscous damping

values, on the other hand, take on a range of values in order to study the effect of bushing damping on the dynamic response of the rigid LCA-bushing system to a set of prescribed loads.

1.2 Prescribed Ball Joint Loads and Displacements

In this study, the LCA-bushing system is subjected to a set of prescribed loads and displacements that have been obtained from road tests simulating a chuckhole event. The prescribed loads are the fore-aft and lateral loads applied at the ball joint, and the prescribed displacement is the vertical displacement of the ball joint. The prescribed load in the fore-aft and lateral directions are shown in Figs. 4 and 5, respectively, whereas the prescribed vertical displacement of the ball joint is shown in Fig. 6. With the prescribed loads and displacements applied to the LCA-bushing system, the dynamic response of the system is simulated with the bushing attachments fixed. The results of the simulation are then quantified through the bushing displacements, bushing forces, ball joint displacements in the fore-aft and lateral directions, and ball joint reaction in the vertical direction.

2. Influence of Bushing Damping Coefficient

It is well known that the energy dissipated by a linear viscous damper is proportional to the frequency of excitation. This means that the proper values for the damping coefficients should be chosen such that the amount of energy dissipated by the analytical model should closely approximate the real system in the frequency range of interest. This also means that a set of damping values that is chosen to suit a particular event may not be adequate for another event if the two events have very different frequency contents.

In order to study the effect of the viscous damping coefficient on the dynamic response of the LCA-bushing system, the linear viscous dampers in each of the bushing axes were arbitrarily assigned uniform ratios of 0.01, 0.001, and 0.0001 relative to the corresponding linearized (nominal) stiffness of the elastic spring that represents the bushing. The linearized spring stiffnesses in turn are computed from the nonlinear elastic spring rates through a linear regression (least squares) technique. The LCA-bushing system is then repeatedly simulated with bushing damping ratios as given above and subject to the prescribed loads and displacements described in the preceding section. The results of the dynamic analyses are presented in the Figs. 7 through 12 in the form of time histories and frequency content of bushing deformation, bushing forces, and ball joint displacements.

Fig. 7 shows the deformation of the front bushing along the local x-axis which is the radial axis directed along the length of the forward arm of the LCA. From this figure, we observe that the three damping models predict the same magnitude for the first peak in the chuckhole event but do not agree on the succeeding peaks. Furthermore, we also observe that the bushing model with higher damping coefficients do not capture the high frequency vibration modes that are present in the bushing model with lower damping coefficients. These differences in the frequency content of the front bushing displacement are made clearer in Fig. 8 which shows the Fourier transforms of the time history plots of Fig. 7. Fig. 9 shows the front bushing's radial force along the local x-axis, and Fig. 10 shows the corresponding Fourier transforms of the front bushing forces. Again, we observe that the bushing model with higher a damping coefficient will predict a smaller response in the high frequency regimes. Figs. 11 and 12 show the time history and the Fourier transform, respectively, of the ball joint displacement along the fore-aft direction, again showing the same trend observed earlier. A summary of the simulation results showing the maximum positive, maximum negative, and peak-to-peak response of the LCA-bushing system with damping ratios of 0.01, 0.001, and 0.0001 relative to nominal stiffness are given in Table 1, Table 2, and Table 3, respectively.

By comparing the tabulated peak-to-peak values of the various components of the dynamic response, we can conclude that the value of the viscous damping coefficient plays a significant role in the dynamic response of the LCA-bushing system. In particular, correlation with experiments wherein the bushing is subjected to harmonic loads indicate that the equivalent linear viscous damping coefficient should be in the range of 0.0001 to 0.001 relative to the corresponding nominal bushing stiffness for frequency ranges of 10 Hz to 30 Hz. Subsequently, we constructed a model of the LCA-bushing system with bushing damping coefficients tuned so that the energy dissipation approximately matched those of the tests of the bushing under harmonic loads in the 10 Hz to 30 Hz frequency range. This rigid LCA-bushing model was simulated to undergo the prescribed road load event and the results of the simulation are summarized in Table 4.

3. Component Flexibility Using ADAMS/FEA

The structural flexibility of the LCA is considered by creating a finite element model of the LCA using NASTRAN. The finite element model contains 1338 nodes and consists mainly of shell elements and beam elements. In order to reduce the number of degrees of freedom, we employ a static condensation (Guyan reduction) procedure to create a superelement with

a manageable number of master nodes. In this study, we consider a 9-master node superelement representation of the flexible LCA. The 9-master node superelement consists of 1 master node located at the front bushing attachment point, 1 master node at the rear bushing attachment point, 1 master node at the ball joint, and 6 master nodes distributed throughout the interior of the structure.

3.1 ADAMS/FEA Representation of Component Flexibility

In an ADAMS model of a multibody system, all bodies are considered rigid. If the structural flexibility of a component is assumed to be important, the structural flexibility of the component can be considered by dividing the deformable body into a set of discrete rigid masses which are interconnected by linear elastic springs (also known as the discrete mass method). By using this method of representing component flexibility, the superelement model obtained from the static condensation procedure in NASTRAN can be transformed into an ADAMS model which contains a set of discrete masses equal to the number of master nodes in the superelement model. The spring constants of the linear elastic springs which interconnect the discrete masses are obtained directly from the stiffness matrix of the superelement.

There are two methods normally used in modeling the mass distribution in the flexible body in ADAMS/FEA. In the first method, (the so-called default mass lumping) the masses of each of the discrete masses are set proportional to the sum of the corresponding rows (or columns) in the superelement mass matrix while maintaining the constraint that the sum of the discrete masses is equal to the total mass of the rigid body, whereas the rotational inertia of each of the discrete masses is set arbitrarily by the user. In the second method (also called the concentrated mass method), the structure is broken up into substructures. The number of substructures is set equal to the desired number of discrete masses, and the masses and rotational inertia of each substructure is determined by using any solid modeling software or the so-called Grid Point Generator in NASTRAN. The discrete mass methods outlined above are deficient in the sense that the inertial forces due to component flexibility are not considered. These methods are adequate if the inertial forces due to flexibility alone are small compared to the inertial forces acting on the reference rigid body (i.e., dynamic flexibility effects are neglected). The effect of component flexibility are therefore considered only through the spring forces (i.e., static flexibility effects).

As mentioned earlier, the spring constants are obtained directly from the superelement stiffness matrix. The spring forces that act between the discrete masses can be evaluated in two ways. In the first method, a single kinematic frame of reference (KRF) is used in order to determine the relative displacements of the master nodes. These relative displacements pre-multiplied by the superelement stiffness matrix gives the spring forces acting between the discrete masses. In the second method, multiple kinematic reference frames (one for each substructure) are used in determining the relative displacements of the master nodes. Again, the spring forces acting between the discrete masses contained in a particular substructure are determined by pre-multiplying the relative displacements with the superelement stiffness matrix for that substructure. This method supposedly takes into consideration the large displacement effects in determining the spring forces between the discrete masses.

3.2. Simulation Results and Discussion

In order to study the adequacy of ADAMS/FEA in performing dynamic analyses of flexible multibody components, we created four models of the flexible LCA based on the 9-master node superelement obtained from NASTRAN, namely: a) default mass lumping with 1 KRF; b) default mass lumping with 3 KRF's; c) concentrated mass approach with 1 KRF; and d) concentrated mass approach with 3 KRF's. For the default mass lumping models, the rotational moments of inertia were arbitrarily set to 100 times the corresponding discrete masses. For the concentrated mass approach, the flexible LCA structure was divided into three substructures and concentrated masses and inertia properties were determined using the Grid Point Generator in NASTRAN.

3.2.1. Effect of Choice of Single Kinematic Reference Frame (KRF)

In ADAMS/FEA, the user must specify which among the master nodes in the structure or substructure is the kinematic reference frame (KRF). In order to determine if the choice of the KRF has any effect on the results of the dynamic analysis, we constructed two models of the flexible LCA, both using default mass lumping as described above. One model had its KRF near the ball joint (KRF at node 356) and the other model had its KRF near the middle of the front arm (node 121). Simulation results for the two models are shown in Figures 13 through 27, and the peak-to-peak values are summarized in Table 5. The results show that the dynamic response is dependent on the choice of the KRF, and the difference in responses for different choices of KRF's are significant. In particular, the peak in the

fore-aft displacement of the ball joint differ by 18% of the average of the two peaks between the two models. This is due to the fact that the spring forces are computed as a product of the superelement stiffness matrix and the relative displacements of the discrete masses. The latter are measured relative to the KRF, and are therefore dependent on the orientation of the KRF. As shown in Figures 28 through 30, the difference between the orientations of the two KRF's are significant, hence the corresponding spring forces will also be proportionately different.

3.2.2. Single Kinematic Reference Frame vs. Multiple Kinematic Reference Frames

To study the differences in the response when using a single KRF as opposed to using multiple KRF's, we compared the simulation results of the 1 KRF model against those of the 3 KRF model, using both default mass lumping and concentrated mass approaches. Time history plots of the dynamic response using the default mass lumping method are shown in Figures 31 through 48, while the time history plots of the dynamic response using the concentrated mass approach are shown in Figures 49 through 66. The peak-to-peak values for the default mass lumping are summarized in Table 6 while the peak-to-peak values for the concentrated mass approach are summarized in Table 7. The simulation results indicate that using multiple KRF's gives erroneous results rather than the expected improvement in accuracy. In particular, when the default mass lumping procedure is used, the force in the axial direction of the front bushing (local z-axis) has a peak-to-peak response is 0.3 kN for the analysis based on the use of a single kinematic reference frame, while the corresponding value for the analysis based on the use of multiple kinematic reference frames is 13.2 kN - a change of more than 20 times the former value. Based on the analysis of the rigid LCA, we can conclude that the results of the analysis using multiple kinematic reference frames are erroneous. These errors can be attributed to the incorrect implementation of the co-rotational stiffness in ADAMS/FEA. In the present implementation, the spring forces in each substructure are computed as the product of a constant stiffness matrix and a relative displacement vector. The former is measured with respect to the global coordinate system in NASTRAN which becomes a floating reference frame in the multibody dynamics code. The relative displacement vector, on the other hand, is measured relative to the kinematic reference frame which is fixed to one of the discrete masses. If the rotation of the kinematic reference frame is significantly different from that of the aforementioned floating reference frame, erroneous spring forces will be result from the present implementation. We can observe that this indeed occurs in the default mass lumping model with 3 KRF's (Figures 46 through 48) and also with the concentrated mass

model with 3 KRF's (Figures 64 through 66). These figures show that the orientations of the kinematic reference frames differ significantly, which implies that the kinematic reference frames experience a finite rotation relative to the floating reference frame on which the superelement stiffness matrices are based on.

3.2.3. Default Mass Lumping vs. Concentrated Mass Approach

The effect of the mass distribution procedure can be examined from the time history plots of the previous section or from the summary of peak-to-peak values of the dynamic responses given in Table 8, which shows a comparison of the peak-to-peak responses for the two different methods of mass distribution. From these results, we can conclude that the effect of the mass distribution will also affect the dynamic response of the flexible multibody system. In order to obtain a better understanding of the effect of mass distribution, we show in Table 9 the natural frequencies of the flexible LCA structure with free boundary conditions for four models, namely: a) full finite element model; b) 9-master node superelement with consistent masses; c) 9-master node model with concentrated masses for each of the three substructures; and d) 9-discrete mass model using ADAMS/FEA default mass lumping. From Table 9, we can conclude that the discrete mass formulation of the flexible multibody dynamics problem, using either the ADAMS/FEA default mass lumping procedure or the concentrated mass approach, leads to a poor estimate of the system natural frequencies.

3.3. Possible Remedies to the Deficiencies of ADAMS/FEA

We have observed in the previous section that ADAMS/FEA gives erroneous results in the dynamic analysis of flexible multibody components. We have pointed out that the errors in the simulation results are due to the fact that ADAMS/FEA computes the elastic forces from

$$P = K\,d$$

where the stiffness matrix K is based on the global coordinate system in NASTRAN, which becomes a floating reference frame in ADAMS, and the deformation vector d is measured with respect to a kinematic reference frame which is fixed to one of the discrete masses. If there is a finite rotation of the kinematic reference frame with respect to the floating reference frame, erroneous spring forces are obtained from the above equation. A possible remedy to this problem is to implement correctly the co-rotated elastic forces,

which means that we need to perform a similar transformation on the stiffness matrix so that the co-rotational stiffness matrix, the elastic force vector, and the deformation vector are all based on the kinematic reference frame, *i.e.*,

$$P = [A^T \, K \, A] \, d$$

where A is the rotation transformation matrix from the kinematic reference frame to floating reference frame. The main drawback to this approach is that when the flexible body has been divided into discrete masses, the reference rigid body and the associated floating reference frame no longer exist as entities in the ADAMS model, and therefore it is not possible to compute for the transformation matrix A unless the user simultaneously performs a dynamic analysis of a similar model with the reference rigid body in place of the flexible body. This is possible for small problems but not practical for large problems such as full vehicle suspension systems.

A better solution than the one outlined above is to lump the rigid body mass and inertia properties at a master node located at the center of gravity of the undeformed flexible body, and locate the remaining master nodes at the attachment points of the flexible body. The master nodes at the attachment points will have very small fictitious masses and very small fictitious moments of inertia. The superelement stiffness matrix that represents the spring coefficients between the master nodes is obtained from NASTRAN as usual. The kinematic reference frame is then attached to the discrete mass located at the center of gravity of the flexible body. Since this discrete mass has exactly the same mass and rotational inertia properties as the reference rigid body, we would expect the kinematic reference frame to be nearly parallel with the floating reference frame. Hence, the rotation transformation matrix A is approximately equal to the identity matrix, and ADAMS/FEA can be implemented without introducing any changes in the software. One difficulty in implementing this approach occurs in the case where the center of gravity of the flexible structure does not lie within the structure. In this case, the analyst must resort to an *ad hoc* procedure of creating the center of gravity node and connecting this node to some selected nodes within the structure in a manner that does not significantly alter the stiffness characteristics of the structure. Another disadvantage of this approach, in terms of practical implementation of ADAMS/FEA, is that the introduction of small fictitious masses and small mass moments of inertia at the attachment points results in spurious high frequency responses in the dynamic analysis. These high frequency components in the dynamic response causes the numerical integrator to take very small time steps, and the computation time therefore

increases. We constructed a flexible model of the LCA consisting of a master node having the same mass and inertia properties as the reference rigid body and located at the center of gravity of the undeformed LCA, and three other master nodes located at the attachment points, *i.e.*, front bushing attachment point, rear bushing attachment point, and ball joint. The results of the dynamic analysis are compared with those of the rigid LCA in Figures 67 through 81, and a comparison of the peak-to-peak values are summarized in Table 10. We observe the spurious high frequency response in the flexible LCA model (*e.g.*, vertical reaction force at the ball joint) because of the necessity of introducing small fictitious masses at the attachment points. However, the magnitude of the spurious high frequency response is small compared to the more significant force components (*e.g.*, radial force along the front bushing's local x-axis) where the dynamic response of the flexible LCA model is almost identical to that of the rigid LCA model, and therefore the introduction of small fictitious masses should not affect the fatigue life prediction of the component. As expected, because of the presence of high frequency response in the dynamic response, the computation time for the dynamic analysis of this flexible model has increased tremendously by 523% compared to the computation time of the rigid body model.

4. Summary and Conclusions

We have conducted a 2-part study on the DN101 LCA-bushing system. In the first part of the study, we investigated the influence of the linear viscous damping coefficient on the rigid LCA supported by nonlinear elastic bushings. Simulation results indicate that the linear viscous damping coefficient has a significant effect on the peak amplitudes of the dynamic response (up to 10% change in the peak-to-peak response for an order of magnitude change in the damping coefficients). It has been pointed out that the proper values of the linear viscous damping coefficients depend on the frequency of the excitation, since a linear viscous damper dissipates energy in an amount that is proportional to the excitation frequency. In particular, correlation with tests on bushings under harmonic loads in the 10 Hz to 30 Hz frequency range suggest that the equivalent linear viscous damping coefficients for the LCA bushings should lie from 0.0001 to 0.001 of the nominal bushing stiffness.

In the second part of the study, we investigated the capability of ADAMS/FEA in modeling component flexibility in the dynamic response of the LCA supported by nonlinear elastic springs. We have pointed out the deficiencies of the discrete mass method used by ADAMS/FEA in modeling component flexibility, and we summarize those deficiencies as

follows. First, it has been shown that the discrete mass approach in modeling flexible components results in incorrect natural frequencies. Second, the discrete mass method does not capture the effects of dynamic flexibility (inertial forces due to component flexibility). Third, the simulation results coming from ADAMS/FEA depend heavily on the choice of the kinematic reference frames whose moments of inertia are not consistent with the finite element model. Fourth, the use of multiple kinematic reference frames (which the developers of ADAMS/FEA have claimed to provide more accurate results) result in even more inaccurate results. We have analyzed the source of the errors in the usual methods of implementing ADAMS/FEA, and we have recommended what we consider to be the best approach in implementing ADAMS/FEA for the dynamic analysis of flexible multibody systems.

	Maximum Positive Dynamic Response	Maximum Negative Dynamic Response	Peak-to-Peak Dynamic Response
Front bush force along local x-axis	20.4 kN	-9.4 kN	29.8 kN
Front bush force along local y-axis	3.3 kN	-2.7 kN	6.0 kN
Front bush force along local z-axis	0.2 kN	-0.4 kN	0.6 kN
Rear bush force along local x-axis	11.7 kN	-14.8 kN	26.5 kN
Rear bush force along local y-axis	0.3 kN	-3.0 kN	3.3 kN
Rear bush force along local z-axis	6.5 kN	-5.1 kN	11.6 kN
Front bush disp. along local x-axis	8.5 mm	-9.6 mm	18.6 mm
Front bush disp. along local y-axis	1.2 mm	-1.7 mm	2.9 mm
Front bush disp. along local z-axis	1.9 mm	-0.4 mm	2.3 mm
Rear bush disp. along local x-axis	1.6 mm	-0.9 mm	2.5 mm
Rear bush disp. along local y-axis	0.5 mm	-0.1 mm	0.6 mm
Rear bush disp. along local z-axis	6.5 mm	-6.5 mm	13.0 mm
Ball joint disp. along fore-aft direction	8.5 mm	-11.7 mm	20.2 mm
Ball joint disp. along lateral direction	0.9 mm	-5.2 mm	6.1 mm
Ball joint vertical reaction force	1.2 kN	-1.4 kN	2.6 kN

Table 1: Simulation Results: Damping ratio = 0.01 of nominal stiffness

	Maximum Positive Dynamic Response	Maximum Negative Dynamic Response	Peak-to-Peak Dynamic Response
Front bush force along local x-axis	21.4 kN	-12.1 kN	33.5 kN
Front bush force along local y-axis	2.2 kN	-2.6 kN	4.8 kN
Front bush force along local z-axis	0.2 kN	-0.3 kN	0.5 kN
Rear bush force along local x-axis	11.6 kN	-15.5 kN	27.1 kN
Rear bush force along local y-axis	0.3 kN	-2.4 kN	2.7 kN
Rear bush force along local z-axis	4.4 kN	-3.3 kN	7.7 kN
Front bush disp. along local x-axis	10.5 mm	-9.8 mm	20.3 mm
Front bush disp. along local y-axis	2.3 mm	-2.0 mm	4.3 mm
Front bush disp. along local z-axis	2.0 mm	-1.1 mm	3.1 mm
Rear bush disp. along local x-axis	2.4 mm	-2.0 mm	4.4 mm
Rear bush disp. along local y-axis	0.5 mm	-0.1 mm	0.6 mm
Rear bush disp. along local z-axis	6.6 mm	-7.7 mm	14.3 mm
Ball joint disp. along fore-aft direction	11.1 mm	-11.9 mm	23.0 mm
Ball joint disp. along lateral direction	1.0 mm	-5.6 mm	6.6 mm
Ball joint vertical reaction force	1.1 kN	-1.4 kN	2.5 kN

Table 2: Simulation Results: Damping ratio = 0.001 of nominal stiffness

	Maximum Positive Dynamic Response	Maximum Negative Dynamic Response	Peak-to-Peak Dynamic Response
Front bush force along local x-axis	21.1 kN	-15.8 kN	36.9 kN
Front bush force along local y-axis	2.4 kN	-2.9 kN	5.3 kN
Front bush force along local z-axis	0.6 kN	-0.6 kN	1.2 kN
Rear bush force along local x-axis	11.6 kN	-16.2 kN	27.8 kN
Rear bush force along local y-axis	1.1 kN	-2.3 kN	3.4 kN
Rear bush force along local z-axis	5.9 kN	-3.3 kN	9.2 kN
Front bush disp. along local x-axis	11.4 mm	-9.8 mm	21.2 mm
Front bush disp. along local y-axis	2.7 mm	-2.2 mm	4.9 mm
Front bush disp. along local z-axis	3.7 mm	-4.0 mm	7.7 mm
Rear bush disp. along local x-axis	2.5 mm	-2.0 mm	4.5 mm
Rear bush disp. along local y-axis	0.5 mm	-0.2 mm	0.7 mm
Rear bush disp. along local z-axis	6.6 mm	-8.7 mm	15.3 mm
Ball joint disp. along fore-aft direction	12.7 mm	-11.6 mm	24.3 mm
Ball joint disp. along lateral direction	0.9 mm	-5.6 mm	6.5 mm
Ball joint vertical reaction force	1.3 kN	-1.3 kN	2.6 kN

Table 3: Simulation Results: Damping ratio = 0.0001 of nominal stiffness

	Maximum Positive Dynamic Response	Maximum Negative Dynamic Response	Peak-to-Peak Dynamic Response
Front bush force along local x-axis	21.2 kN	-15.0 kN	36.2 kN
Front bush force along local y-axis	2.3 kN	-2.8 kN	5.1 kN
Front bush force along local z-axis	0.3 kN	-0.3 kN	0.6 kN
Rear bush force along local x-axis	11.5 kN	-16.1 kN	27.6 kN
Rear bush force along local y-axis	0.4 kN	-0.5 kN	0.9 kN
Rear bush force along local z-axis	5.5 kN	-3.2 kN	8.7 kN
Front bush disp. along local x-axis	11.2 mm	-9.8 mm	21.0 mm
Front bush disp. along local y-axis	2.6 mm	-2.1 mm	4.7 mm
Front bush disp. along local z-axis	1.4 mm	-1.6 mm	3.0 mm
Rear bush disp. along local x-axis	2.5 mm	-2.0 mm	4.5 mm
Rear bush disp. along local y-axis	0.1 mm	-0.1 mm	0.2 mm
Rear bush disp. along local z-axis	6.6 mm	-8.4 mm	15.0 mm
Ball joint disp. along fore-aft direction	12.2 mm	-11.7 mm	23.9 mm
Ball joint disp. along lateral direction	0.9 mm	-5.6 mm	6.5 mm
Ball joint vertical reaction force	1.2 kN	-1.3 kN	2.5 kN

Table 4: Simulation Results: Damping coefficients correlated with experiments (10-30 Hz)

	Kinematic Reference Frame at node 121	Kinematic Reference Frame at node 356
Front bushing force along local x-axis	38.7 kN	36.2 kN
Front bushing force along local y-axis	5.2 kN	5.0 kN
Front bushing force along local z-axis	1.2 kN	0.6 kN
Rear bushing force along local x-axis	27.4 kN	27.8 kN
Rear bushing force along local y-axis	0.8 kN	1.0 kN
Rear bushing force along local z-axis	7.4 kN	9.6 kN
Front bushing disp. along local x-axis	21.5 mm	20.9 mm
Front bushing disp. along local y-axis	4.8 mm	4.6 mm
Front bushing disp. along local z-axis	7.0 mm	3.3 mm
Rear bushing disp. along local x-axis	4.5 mm	4.5 mm
Rear bushing disp. along local y-axis	0.15 mm	0.15 mm
Rear bushing disp. along local z-axis	13.0 mm	14.8 mm
Ball joint disp. along the fore-aft direction	32.7 mm	36.2 mm
Ball joint disp. along the lateral direction	10.5 mm	9.7 mm
Ball joint reaction in the vertical direction	2.6 kN	2.5 kN

Table 5: Peak-to-peak response: effect of location of kinematic reference frame

	Single Kinematic Reference Frame	Multiple Kinematic Reference Frames
Front bushing force along local x-axis	36.2 kN	39.5 kN
Front bushing force along local y-axis	5.0 kN	8.5 kN
Front bushing force along local z-axis	0.6 kN	13.1 kN
Rear bushing force along local x-axis	27.8 kN	29.0 kN
Rear bushing force along local y-axis	1.0 kN	6.2 kN
Rear bushing force along local z-axis	9.6 kN	13.2 kN
Front bushing disp. along local x-axis	20.9 mm	21.7 mm
Front bushing disp. along local y-axis	4.6 mm	7.1 mm
Front bushing disp. along local z-axis	3.3 mm	30.4 mm
Rear bushing disp. along local x-axis	4.5 mm	4.7 mm
Rear bushing disp. along local y-axis	0.15 mm	1.2 mm
Rear bushing disp. along local z-axis	14.8 mm	15.9 mm
Ball joint disp. along the fore-aft direction	36.2 mm	71.4 mm
Ball joint disp. along the lateral direction	9.7 mm	24.0 mm
Ball joint reaction in the vertical direction	2.5 kN	7.2 kN

Table 6: Peak-to-peak response, default mass lumping: single kinematic reference frame vs. multiple kinematic reference frames

	Single Kinematic Reference Frame	Multiple Kinematic Reference Frames
Front bushing force along local x-axis	35.9 kN	45.3 kN
Front bushing force along local y-axis	4.5 kN	5.7 kN
Front bushing force along local z-axis	0.8 kN	8.8 kN
Rear bushing force along local x-axis	27.4 kN	30.0 kN
Rear bushing force along local y-axis	1.2 kN	6.9 kN
Rear bushing force along local z-axis	9.3 kN	9.3 kN
Front bushing disp. along local x-axis	20.8 mm	22.9 mm
Front bushing disp. along local y-axis	4.3 mm	5.3 mm
Front bushing disp. along local z-axis	4.2 mm	28.4 mm
Rear bushing disp. along local x-axis	4.5 mm	4.8 mm
Rear bushing disp. along local y-axis	0.22 mm	1.3 mm
Rear bushing disp. along local z-axis	14.7 mm	14.0 mm
Ball joint disp. along the fore-aft direction	35.5 mm	64.6 mm
Ball joint disp. along the lateral direction	10.2 mm	25.7 mm
Ball joint reaction in the vertical direction	3.0 kN	7.4 kN

Table 7: Peak-to-peak response, concentrated mass approach: single kinematic reference frame vs. multiple kinematic reference frames

	Concentrated Mass Method	Default Mass Lumping Method
Front bushing force along local x-axis	35.9 kN	36.2 kN
Front bushing force along local y-axis	4.5 kN	4.9 kN
Front bushing force along local z-axis	0.8 kN	0.6 kN
Rear bushing force along local x-axis	27.4 kN	27.8 kN
Rear bushing force along local y-axis	1.2 kN	1.0 kN
Rear bushing force along local z-axis	9.3 kN	9.6 kN
Front bushing disp. along local x-axis	20.8 mm	20.8 mm
Front bushing disp. along local y-axis	4.3 mm	4.6 mm
Front bushing disp. along local z-axis	4.2 mm	3.3 mm
Rear bushing disp. along local x-axis	4.5 mm	4.5 mm
Rear bushing disp. along local y-axis	0.22 mm	0.15 mm
Rear bushing disp. along local z-axis	14.7 mm	14.8 mm
Ball joint disp. along the fore-aft direction	35.5 mm	36.2 mm
Ball joint disp. along the lateral direction	10.2 mm	9.7 mm
Ball joint reaction in the vertical direction	3.0 kN	2.5 kN

Table 8: Peak-to-peak response, single kinematic reference frame: concentrated mass approach vs. default mass lumping method

DN101 LCA Mounted on Nonlinear Elastic Bushings

ball joint displacement along the lateral direction
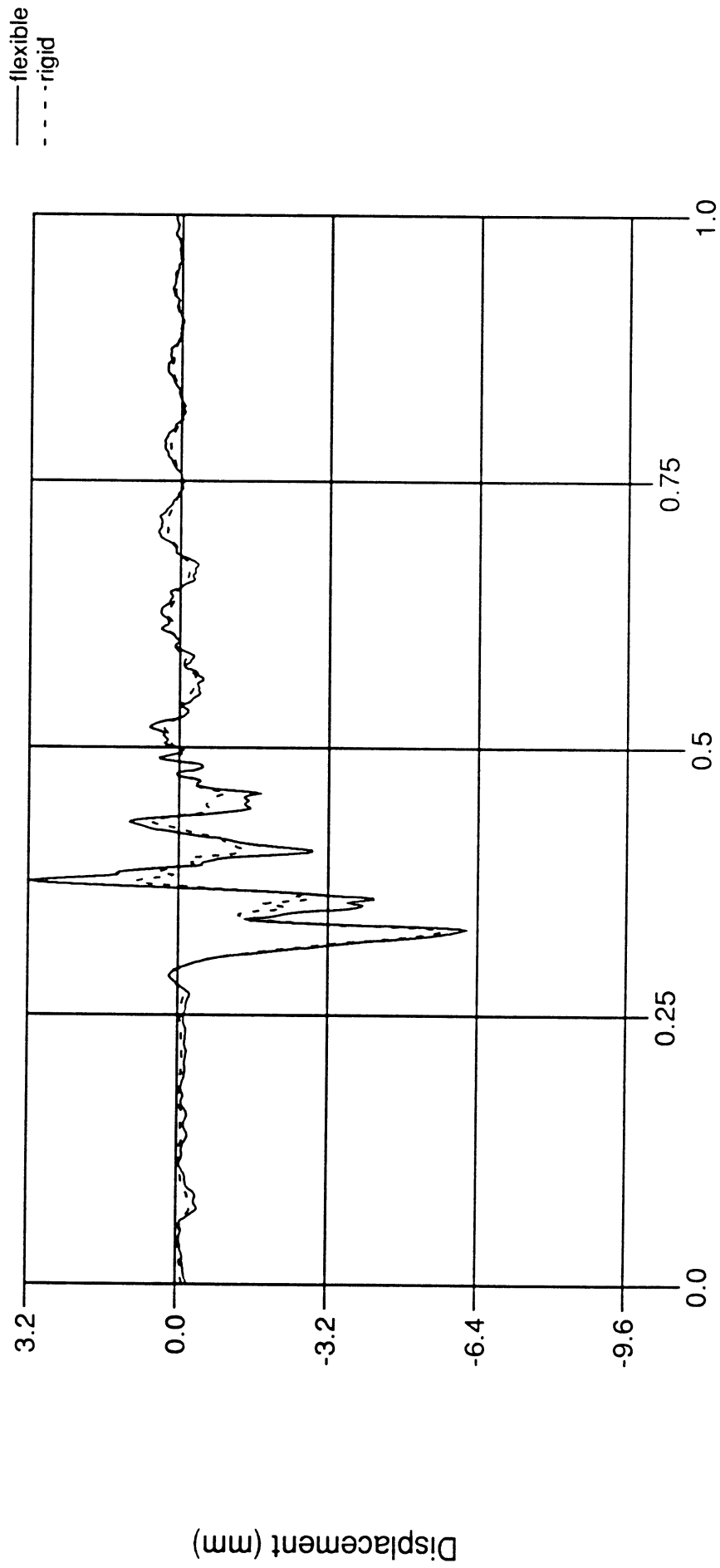
Figure 68

	Rigid LCA Model	Flexible (1-Mass) LCA Model
Front bushing force along local x-axis	36.2 kN	37.7 kN
Front bushing force along local y-axis	5.1 kN	4.5 kN
Front bushing force along local z-axis	0.6 kN	0.5 kN
Rear bushing force along local x-axis	27.6 kN	27.6 kN
Rear bushing force along local y-axis	0.9 kN	1.4 kN
Rear bushing force along local z-axis	8.7 kN	7.0 kN
Front bushing disp. along local x-axis	21.0 mm	21.3 mm
Front bushing disp. along local y-axis	4.7 mm	4.2 mm
Front bushing disp. along local z-axis	3.0 mm	2.4 mm
Rear bushing disp. along local x-axis	4.5 mm	4.5 mm
Rear bushing disp. along local y-axis	0.2 mm	0.3 mm
Rear bushing disp. along local z-axis	15.0 mm	13.1 mm
Ball joint disp. along the fore-aft direction	23.9 mm	31.2 mm
Ball joint disp. along the lateral direction	6.5 mm	9.3 mm
Ball joint reaction in the vertical direction	2.5 kN	3.2 kN

Table 10: Peak-to-peak response: rigid LCA model vs. flexible (1 mass at c.g.) LCA model

DN101 Lower Control Arm
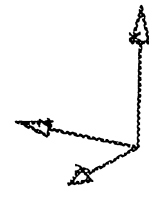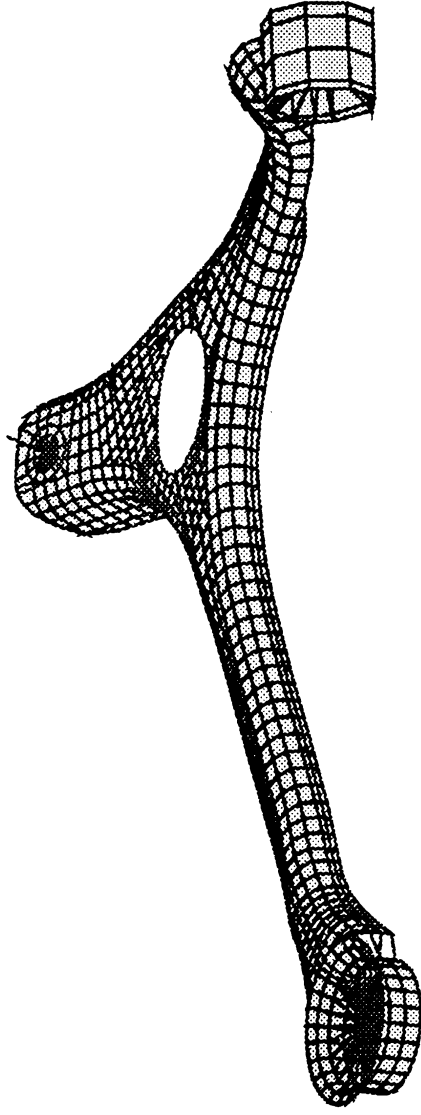
Figure 1

DN101 Front LCA Bushing Quasi-Static Rates

Force (N)

Displacement (mm)

Radial-y

Radial-x

Axial
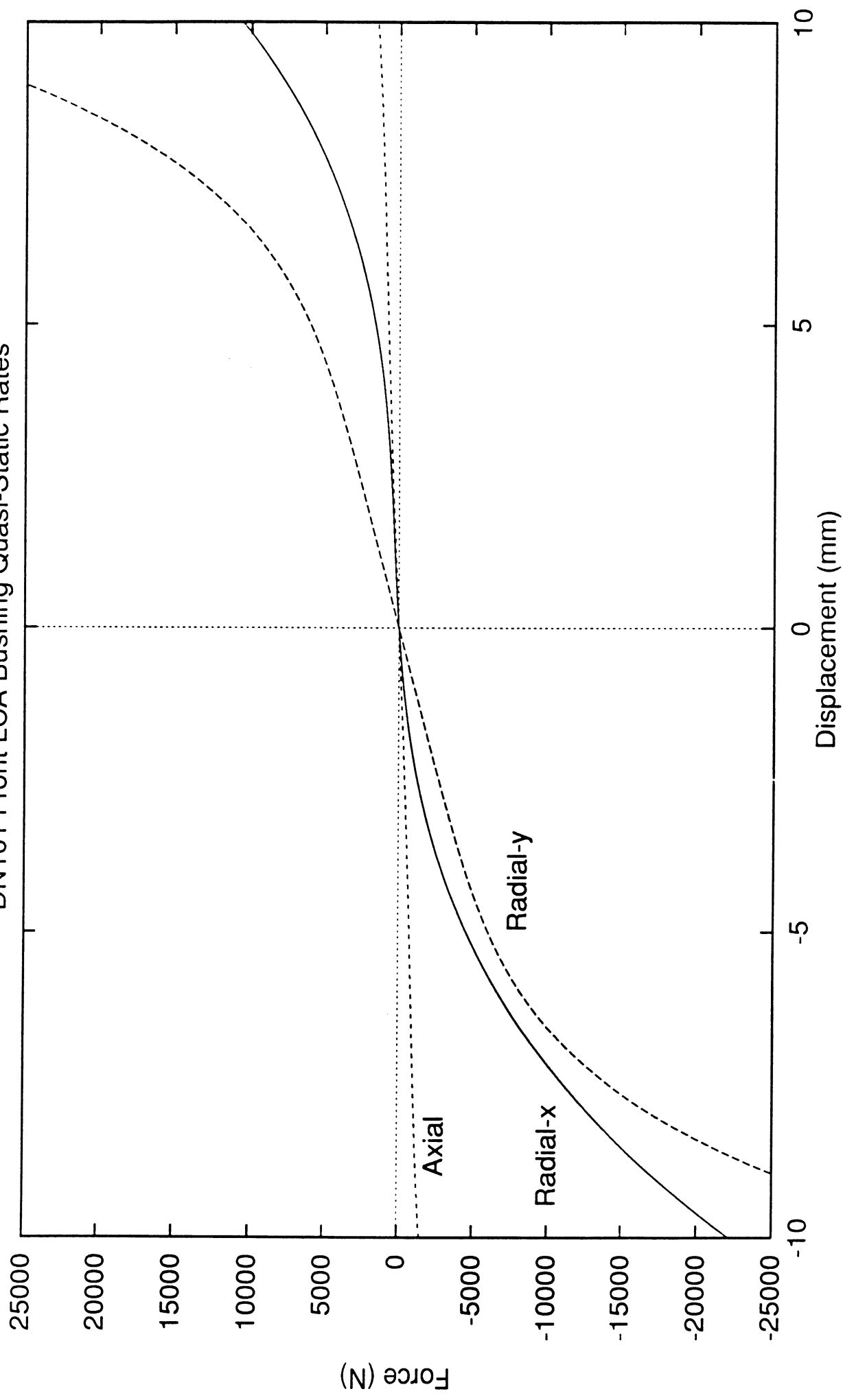
Figure 2

DN101 Rear LCA Bushing Quasi-Static Rates

Radial

Axial

Force (N)

Displacement (mm)
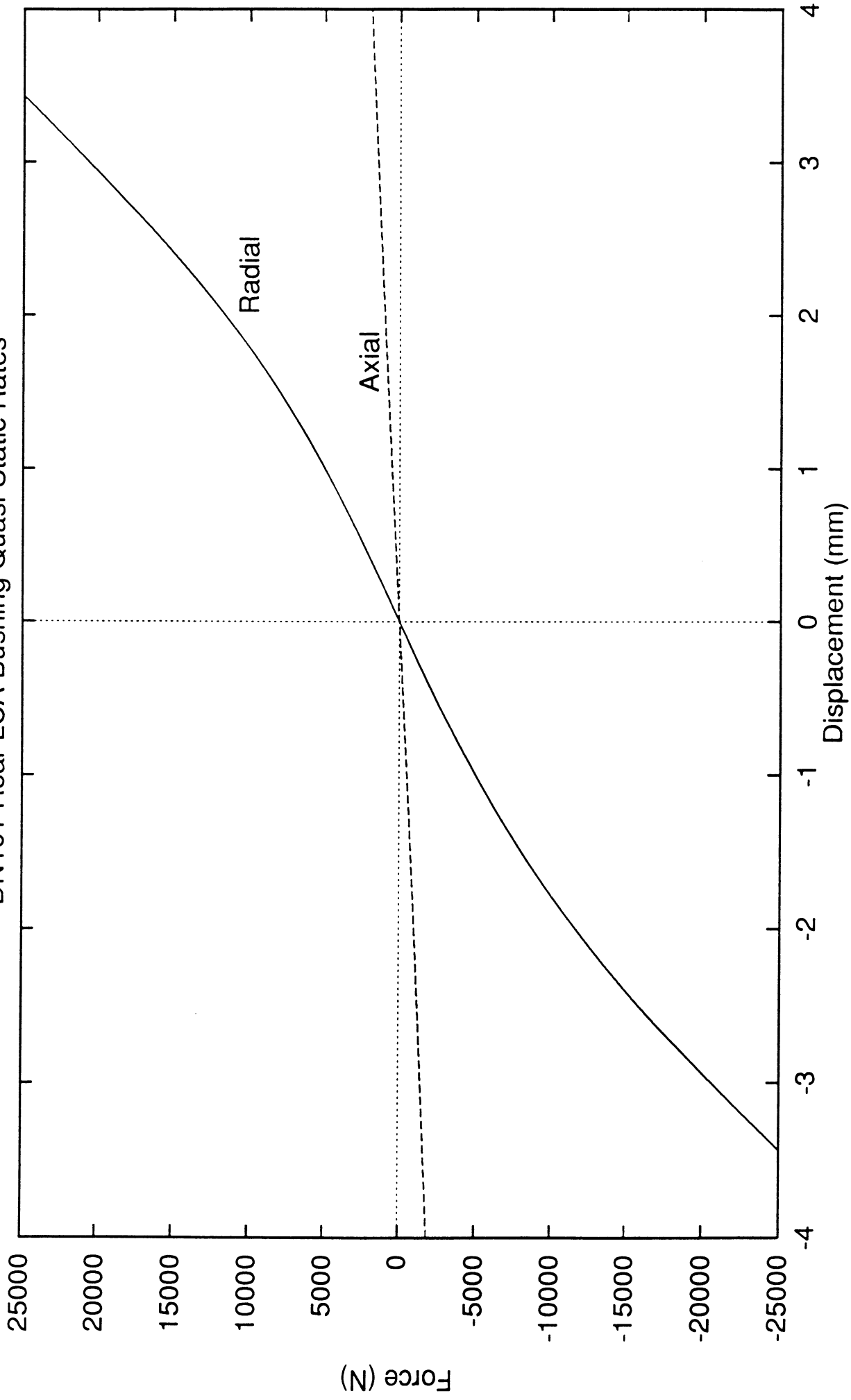
Figure 3

DN101 LCA Chuckhole Road Load Event

ball joint force along the fore-aft direction
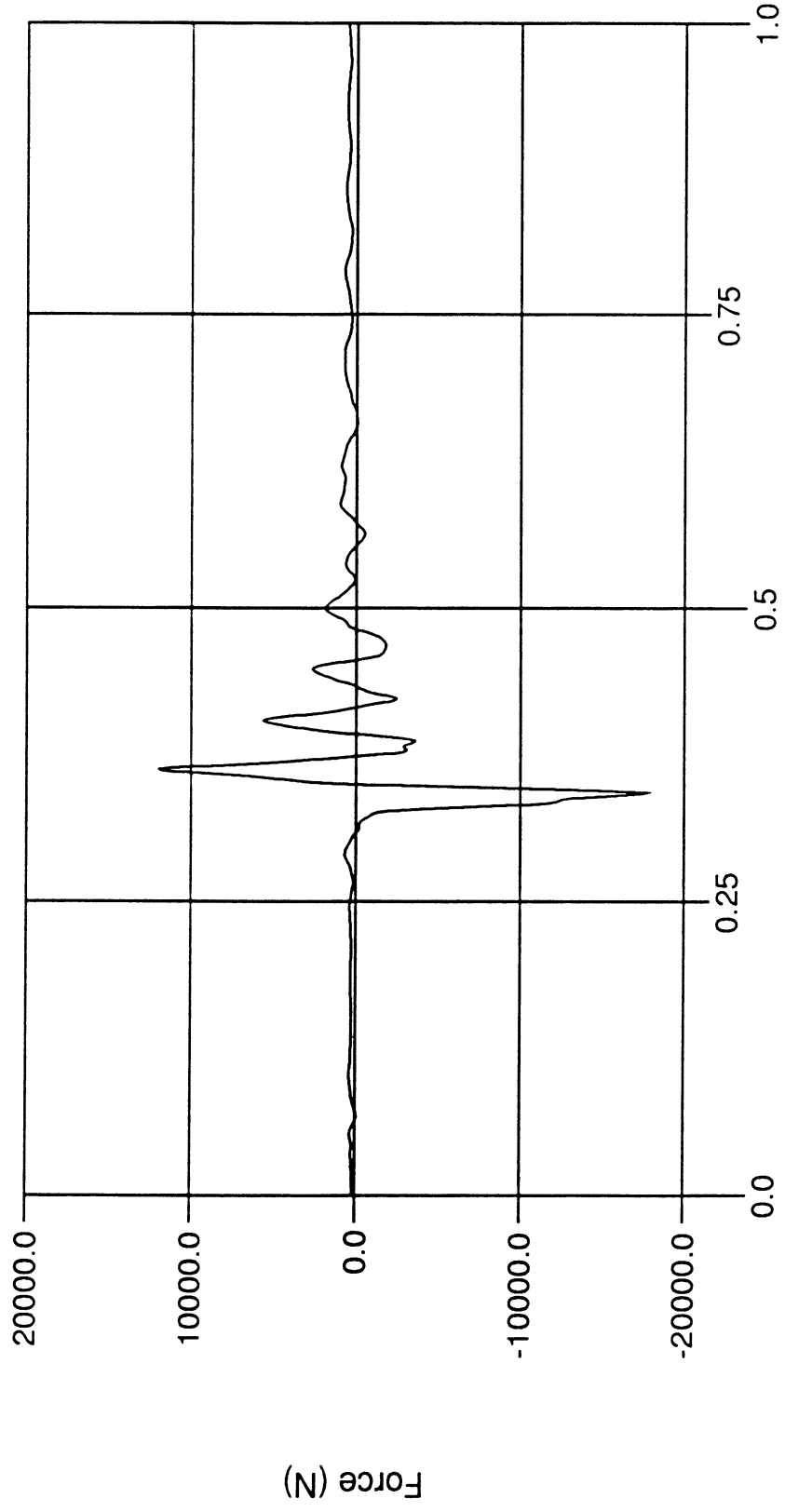
Force (N)

Time (sec.)

Figure 4

DN101 LCA Chuckhole Road Load Event
ball joint force along the lateral direction

Force (N)
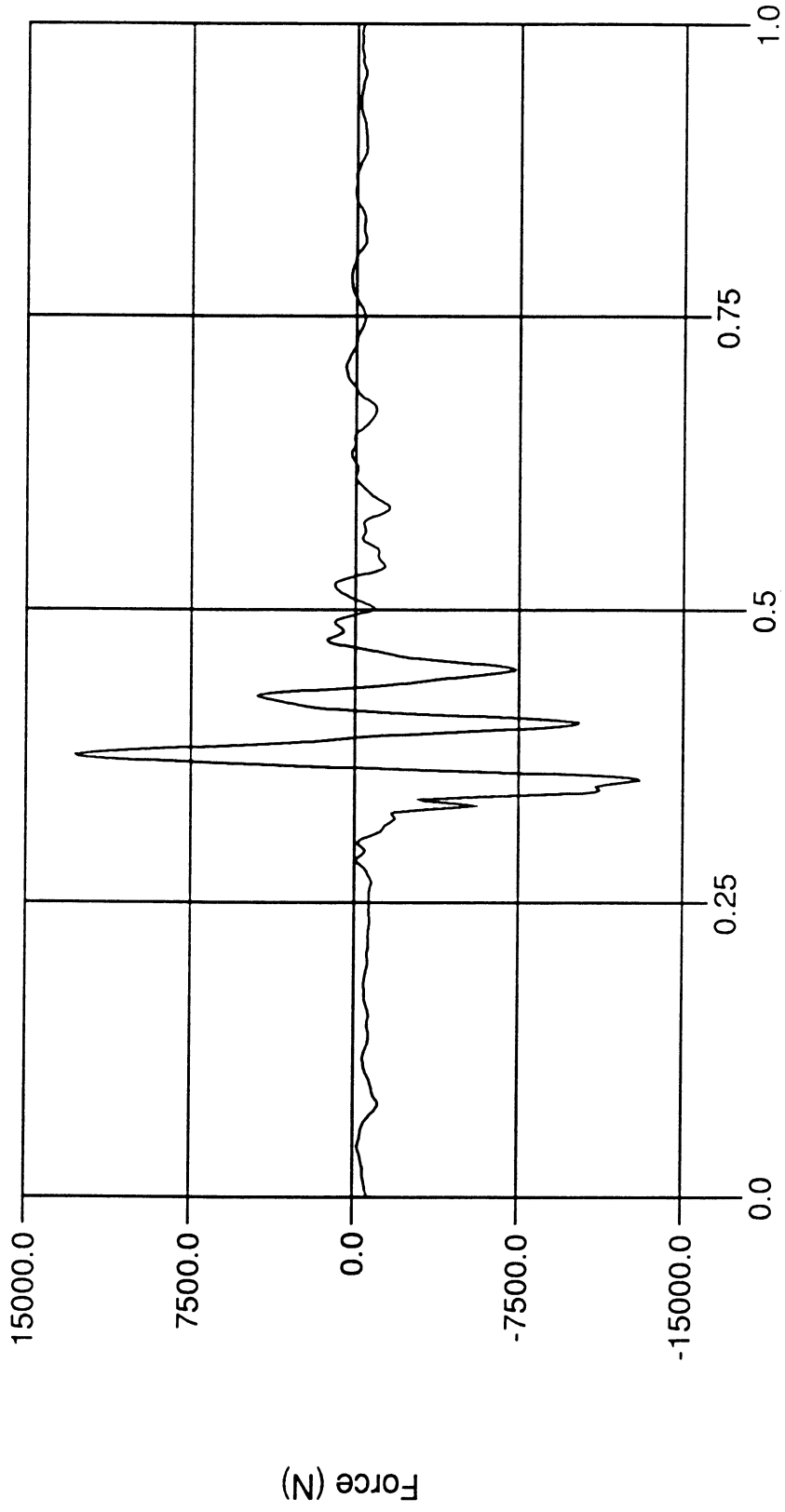
Time (sec.)

Figure 5

DN101 LCA Chuckhole Road Load Event
ball joint displacement along the vertical direction
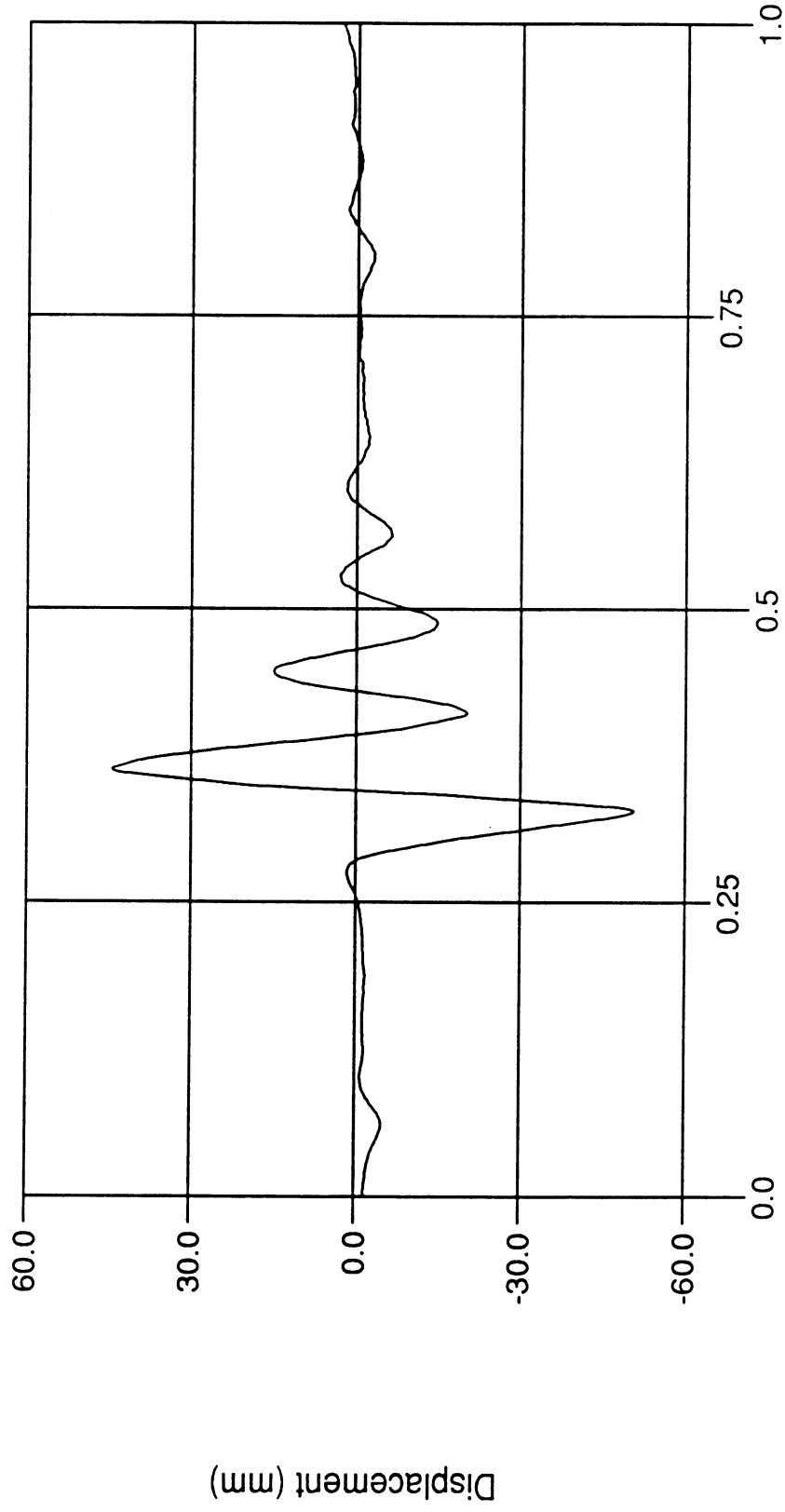
Displacement (mm)

Time (sec.)

Figure 6

DN101 Rigid LCA Mounted on Nonlinear Elastic Bushings

displacement of front bushing along local x-axis

- - - · c = 0.01 * k
—— c = 0.001 * k
—— c = 0.0001 * k
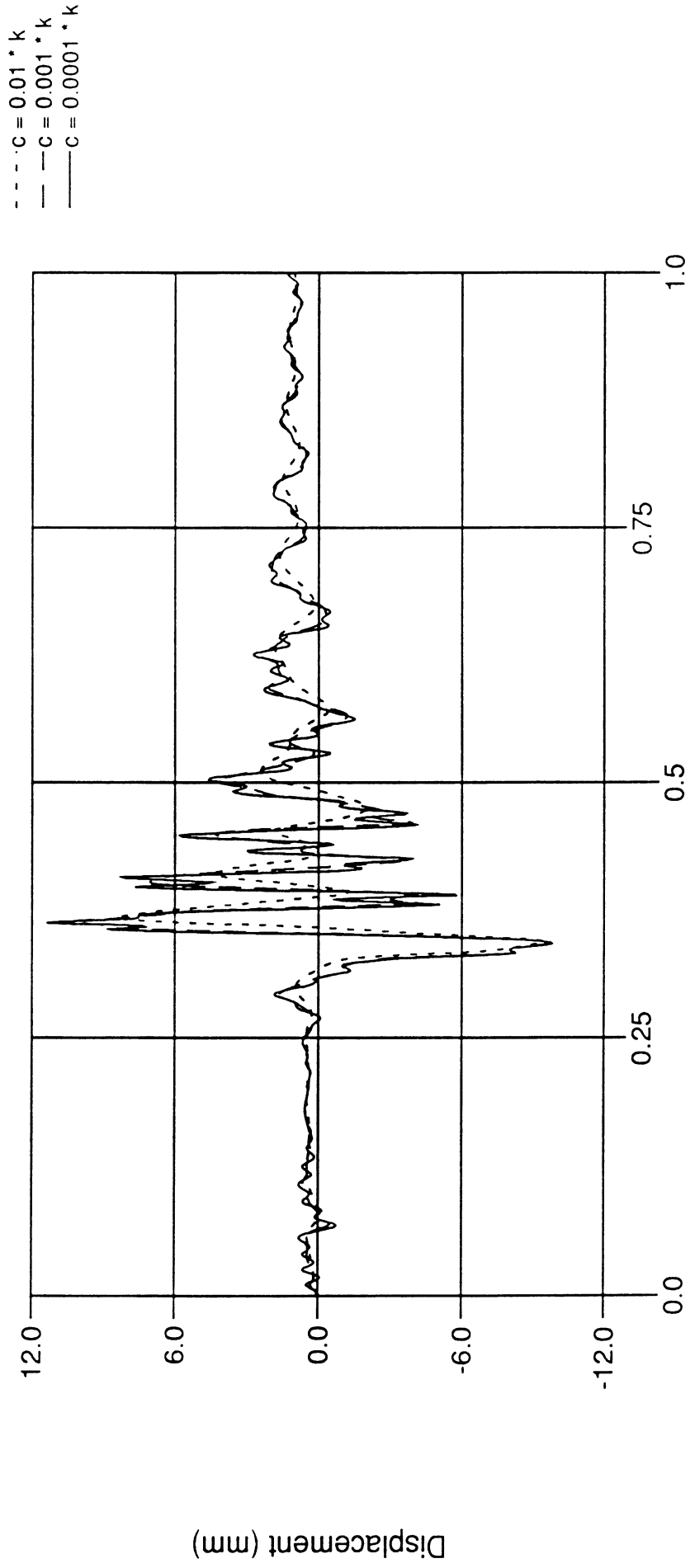
Time (sec.)

Displacement (mm)

Figure 7

DN101 Rigid LCA Mounted on Nonlinear Elastic Bushings
frequency content of displacement of front bushing along local x-axis

Legend:
- - · c = 0.01 * k
— — c = 0.001 * k
——— c = 0.0001 * k

Log Displacement (mm)
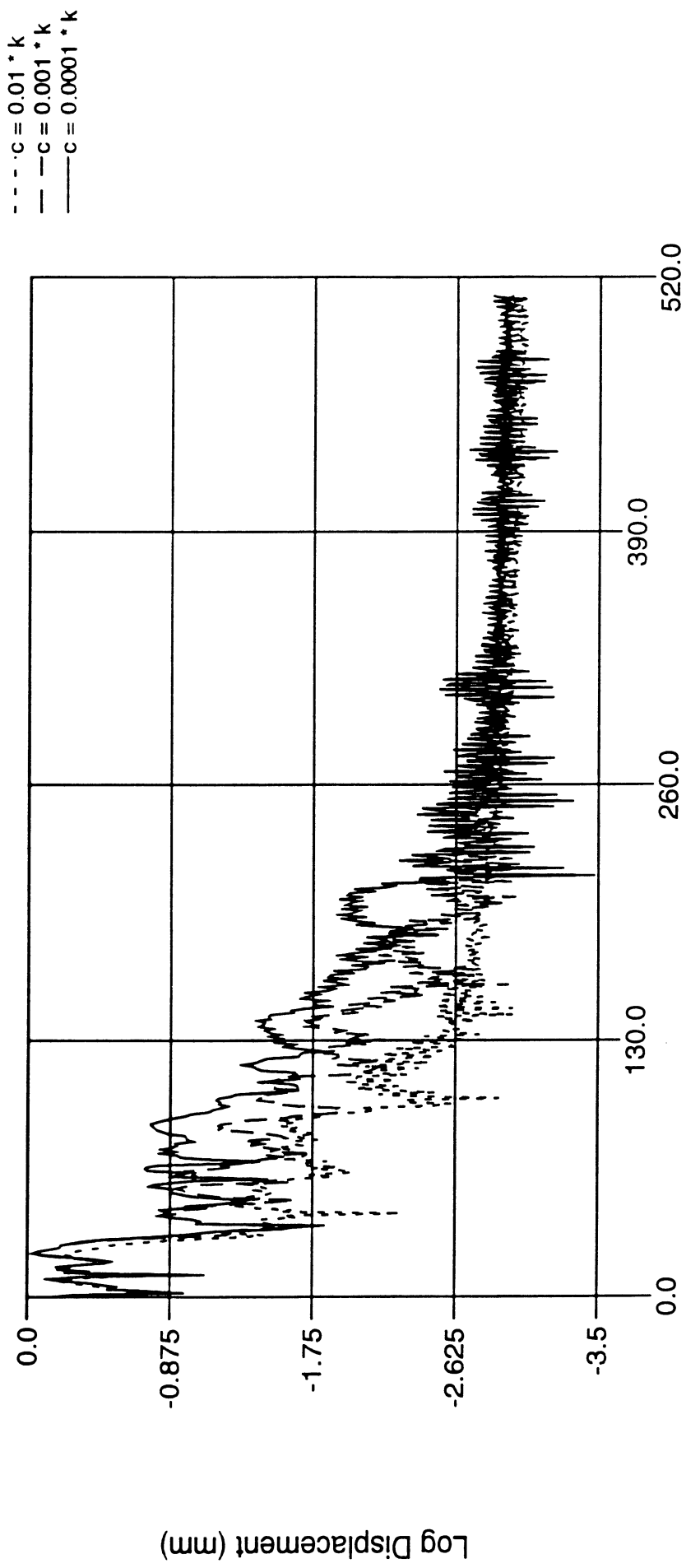
Frequency (Hz)

Figure 8

DN101 Rigid LCA Mounted on Nonlinear Elastic Bushings
front bushing radial force along local x-axis

- - - c = 0.01 * k
— — c = 0.001 * k
——— c = 0.0001 * k
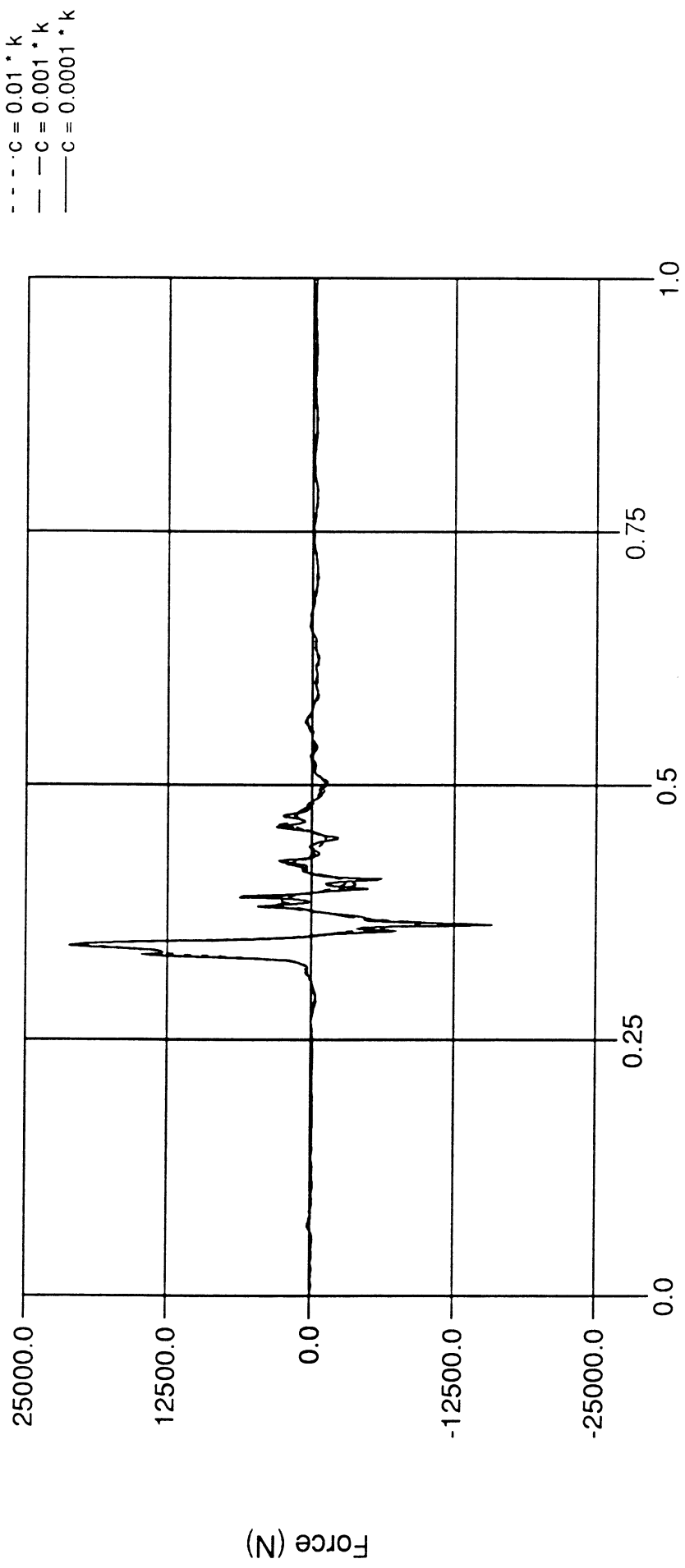
Time (sec.)

Force (N)

Figure 9

DN101 Rigid LCA Mounted on Nonlinear Elastic Bushings

frequency content of front bushing radial force along local x-axis

- - - c = 0.01 * k
— — c = 0.001 * k
—— c = 0.0001 * k

Frequency (Hz)

Log Force (N)
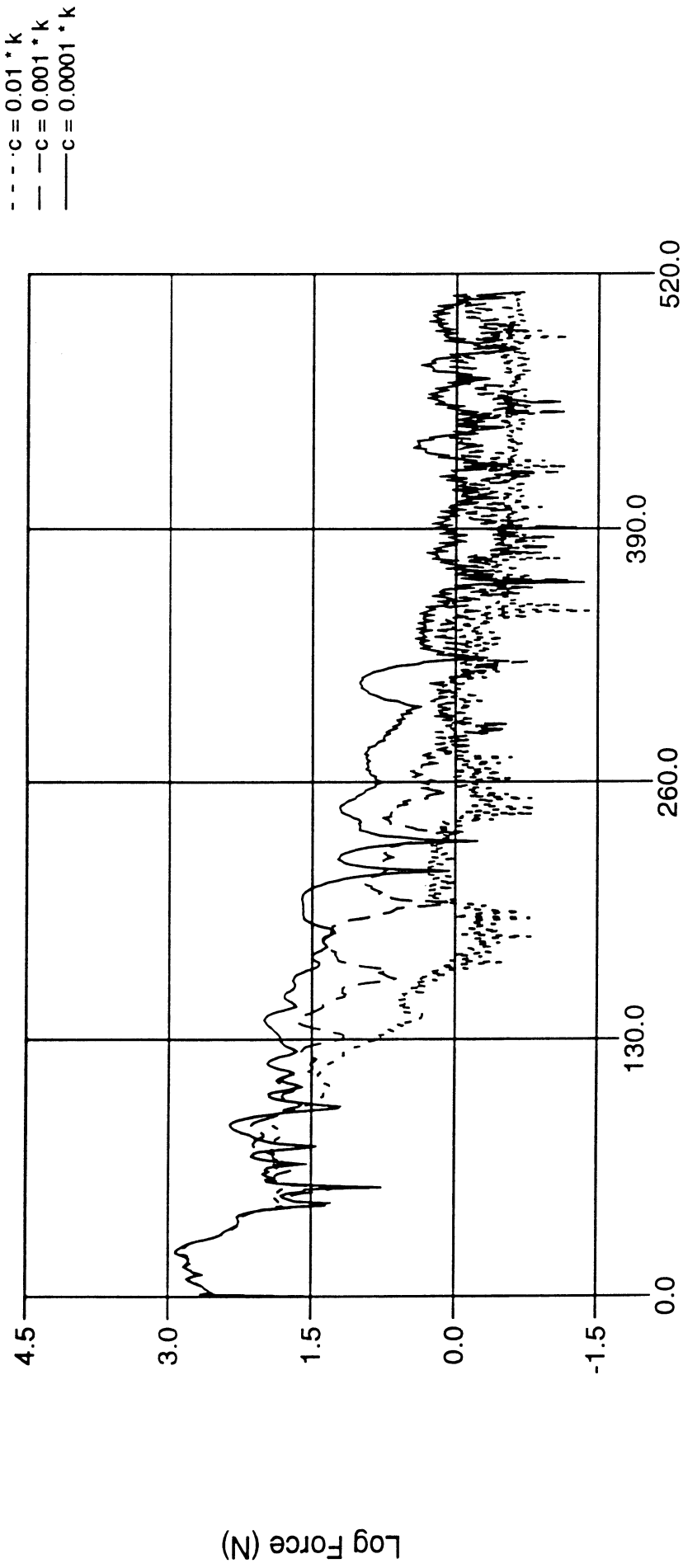
Figure 10

DN101 Rigid LCA Mounted on Nonlinear Elastic Bushings

ball joint displacement along the fore-aft direction

- - - c = 0.01 * k
— — c = 0.001 * k
—— c = 0.0001 * k
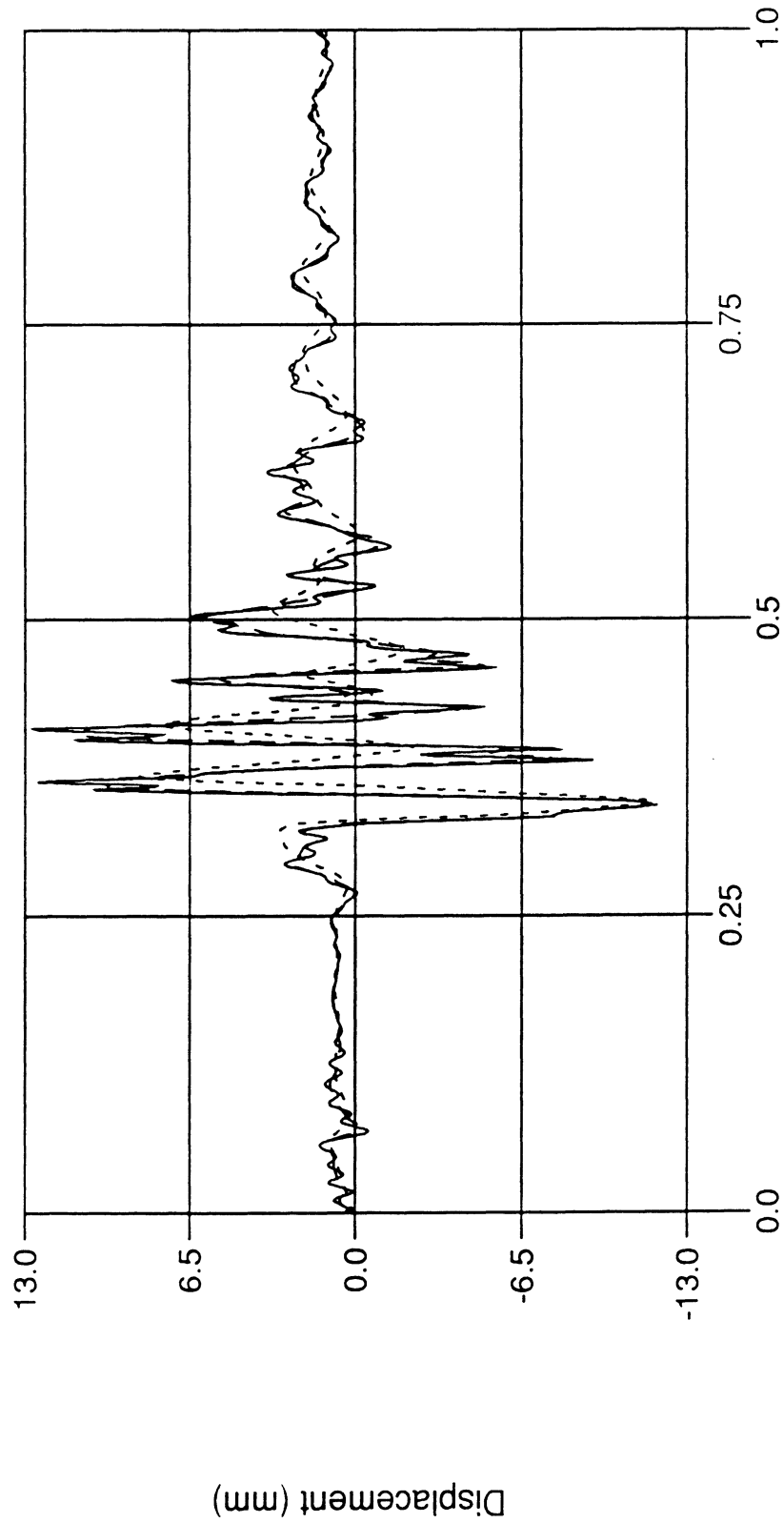
Time (sec.)

Displacement (mm)

Figure 11

DN101 Rigid LCA Mounted on Nonlinear Elastic Bushings

frequency content of ball joint displacements along the fore-aft direction

- - - · c = 0.01 * k
— — c = 0.001 * k
——— c = 0.0001 * k

Frequency (Hz)
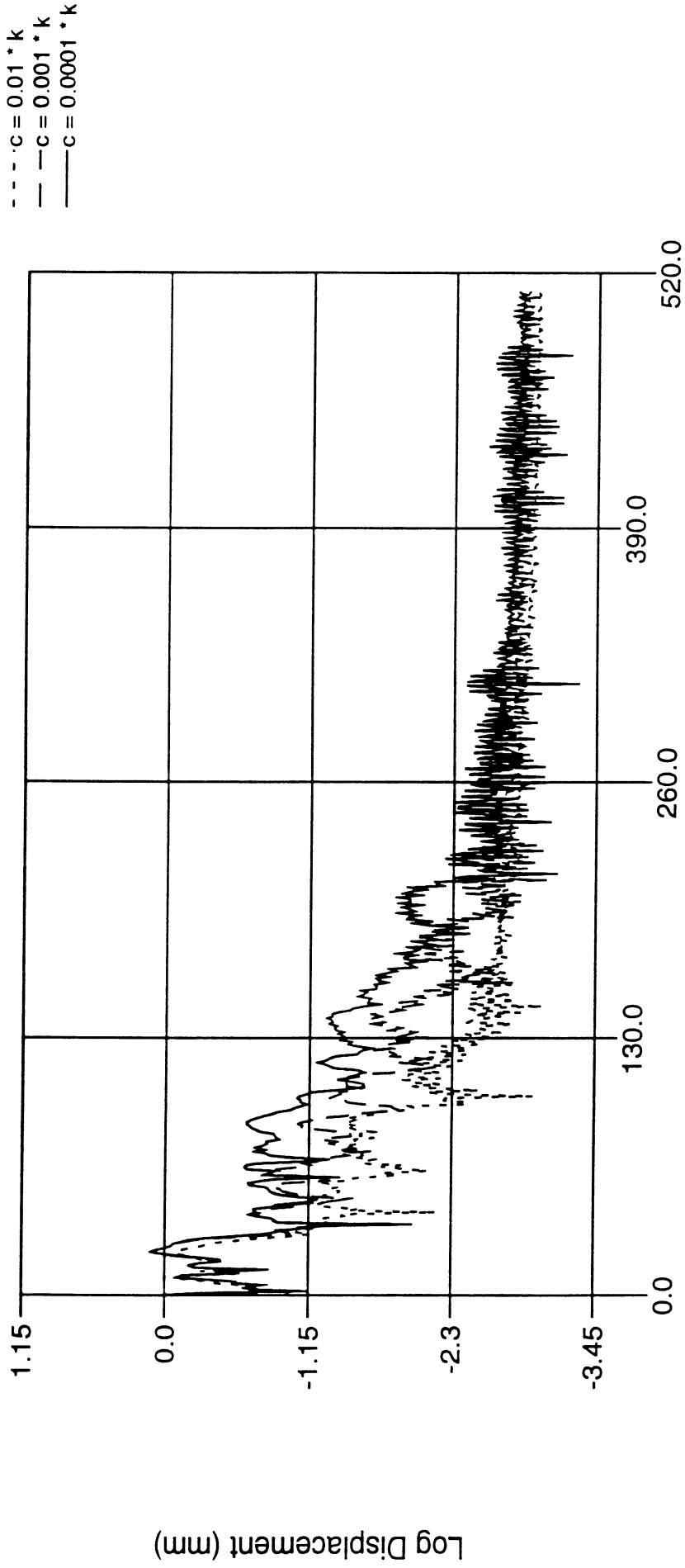
Log Displacement (mm)

Figure 12

DN101 Flexible LCA, Default Mass Lumping

ball joint displacement along the fore-aft direction

KRF at node 356
KRF at node 121

Displacement (mm)
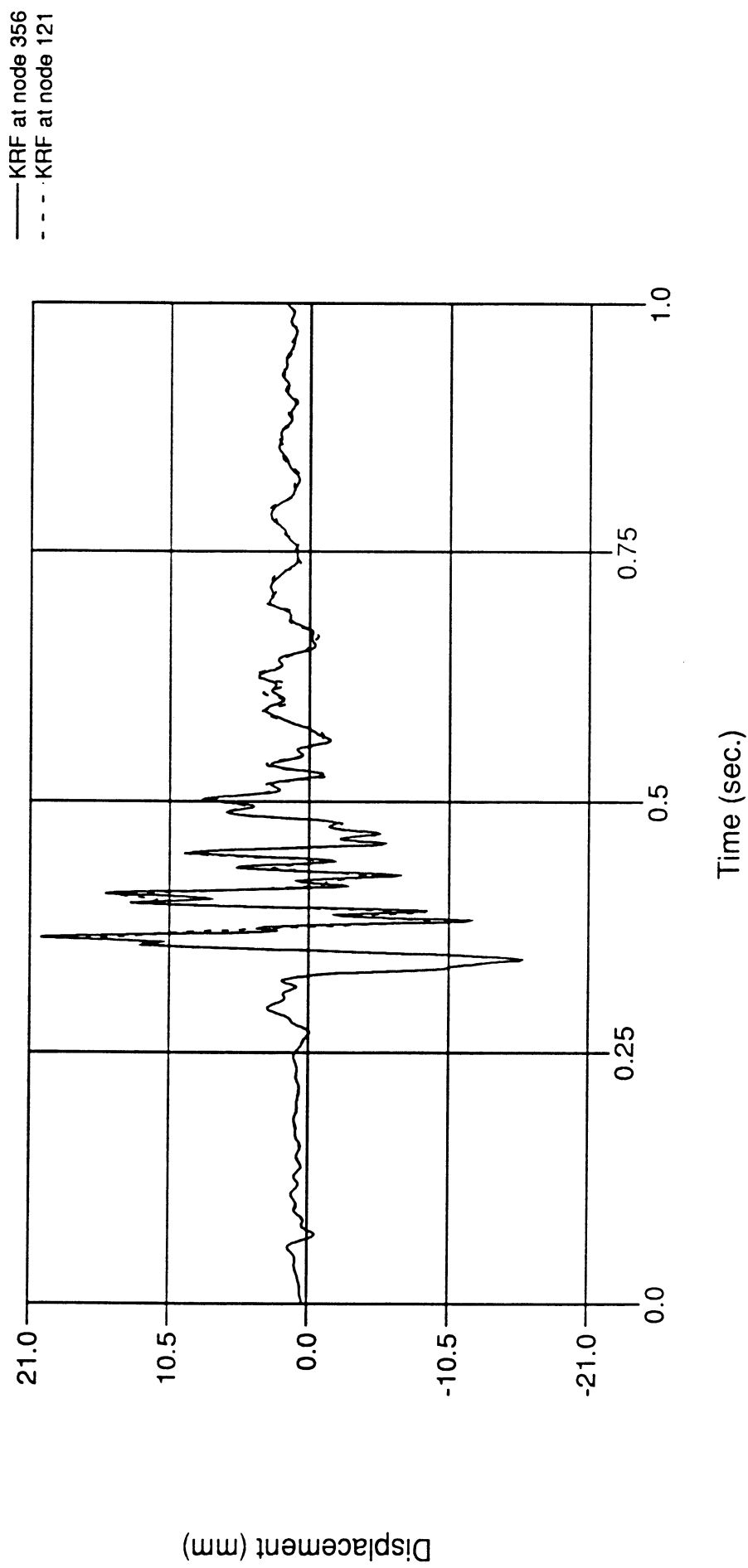
Time (sec.)

Figure 13

DN101 Flexible LCA, Default Mass Lumping
ball joint displacement along the lateral direction

KRF at node 356
KRF at node 121
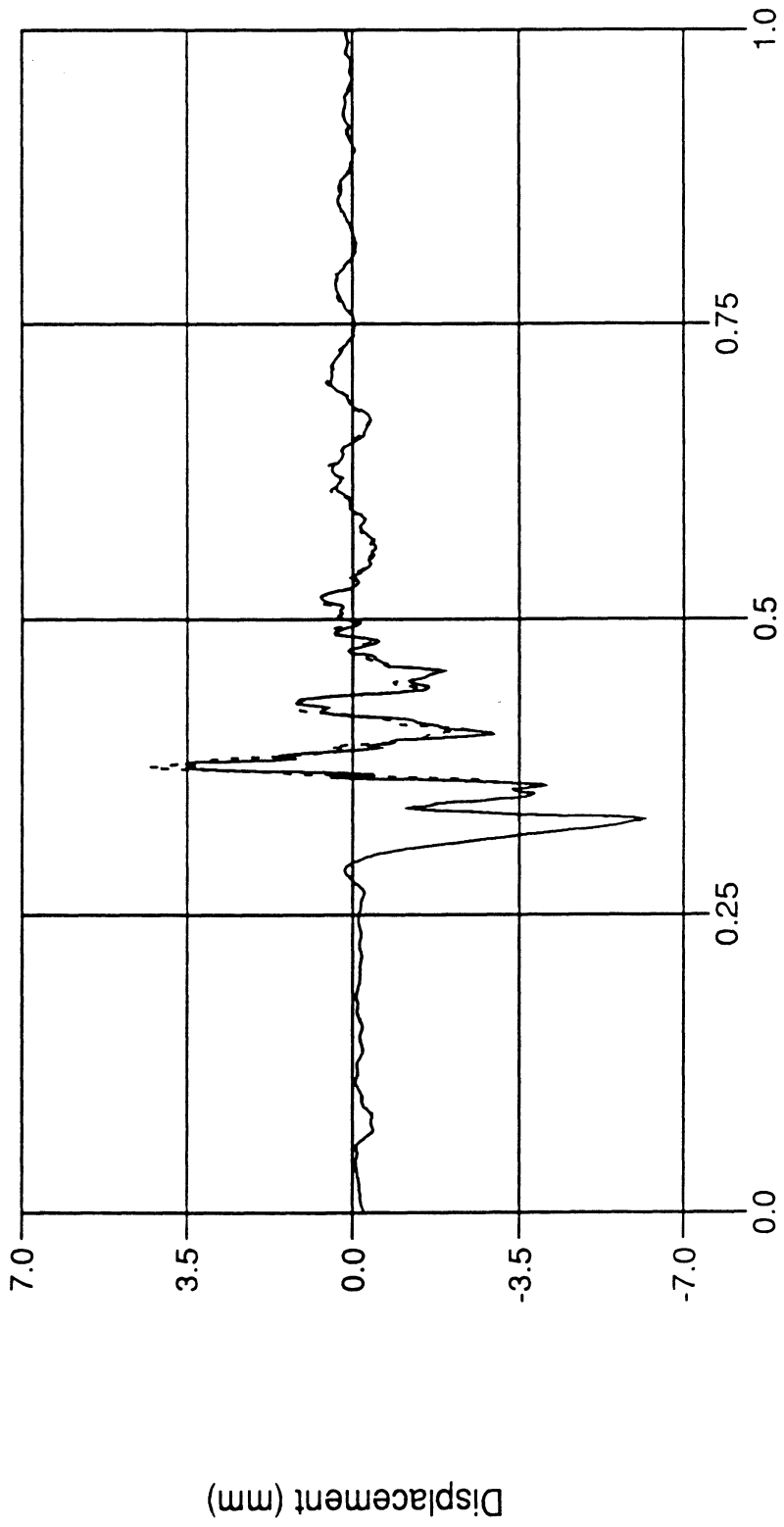
Displacement (mm)

Time (sec.)

Figure 14

DN101 Flexible LCA, Default Mass Lumping
ball joint reaction along the vertical direction

KRF at node 356
KRF at node 121

Reaction Force (N)
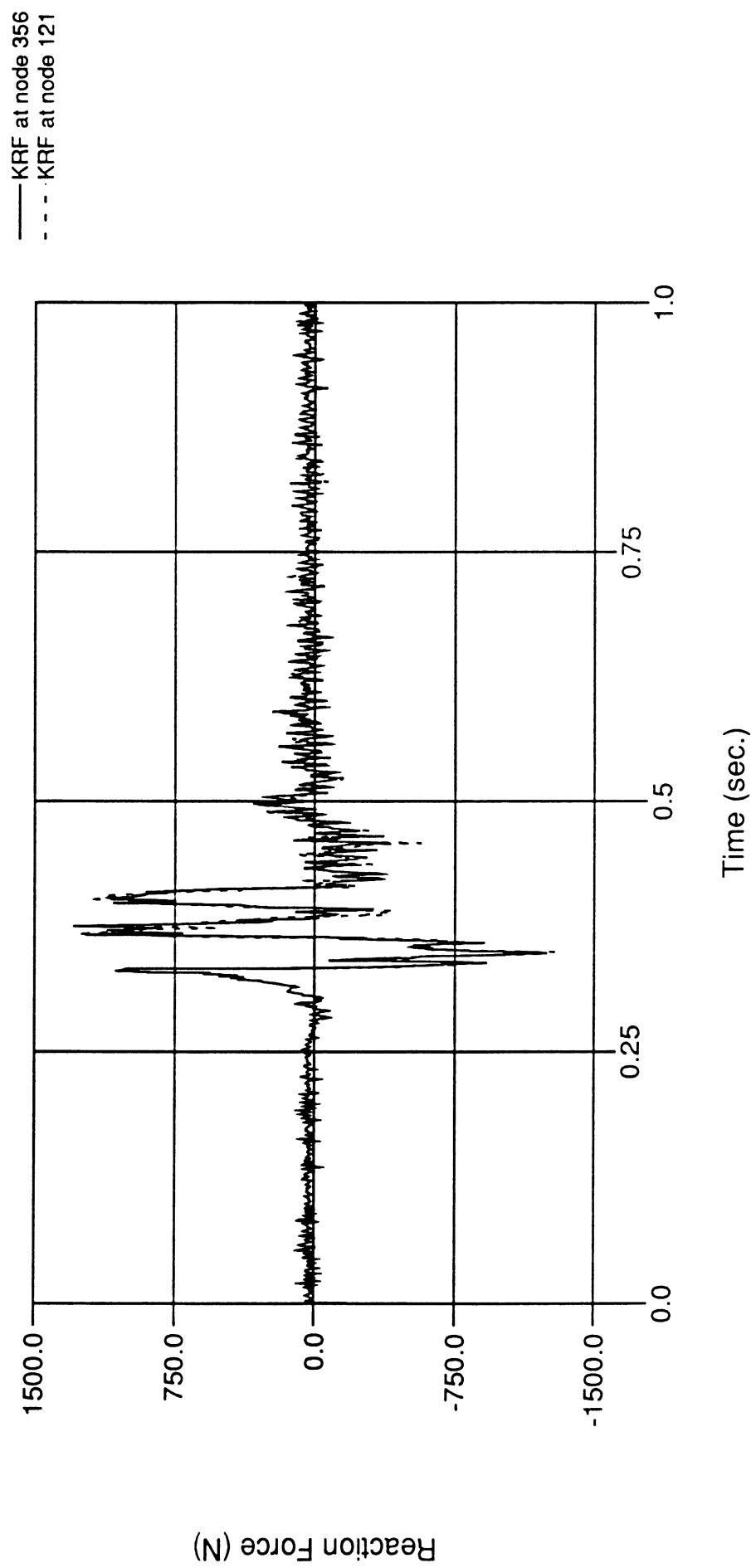
Time (sec.)

Figure 15

DN101 Flexible LCA, Default Mass Lumping
displacement of front bushing along local x-axis

Legend:
—— KRF at node 356
- - - KRF at node 121

Displacement (mm): 12.0, 6.0, 0.0, -6.0, -12.0

Time (sec.): 0.0, 0.25, 0.5, 0.75, 1.0
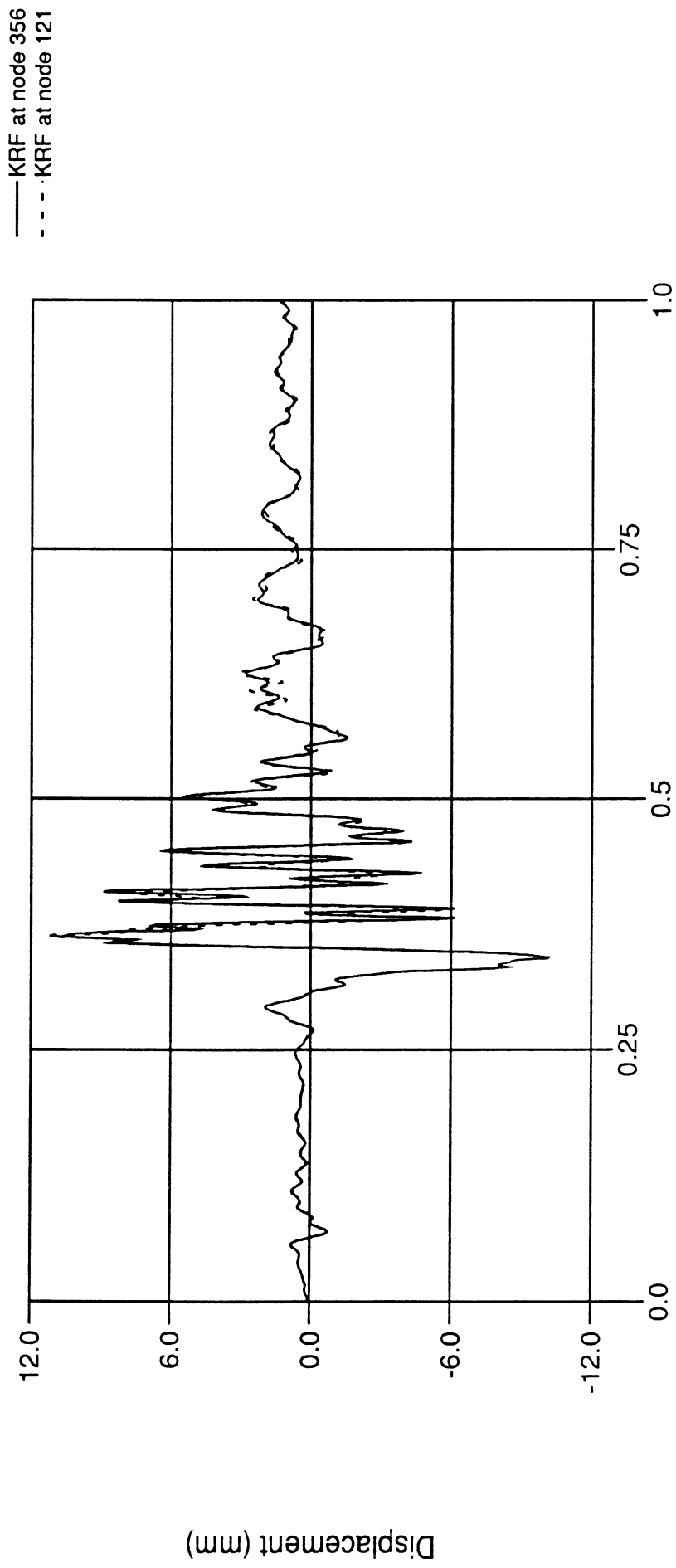
Figure 16

DN101 Flexible LCA, Default Mass Lumping
displacement of front bushing along local y-axis
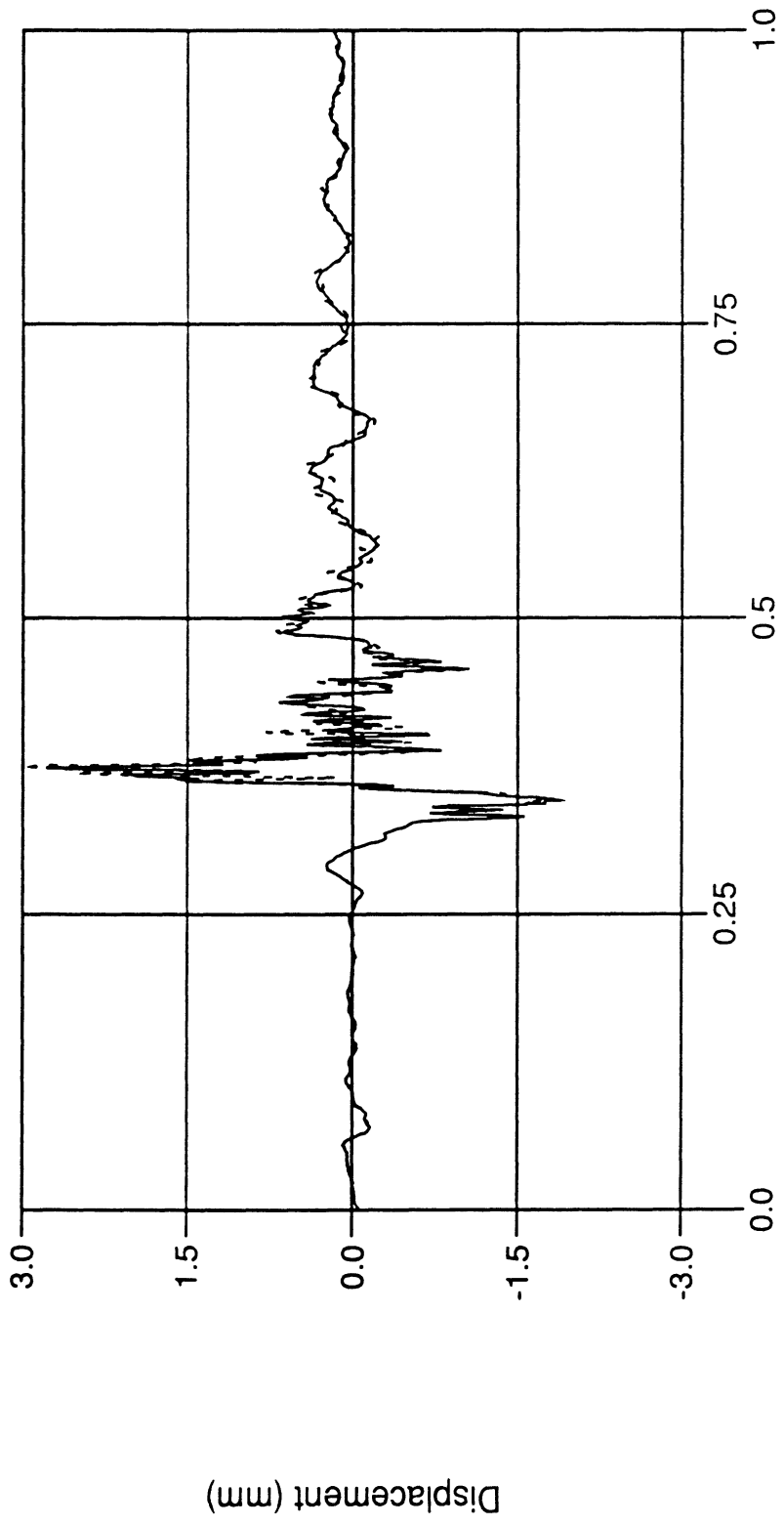
Figure 17

DN101 Flexible LCA, Default Mass Lumping
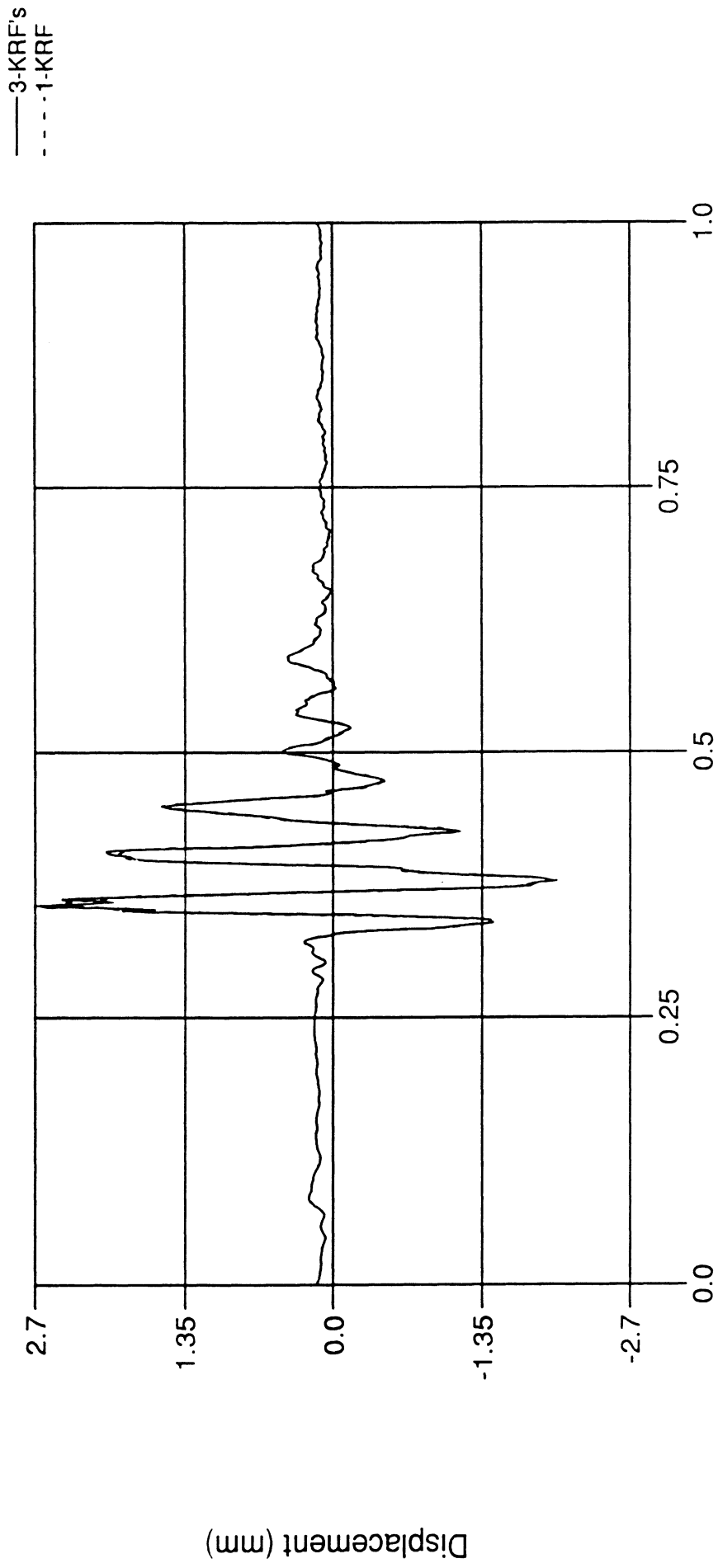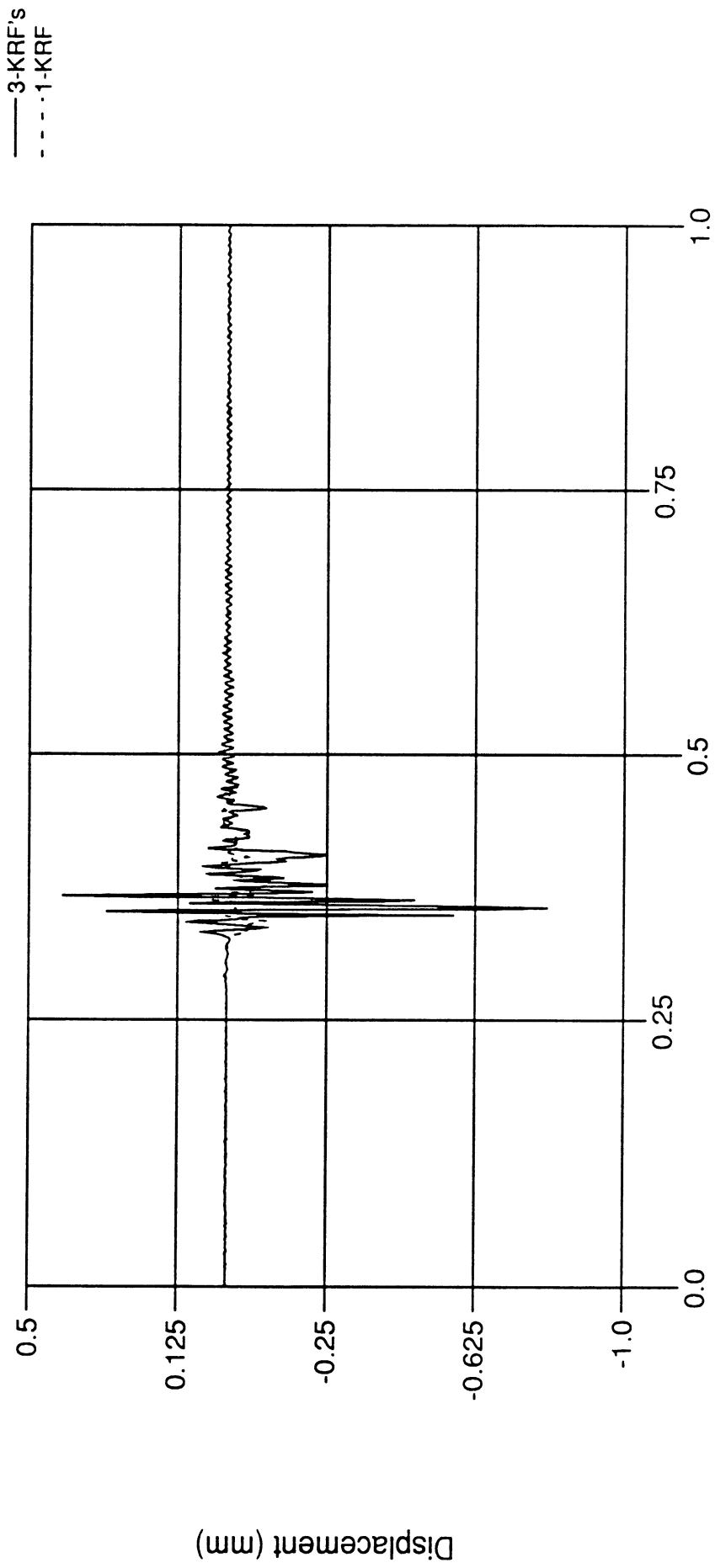displacement of front bushing along local z-axis

KRF at node 356
KRF at node 121

Displacement (mm)
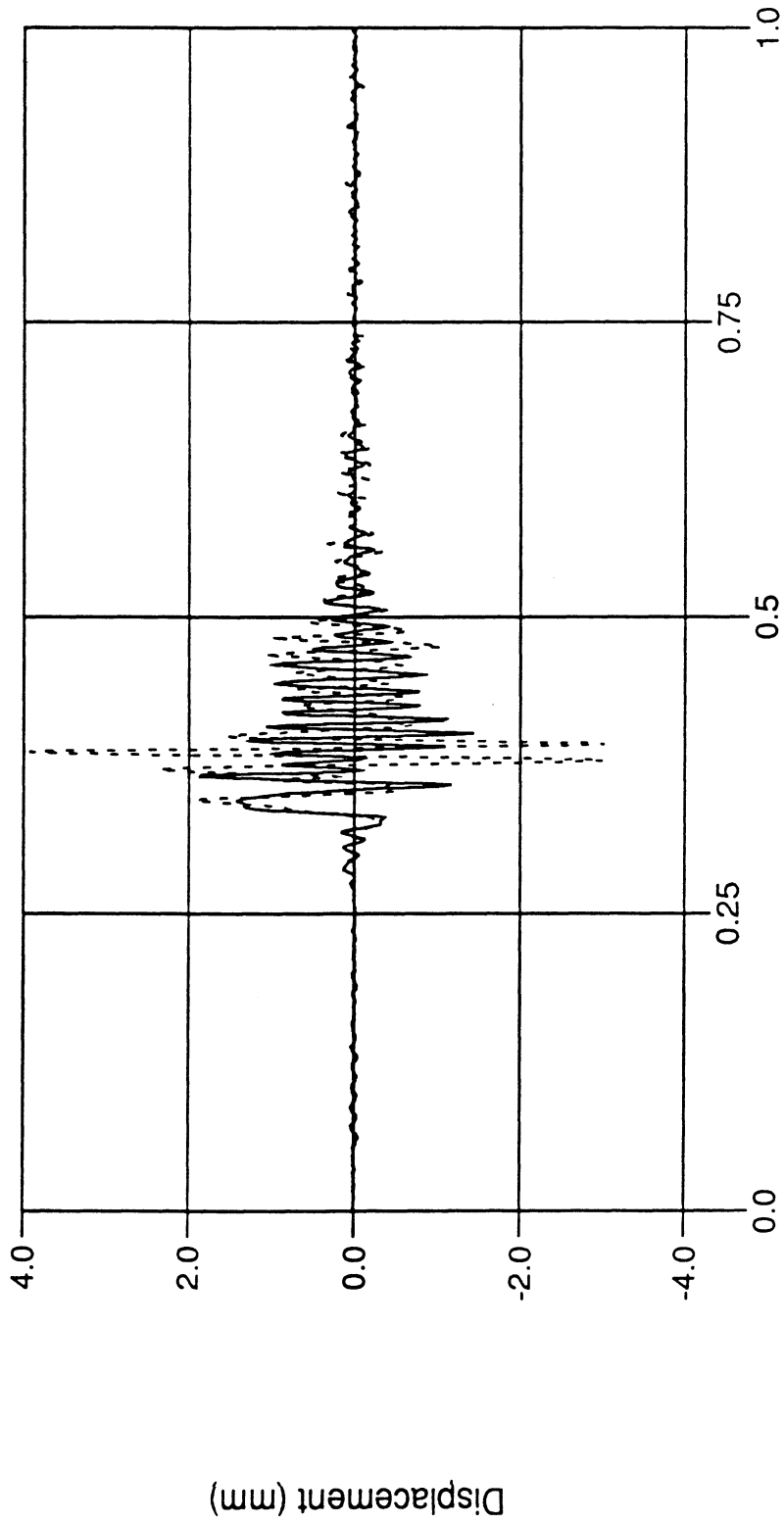
Time (sec.)

Figure 18

DN101 Flexible LCA, Default Mass Lumping
front bushing radial force along local x-axis

KRF at node 356
KRF at node 121
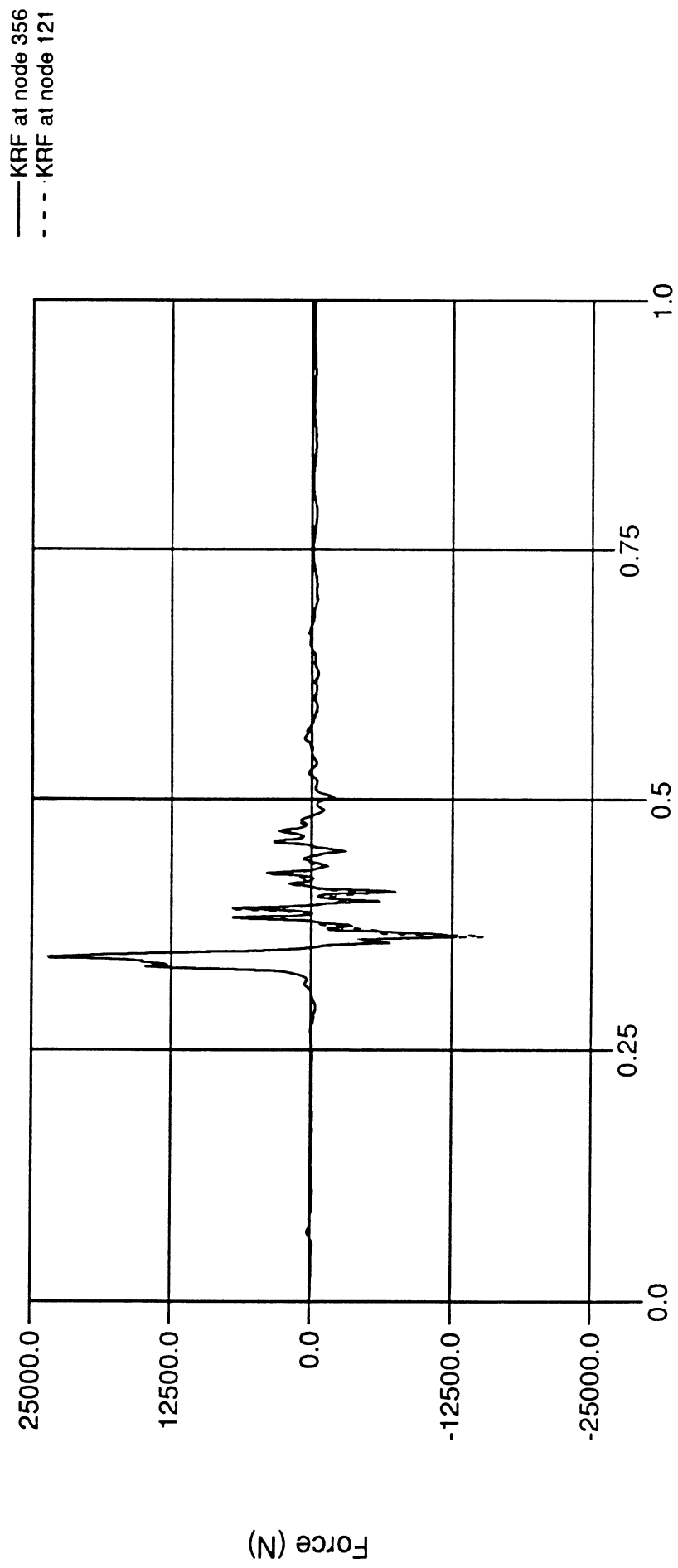
Force (N)

Time (sec.)

Figure 19

DN101 Flexible LCA, Default Mass Lumping
front bushing radial force along local y-axis

KRF at node 356
KRF at node 121

Force (N)

2500.0
625.0
-1250.0
-3125.0
-5000.0

0.0   0.25   0.5   0.75   1.0
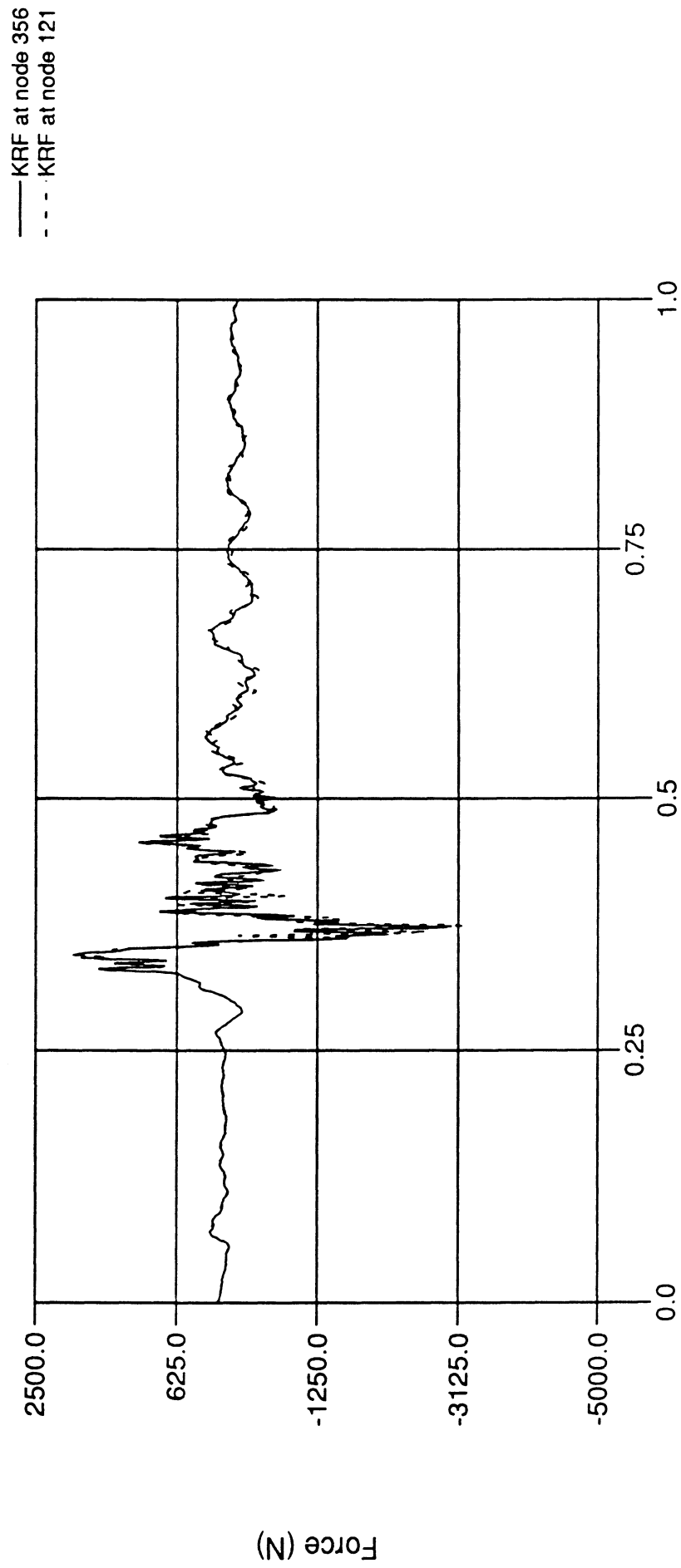
Time (sec.)

Figure 20

DN101 Flexible LCA, Default Mass Lumping
front bushing axial force along local z-axis

KRF at node 356
KRF at node 121

Time (sec.)

Force (N)
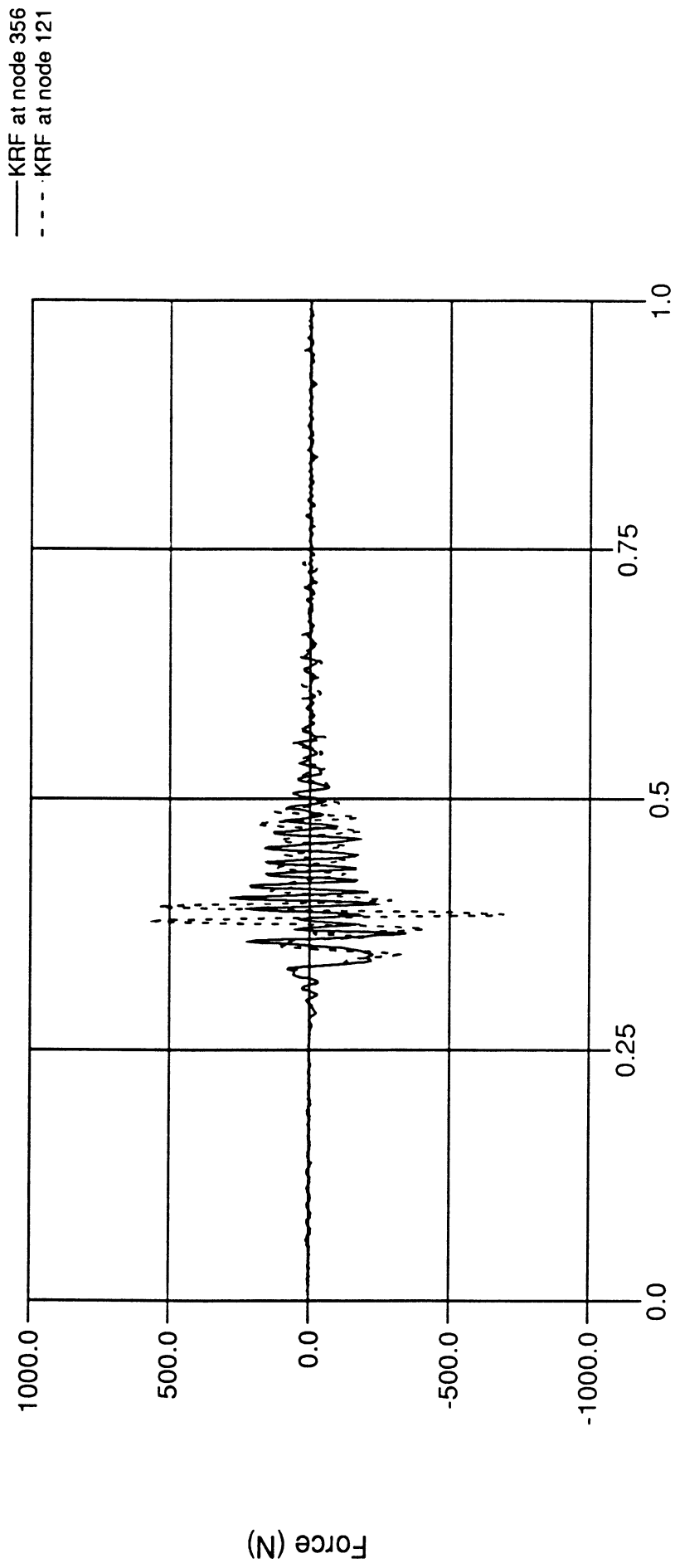
Figure 21

DN101 Flexible LCA, Default Mass Lumping
displacement of rear bushing along local x-axis

KRF at node 356
KRF at node 121
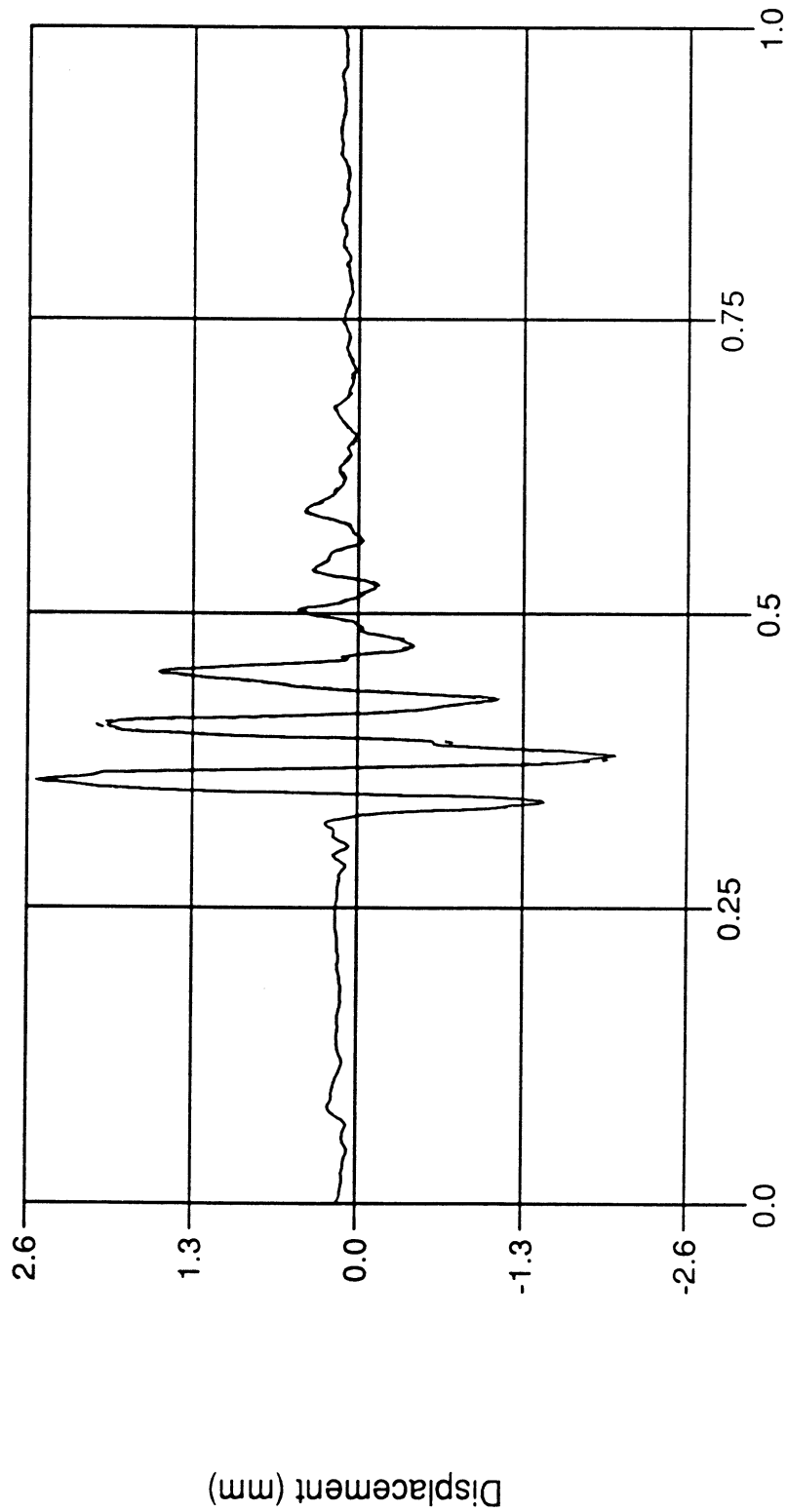
Displacement (mm)

Time (sec.)

Figure 22

DN101 Flexible LCA, Default Mass Lumping
displacement of rear bushing along local y-axis

KRF at node 356
KRF at node 121
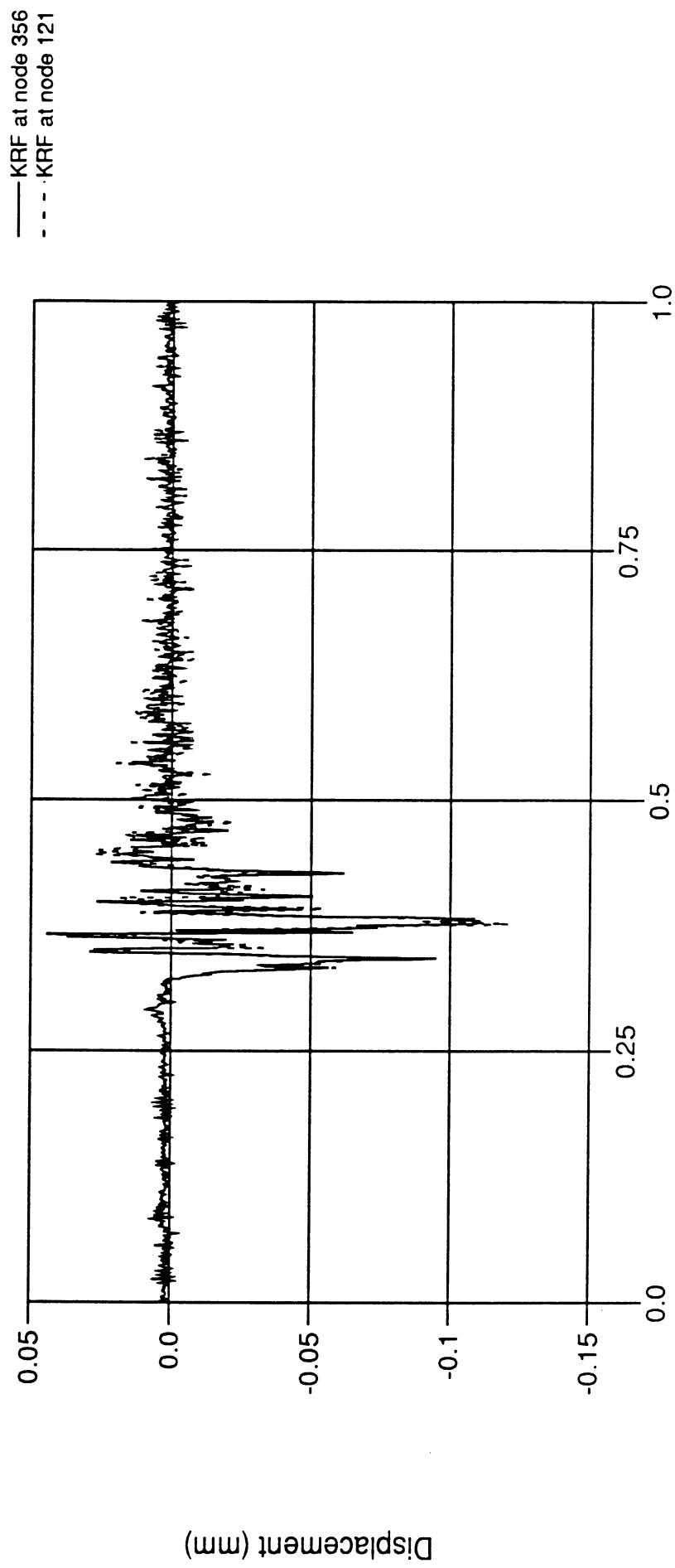
Time (sec.)

Displacement (mm)

Figure 23

DN101 Flexible LCA, Default Mass Lumping
displacement of rear bushing along local z-axis

KRF at node 356
KRF at node 121

Displacement (mm)
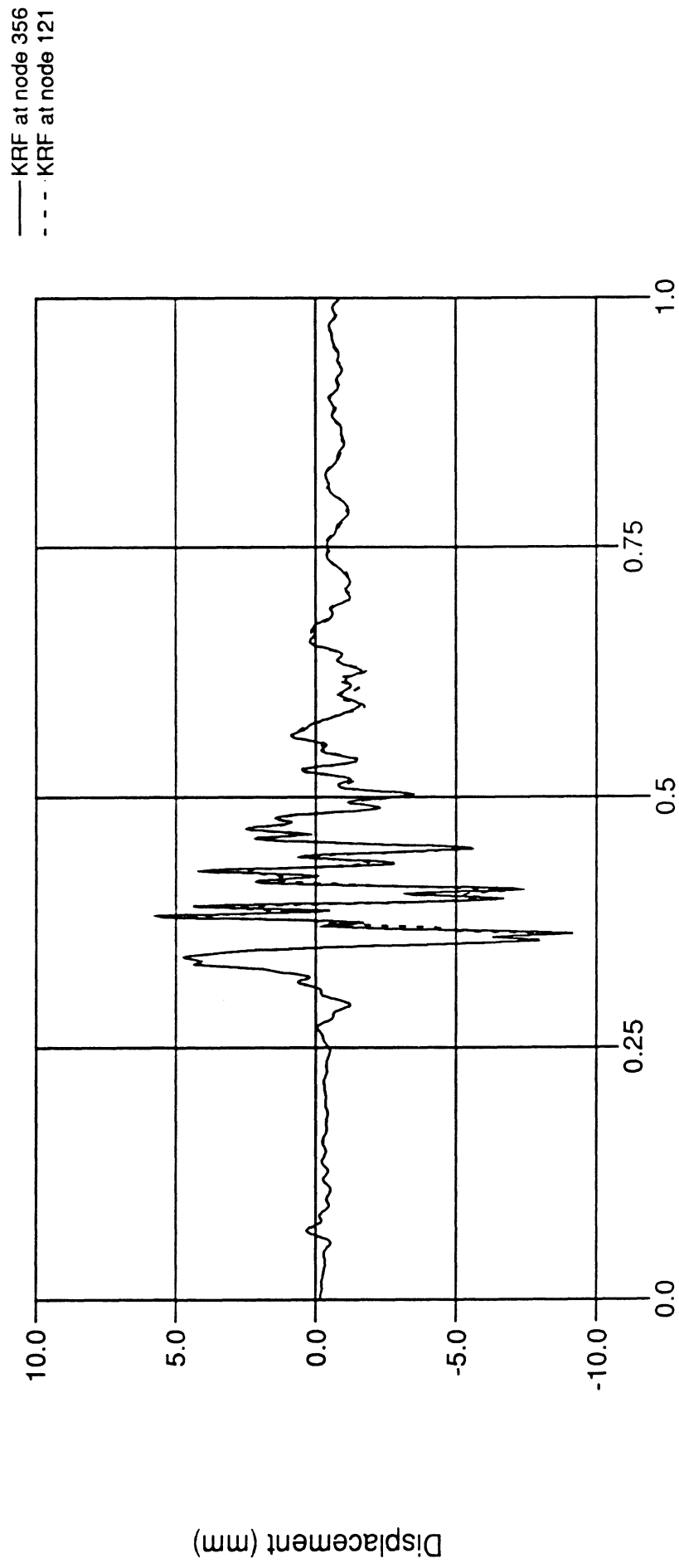
Time (sec.)

Figure 24

DN101 Flexible LCA, Default Mass Lumping

rear bushing radial force along local x-axis

Legend:
— KRF at node 356
– – – KRF at node 121

Force (N) vs Time (sec.)
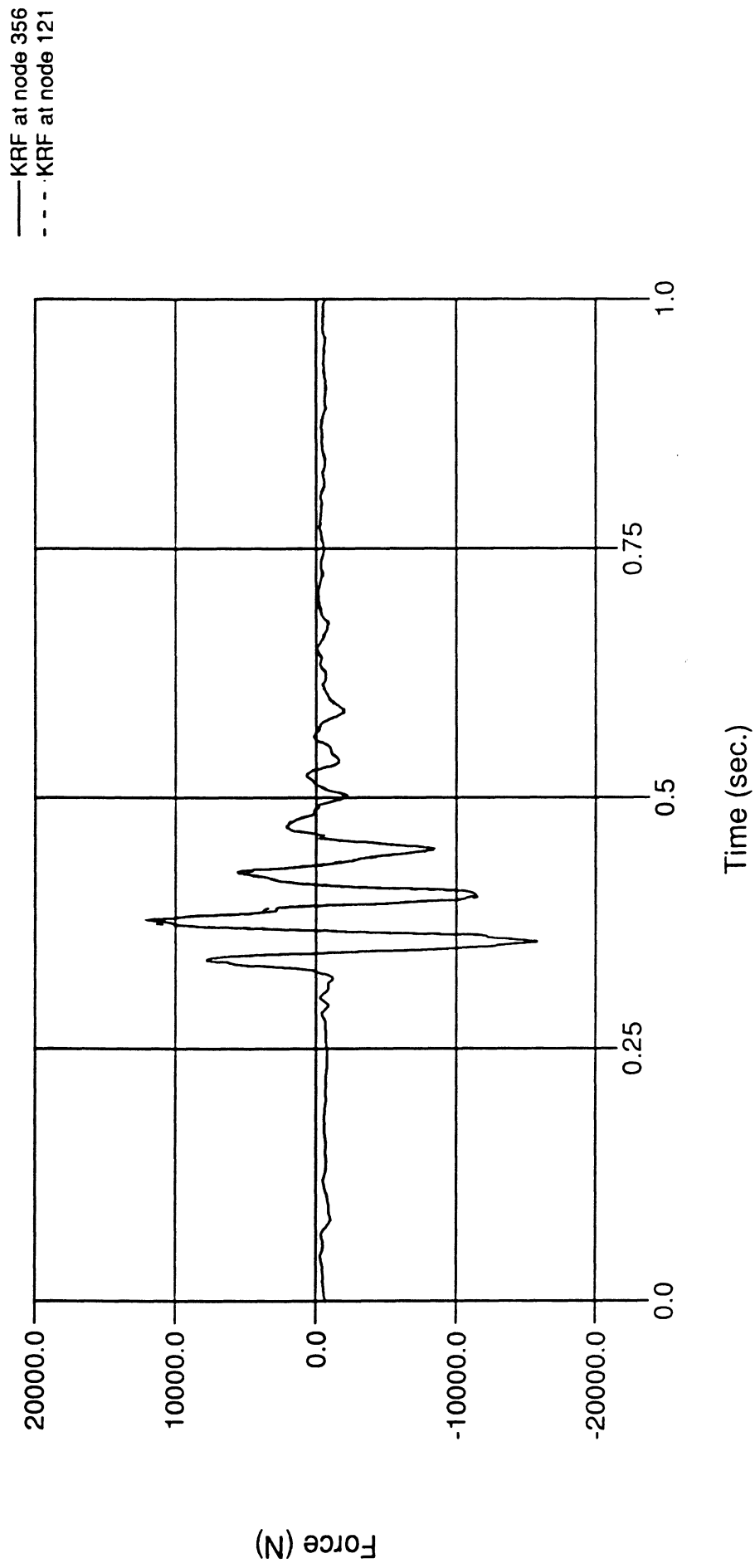
Figure 25

DN101 Flexible LCA, Default Mass Lumping
rear bushing radial force along local y-axis

KRF at node 356
KRF at node 121
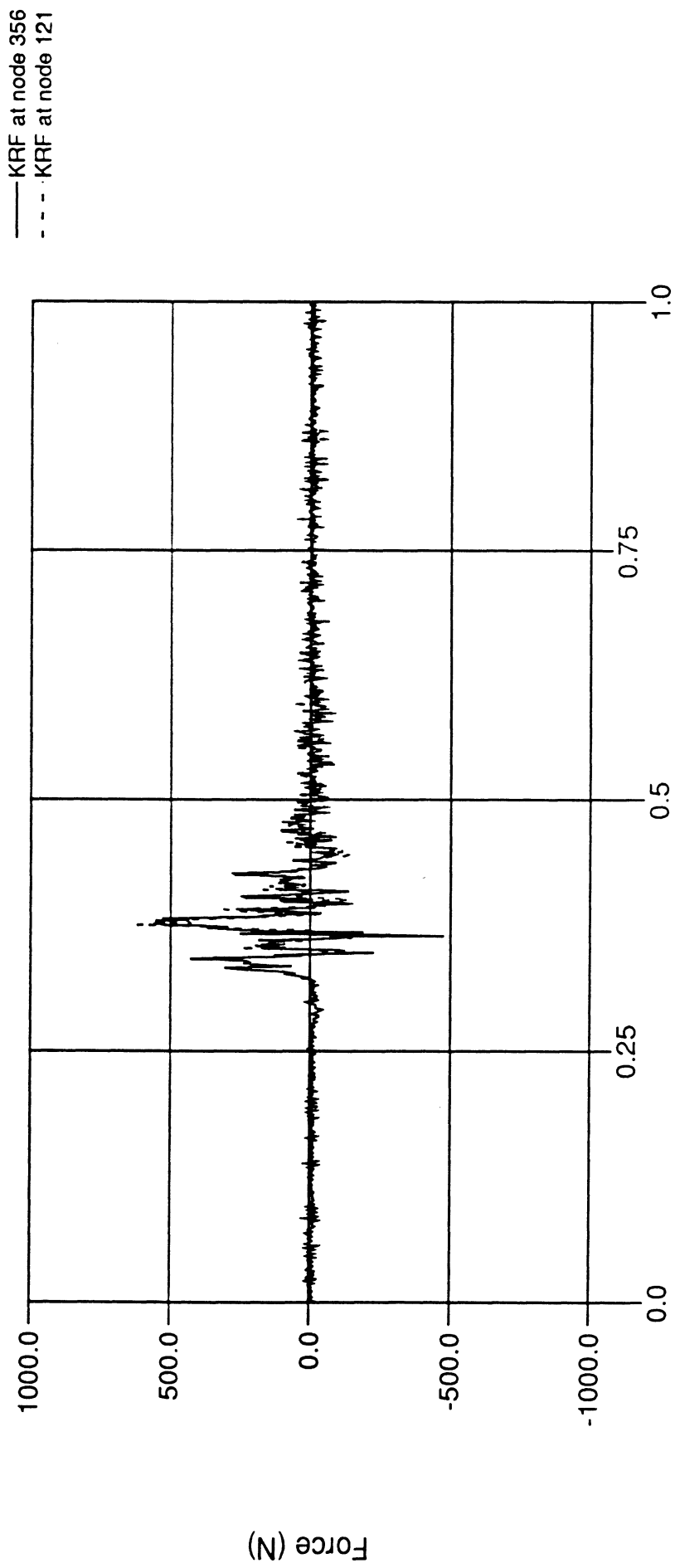
Force (N)

Time (sec.)

Figure 26

DN101 Flexible LCA, Default Mass Lumping
rear bushing axial force along local z-axis

KRF at node 356
KRF at node 121

Force (N)
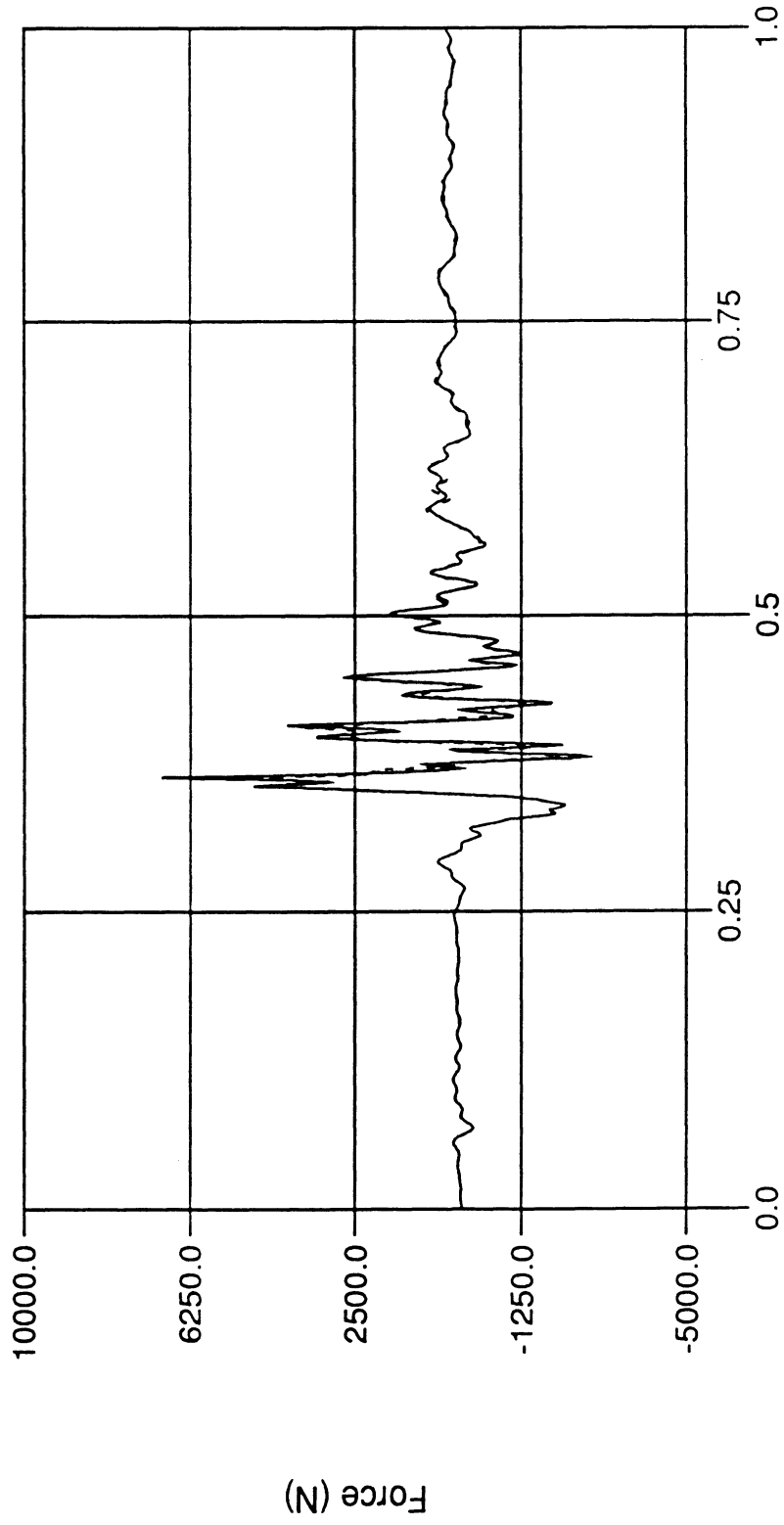
Time (sec.)

Figure 27

DN101 Flexible LCA, Default Mass Lumping
rotation of KRF's about global X-axis

KRF at node 356
KRF at node 121

Rotation (radians)
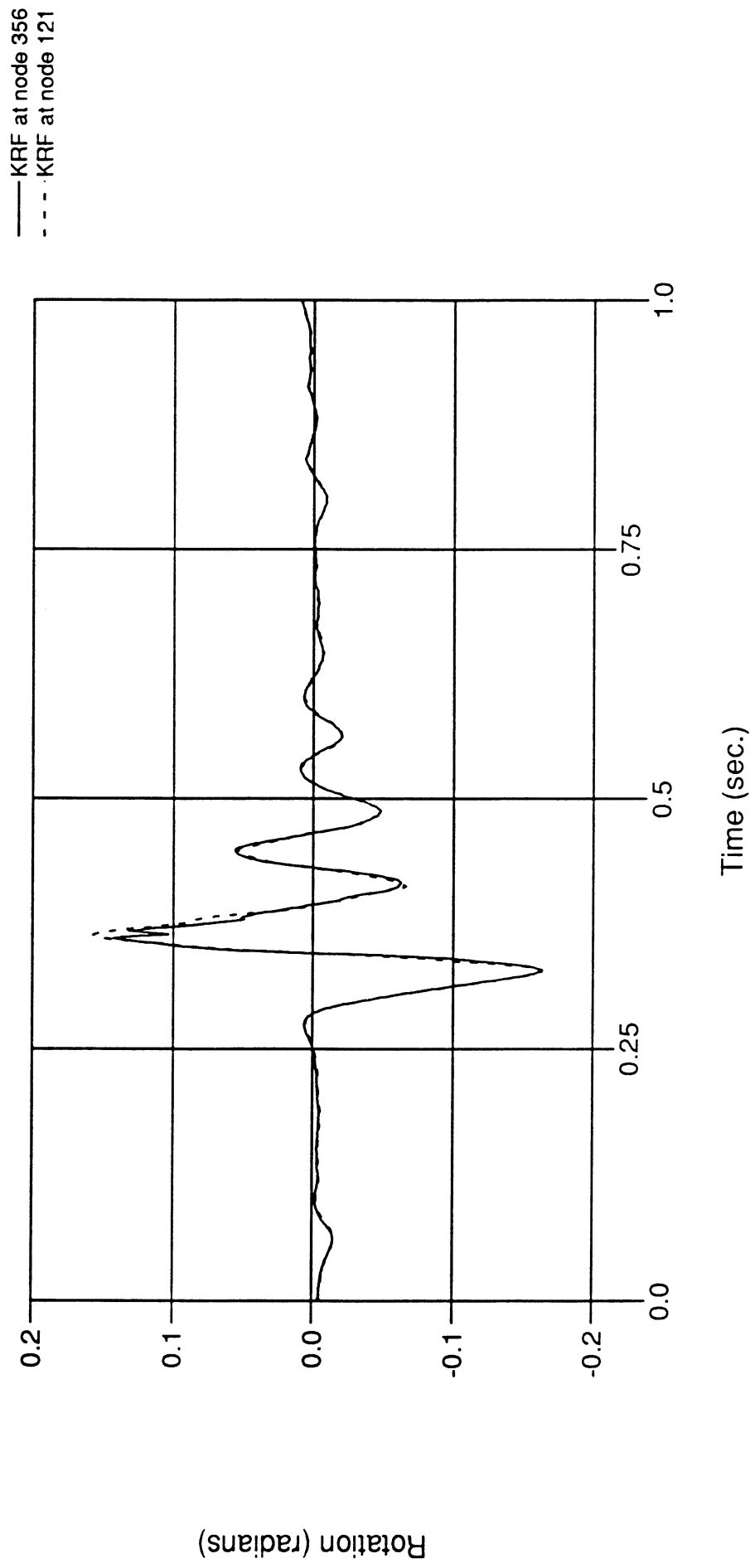
Time (sec.)

Figure 28

DN101 Flexible LCA, Default Mass Lumping
rotation of KRF's about global Y-axis

KRF at node 356
KRF at node 121

Rotation (radians)

0.15
0.1
0.05
0.0
-0.05

0.0   0.25   0.5   0.75   1.0
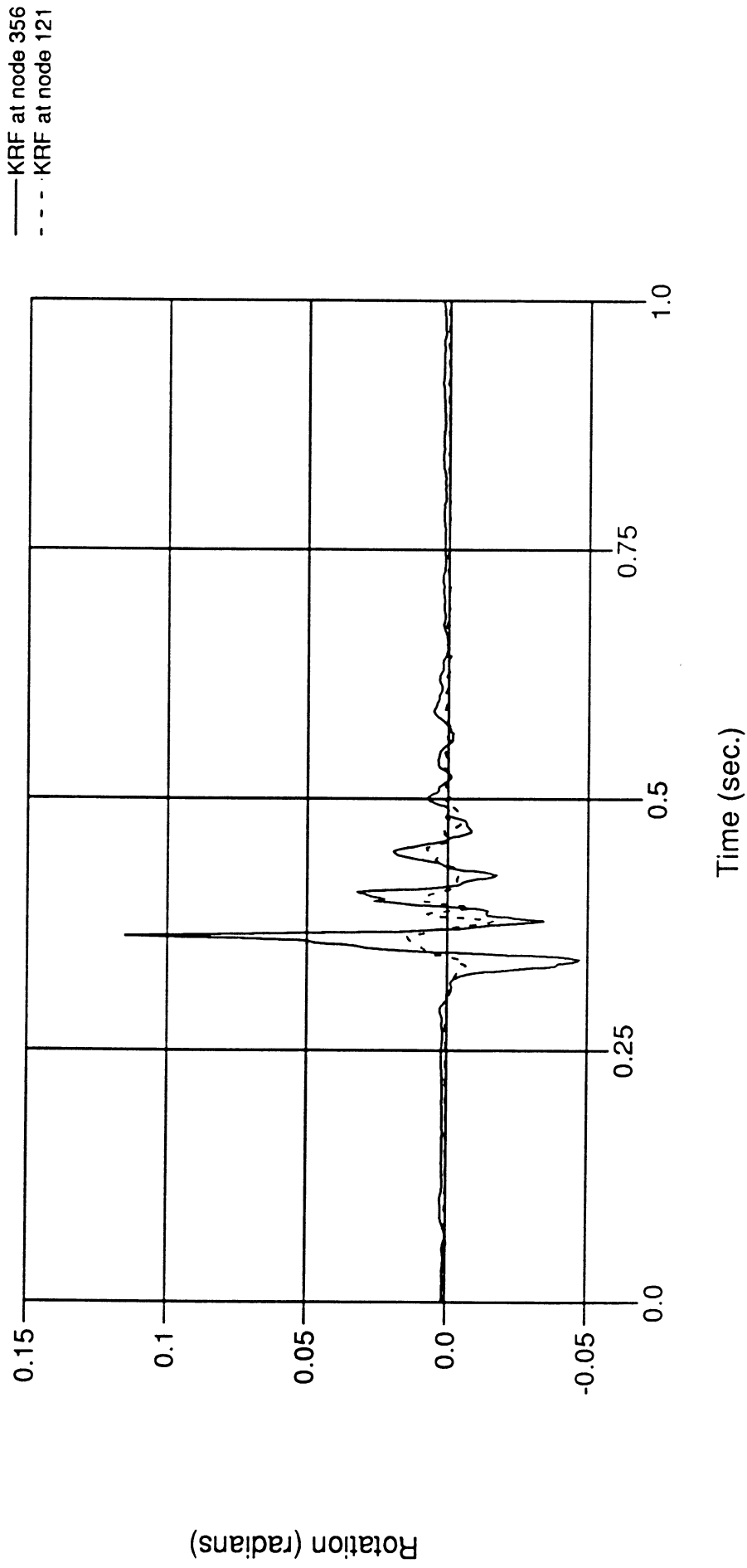
Time (sec.)

Figure 29

DN101 Flexible LCA, Default Mass Lumping

rotation of KRF's about global Z-axis

KRF at node 356
KRF at node 121

Rotation (radians)
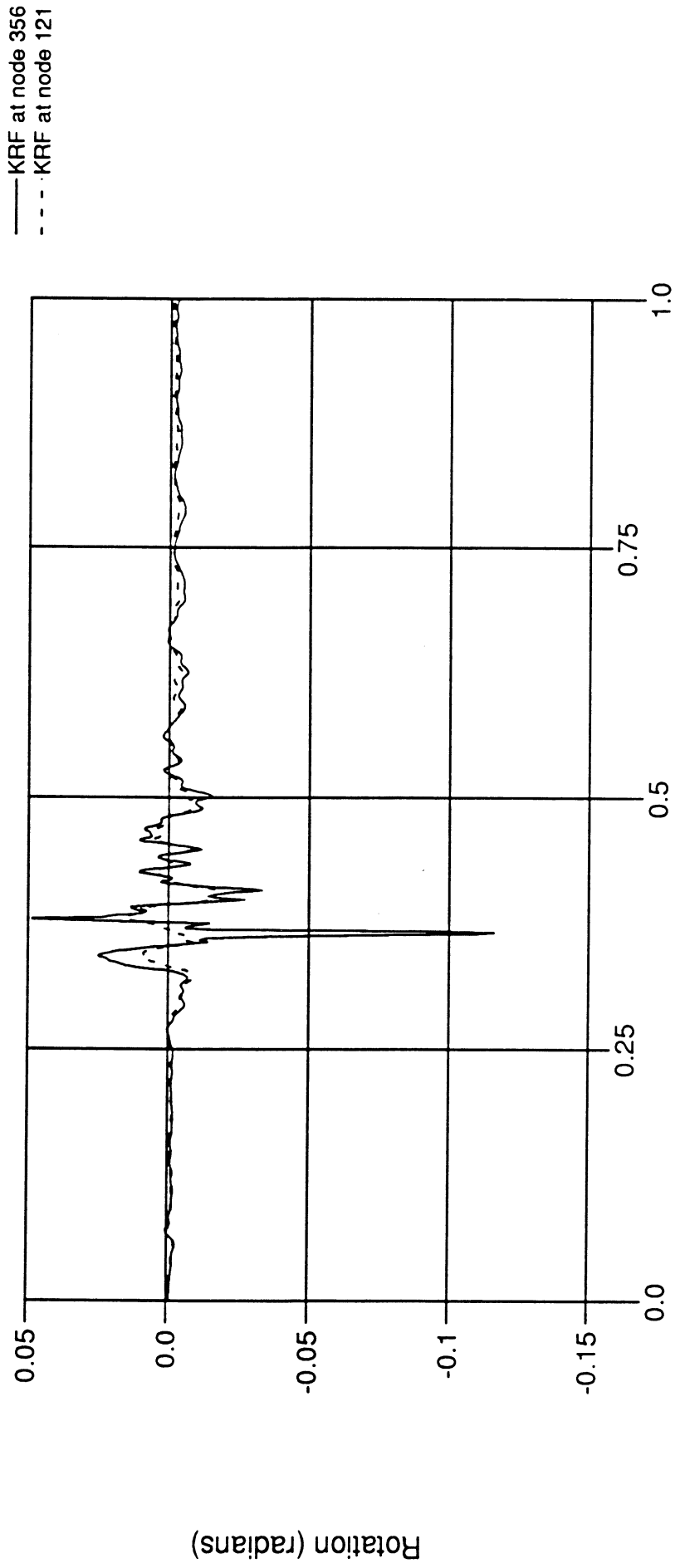
Time (sec.)

Figure 30

DN101 Flexible LCA, Default Mass Lumping
ball joint displacement along the fore-aft direction

—— 3-KRF's
- - - - 1-KRF
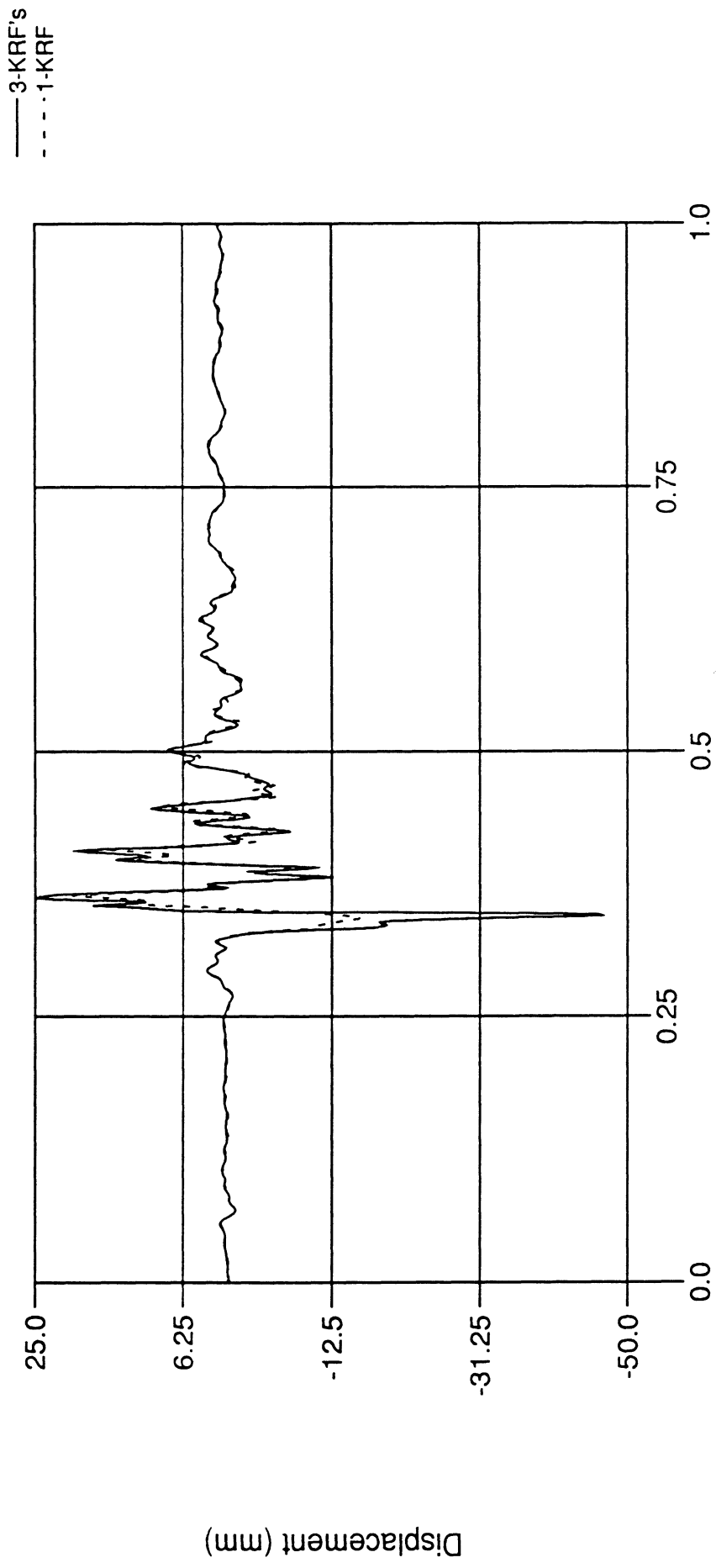
Displacement (mm)

Time (sec.)

Figure 31

DN101 Flexible LCA, Default Mass Lumping

ball joint displacement along the lateral direction

Legend:
— 3-KRF's
- - - 1-KRF
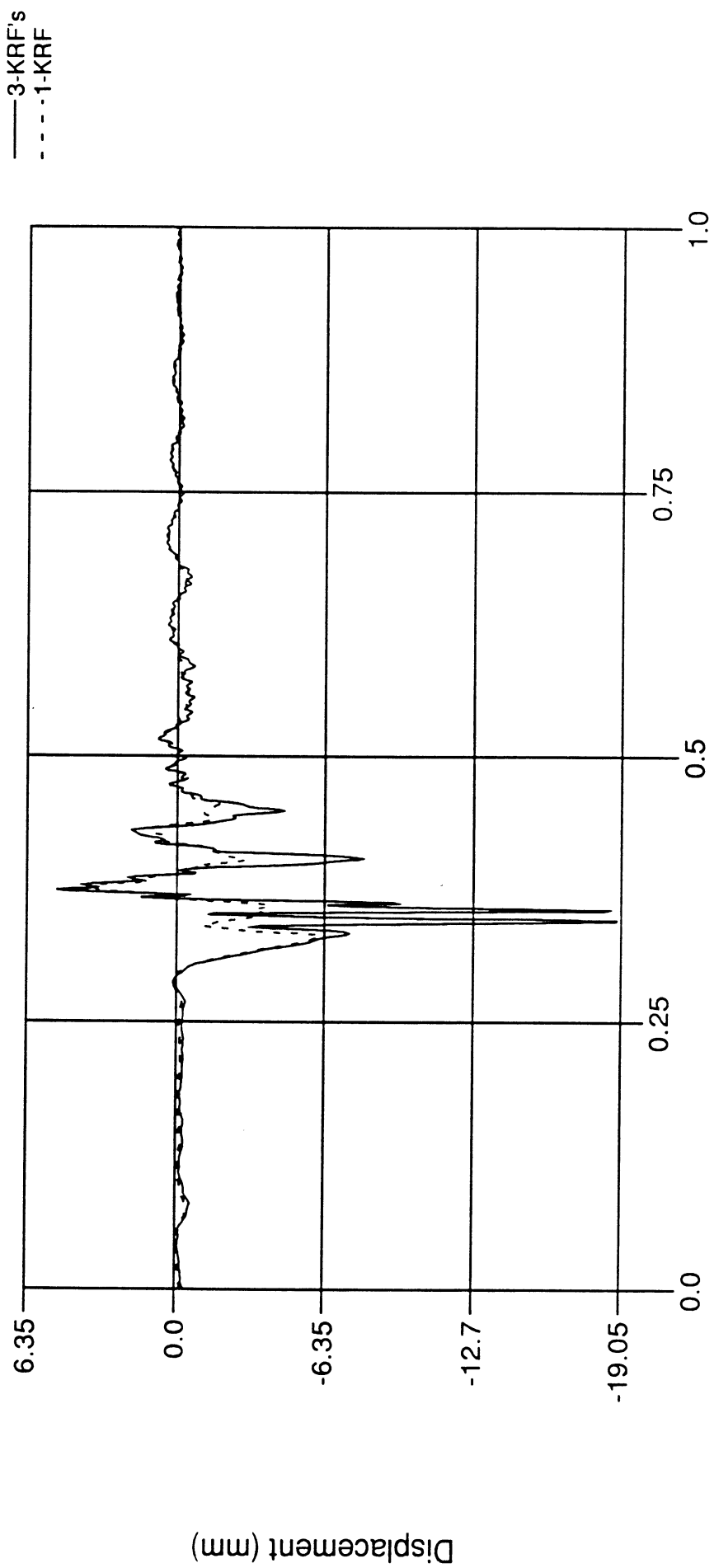
Time (sec.)

Displacement (mm)

Figure 32

DN101 Flexible LCA, Default Mass Lumping
ball joint reaction along the vertical direction

Time (sec.)

Figure 33

Reaction Force (N)

——— 3-KRF's
- - - 1-KRF

DN101 Flexible LCA, Default Mass Lumping
displacement of front bushing along local x-axis

Time (sec.)
Figure 34

3-KRF's
1-KRF

Displacement (mm)

DN101 Flexible LCA, Default Mass Lumping
displacement of front bushing along local y-axis

Time (sec.)

Figure 35

Displacement (mm)

3-KRF's
1-KRF

DN101 Flexible LCA, Default Mass Lumping

displacement of front bushing along local z-axis

Time (sec.)

Figure 36

Displacement (mm)

3-KRF's
- - - -1-KRF
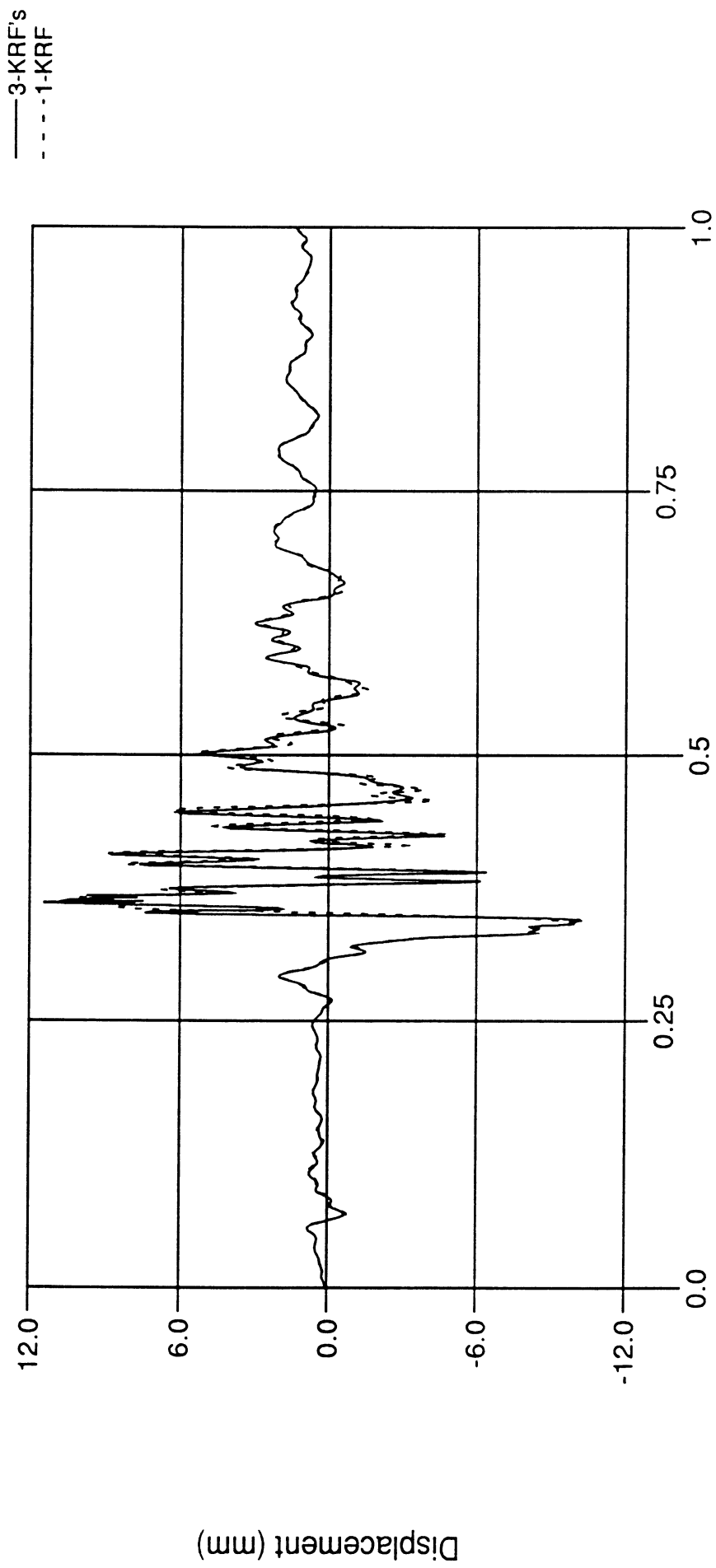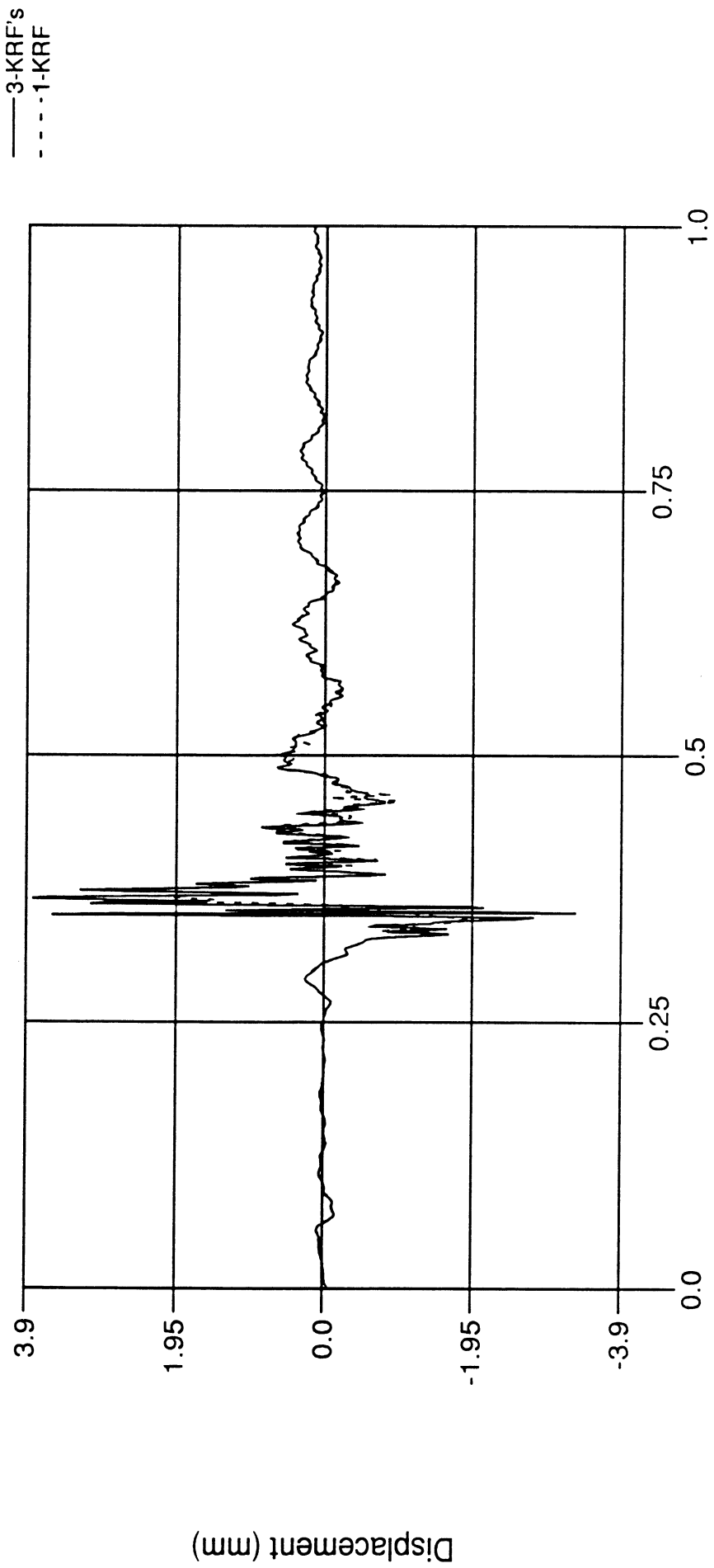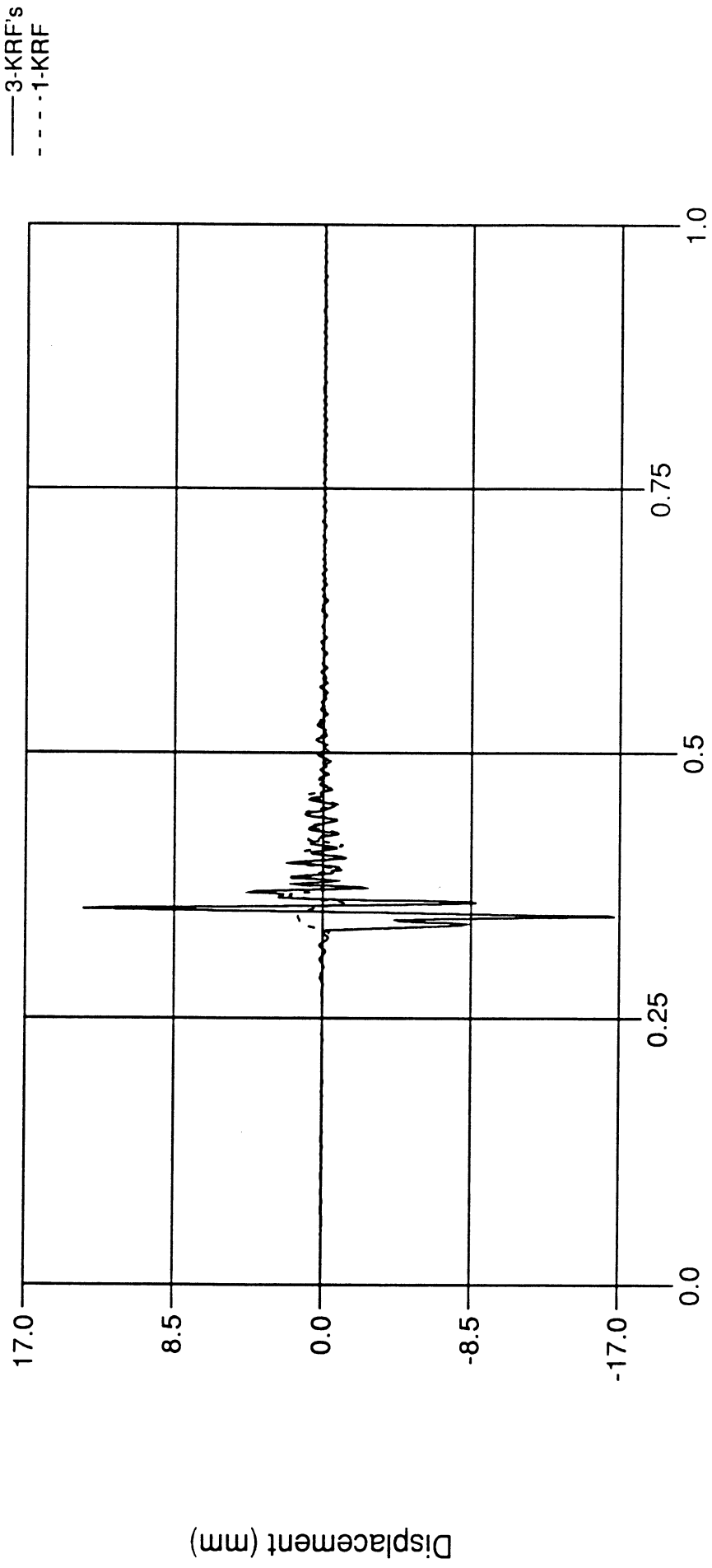
DN101 Flexible LCA, Default Mass Lumping

front bushing radial force along local x-axis
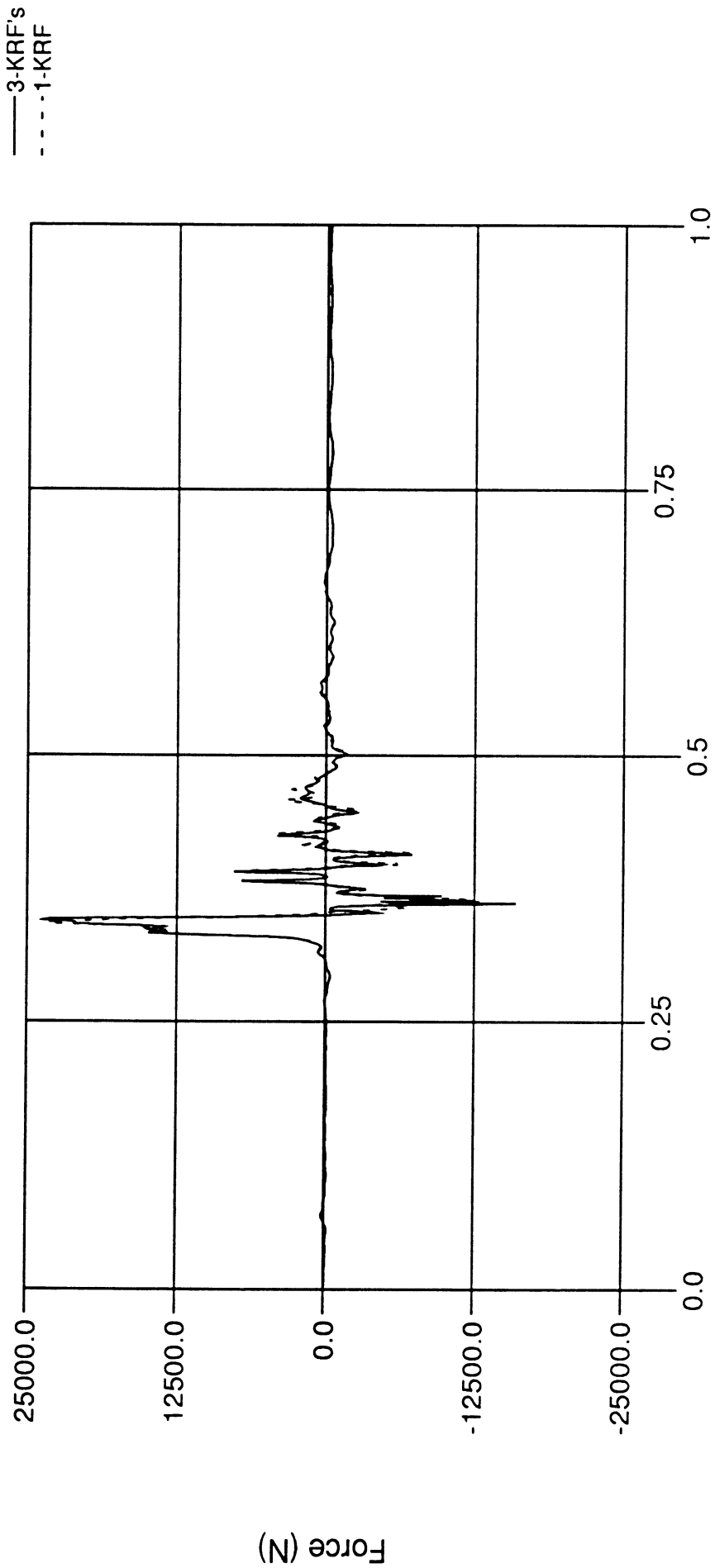
Time (sec.)

Figure 37

DN101 Flexible LCA, Default Mass Lumping
front bushing radial force along local y-axis

3-KRF's
- - - -1-KRF
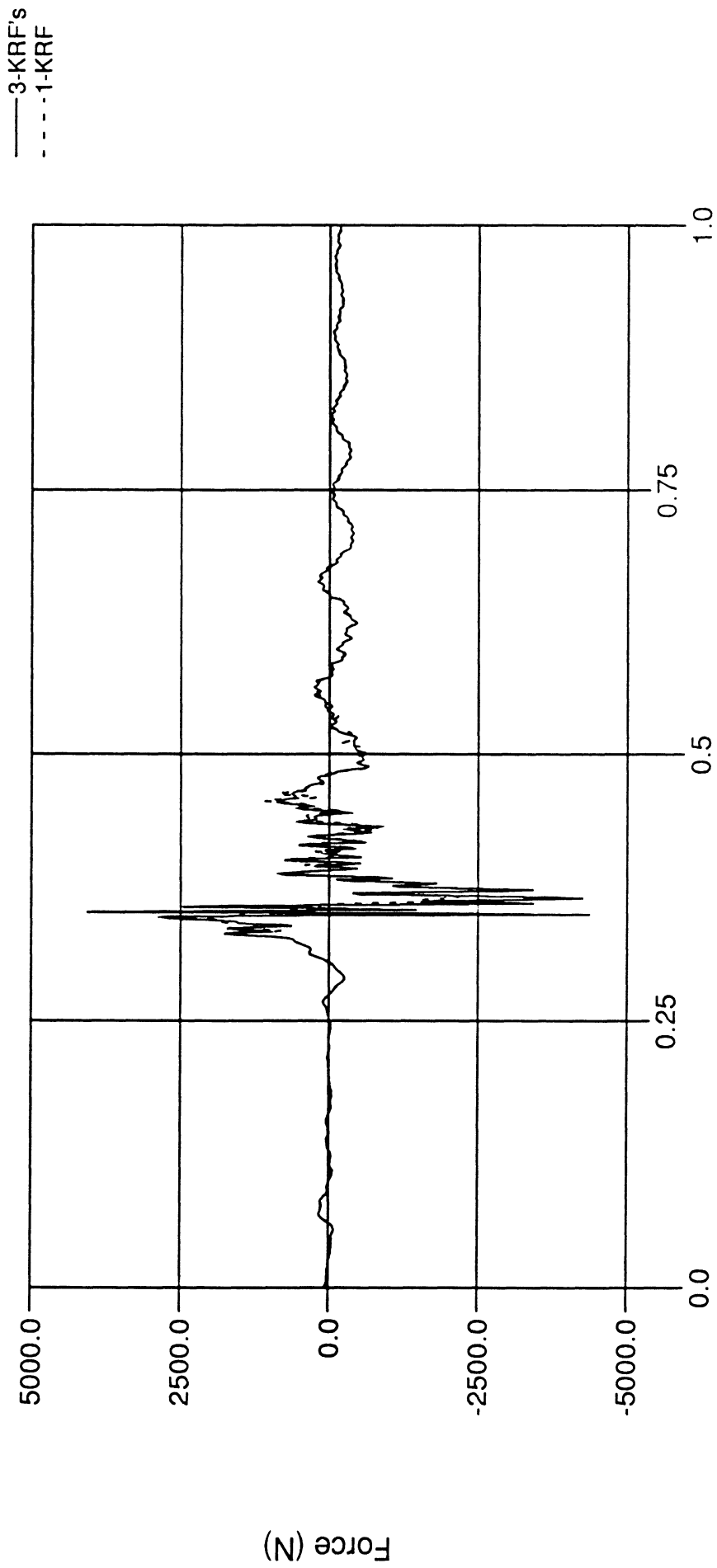
Force (N)

Time (sec.)
Figure 38

DN101 Flexible LCA, Default Mass Lumping
front bushing axial force along local z-axis

3-KRF's
- - -1-KRF

Force (N)

5000.0
2500.0
0.0
-2500.0
-5000.0

0.0   0.25   0.5   0.75   1.0
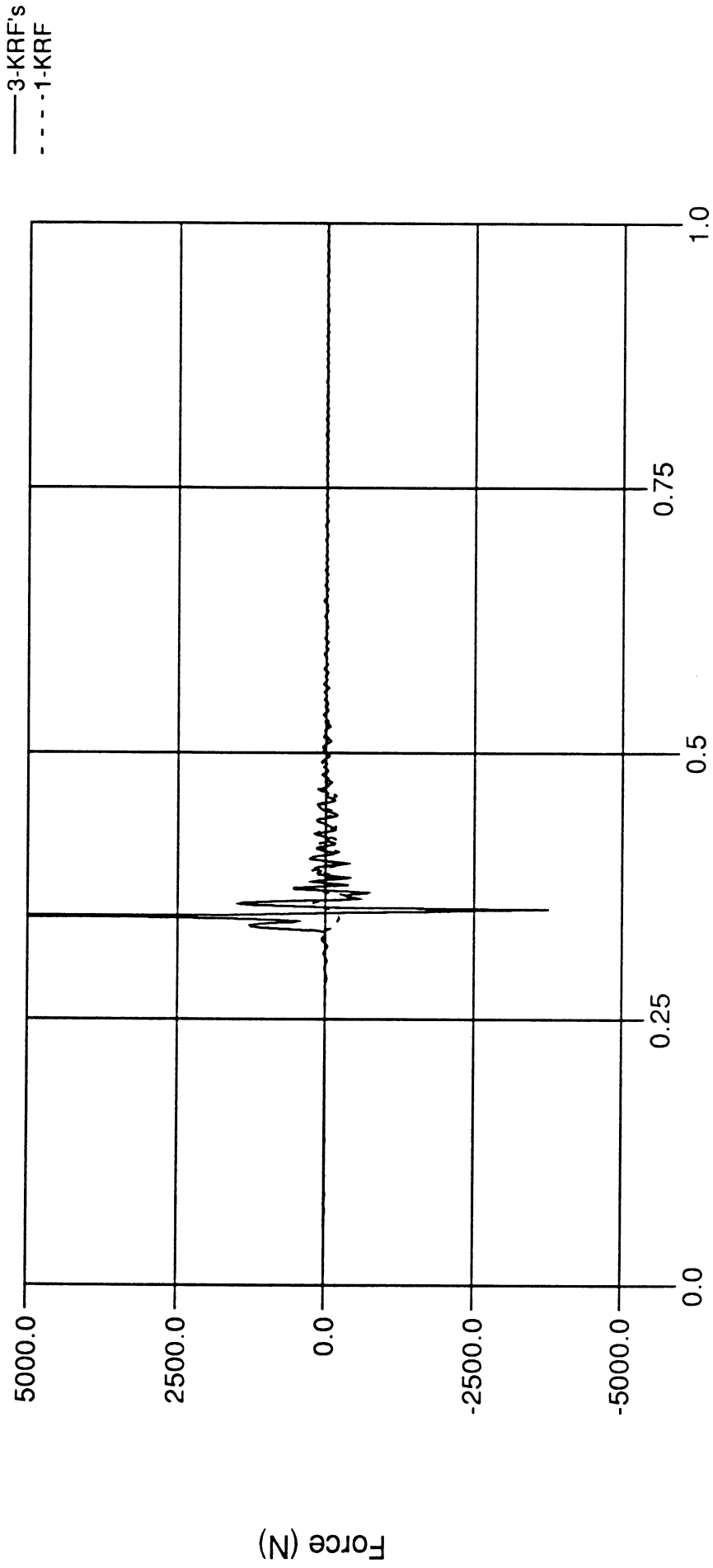
Time (sec.)

Figure 39

DN101 Flexible LCA, Default Mass Lumping

displacement of rear bushing along local x-axis

Time (sec.)

Figure 40

Displacement (mm)

3-KRF's
1-KRF

DN101 Flexible LCA, Default Mass Lumping

displacement of rear bushing along local y-axis

Time (sec.)

Displacement (mm)

3-KRF's
1-KRF

Figure 41

DN101 Flexible LCA, Default Mass Lumping
displacement of rear bushing along local z-axis
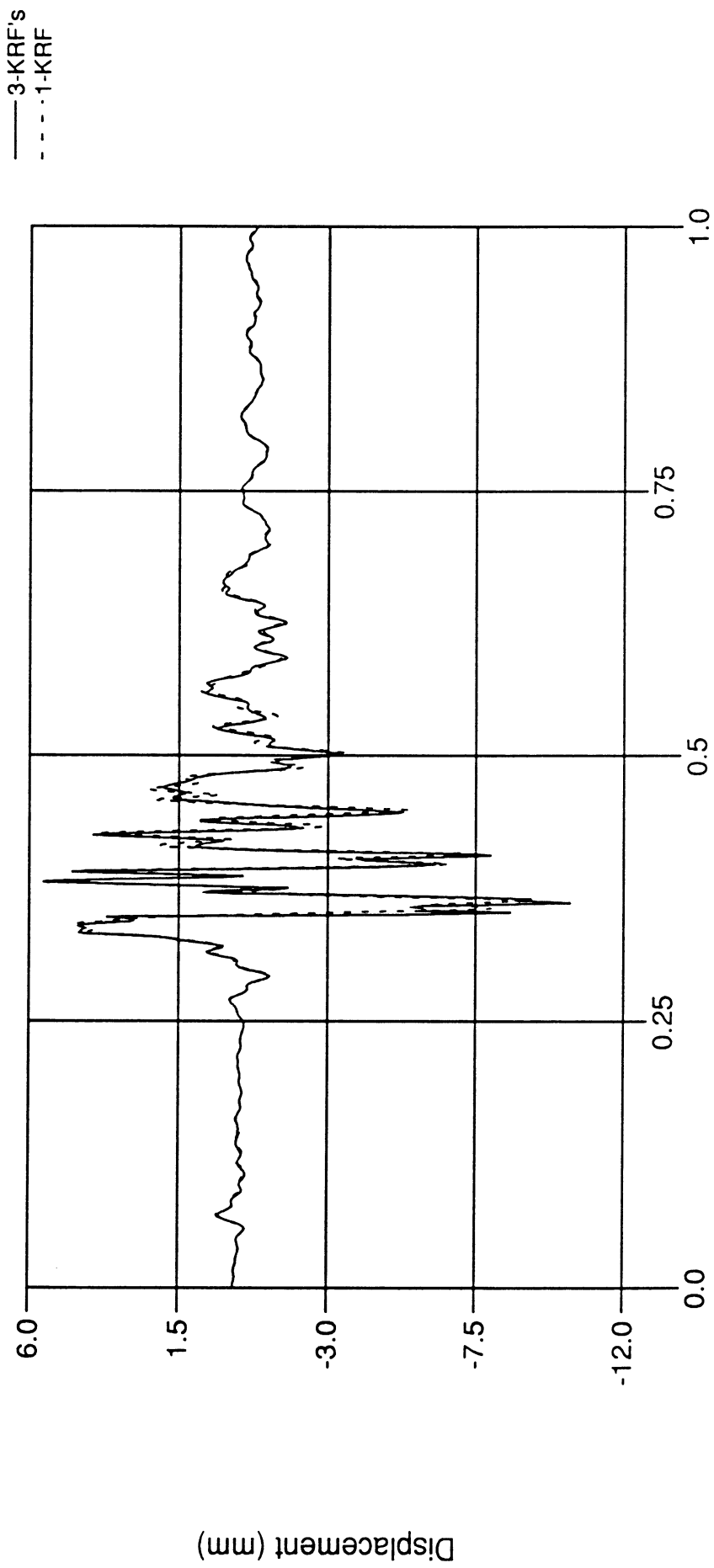
Time (sec.)

Figure 42

DN101 Flexible LCA, Default Mass Lumping
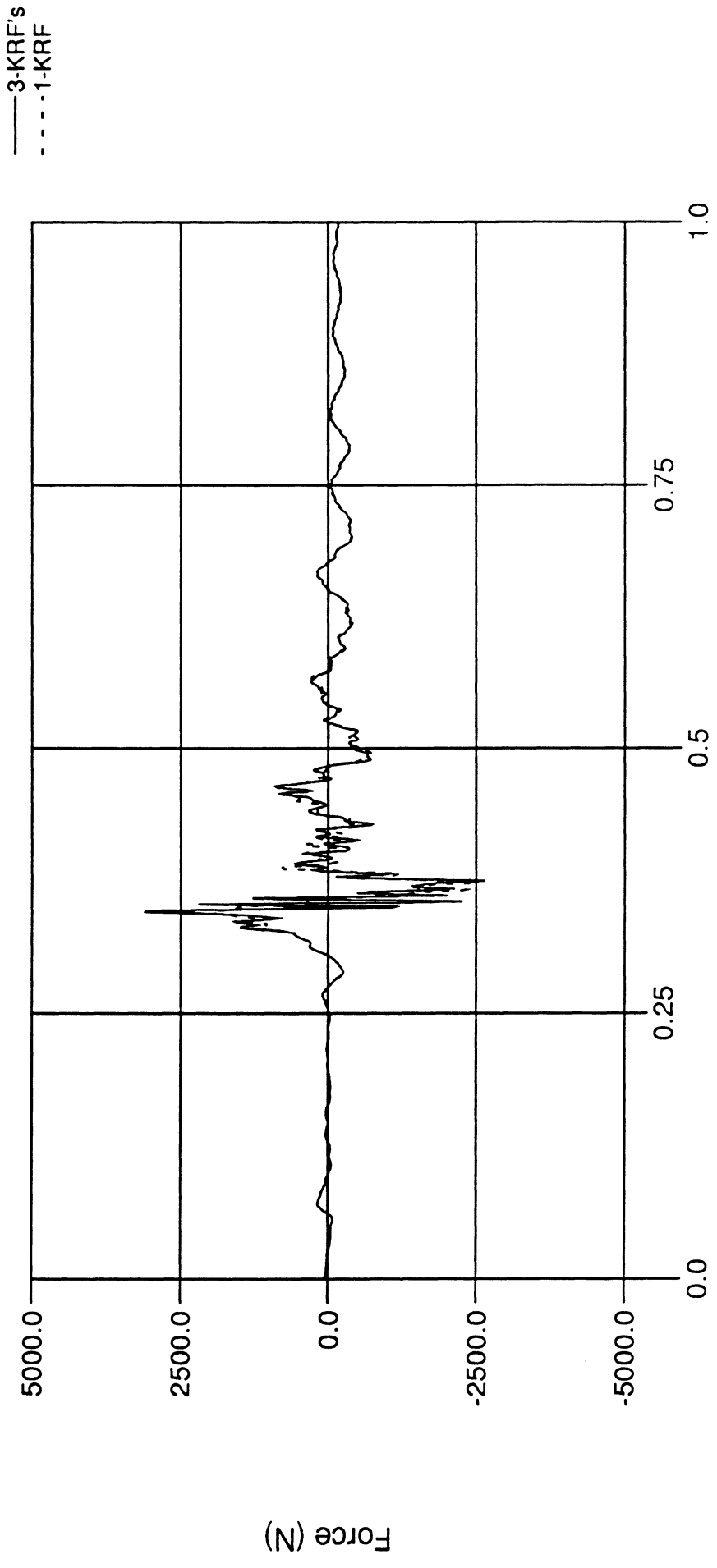rear bushing radial force along local x-axis
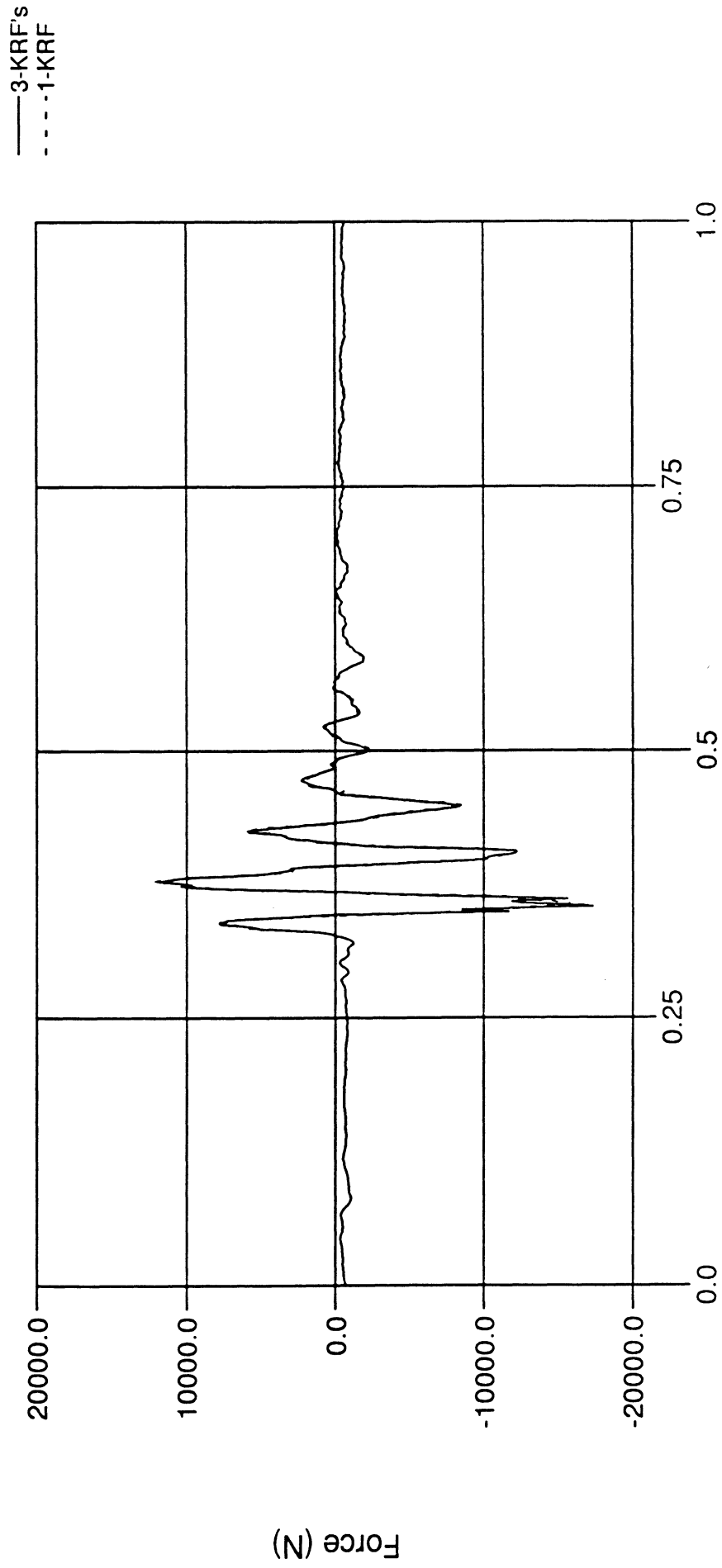
Time (sec.)
Figure 43

3-KRF's
1-KRF

DN101 Flexible LCA, Default Mass Lumping
rear bushing radial force along local y-axis
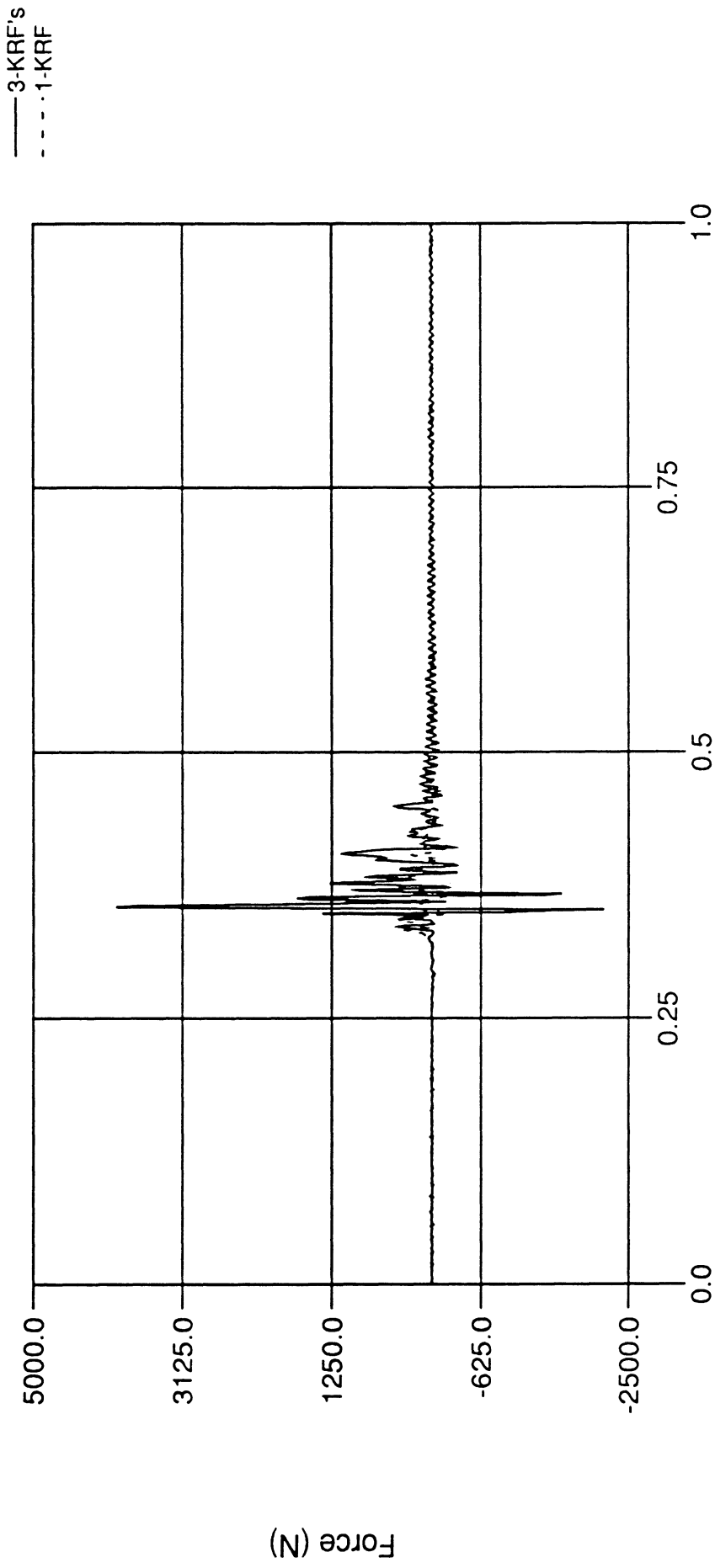
Figure 44

DN101 Flexible LCA, Default Mass Lumping

rear bushing axial force along local z-axis

Time (sec.)

Force (N)

3-KRF's
1-KRF
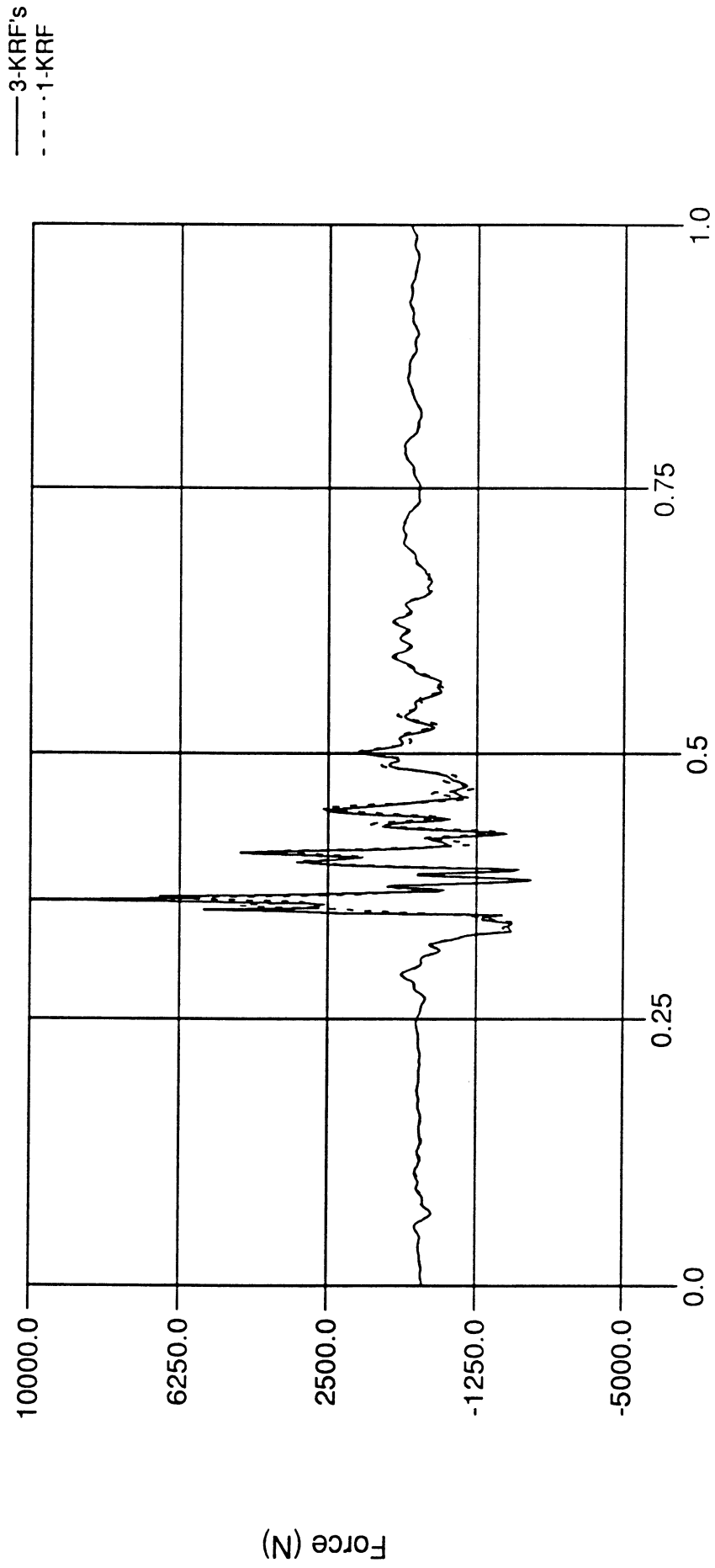
Figure 45

DN101 Flexible LCA, Default Mass Lumping
rotation of KRF's about global X-axis

KRF 1
KRF 2
KRF 3

Rotation (radians)
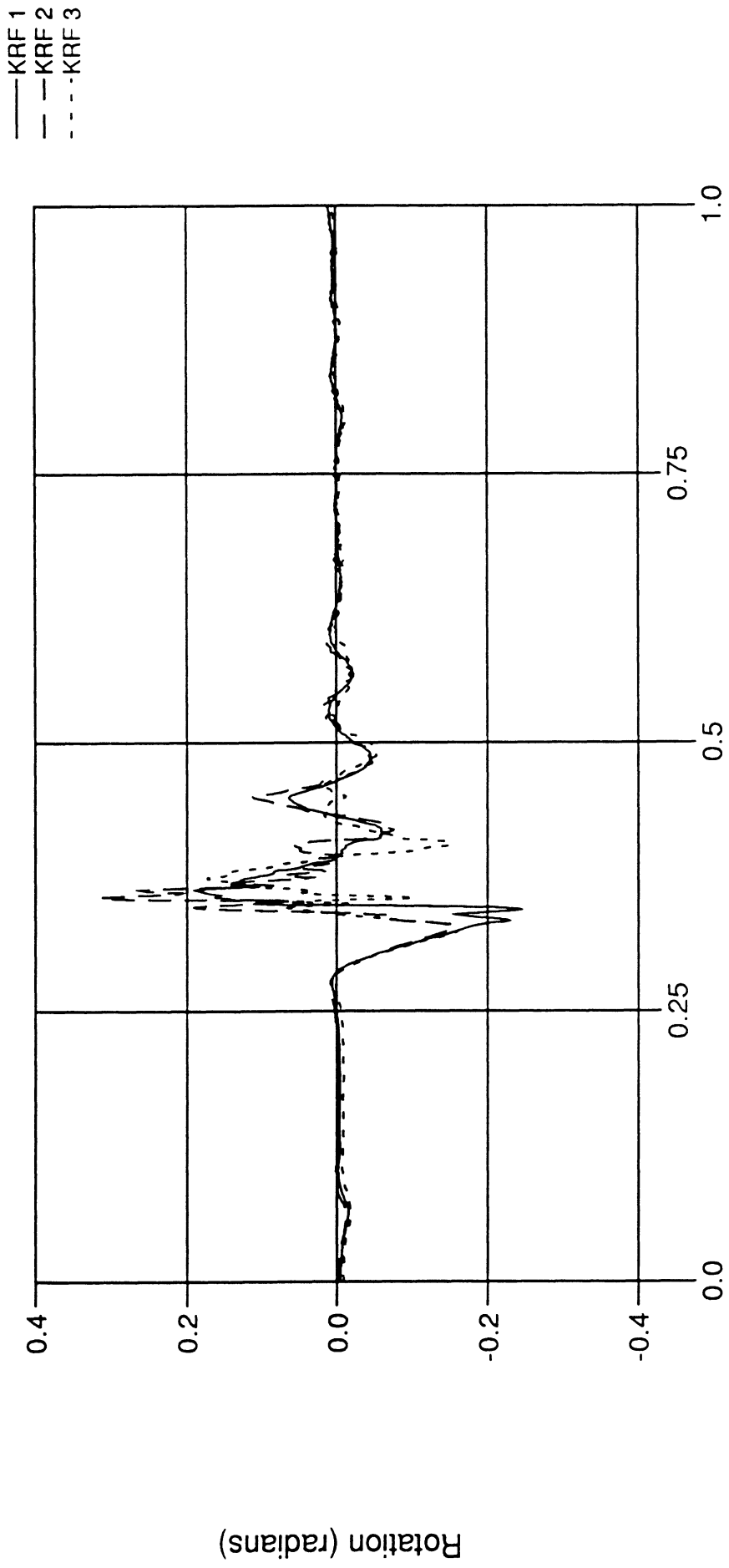
Time (sec.)

Figure 46

DN101 Flexible LCA, Default Mass Lumping

rotation of KRF's about global Y-axis

KRF 1
KRF 2
KRF 3

Rotation (radians)

0.25

0.0625

-0.125

-0.3125

-0.5

0.0   0.25   0.5   0.75   1.0
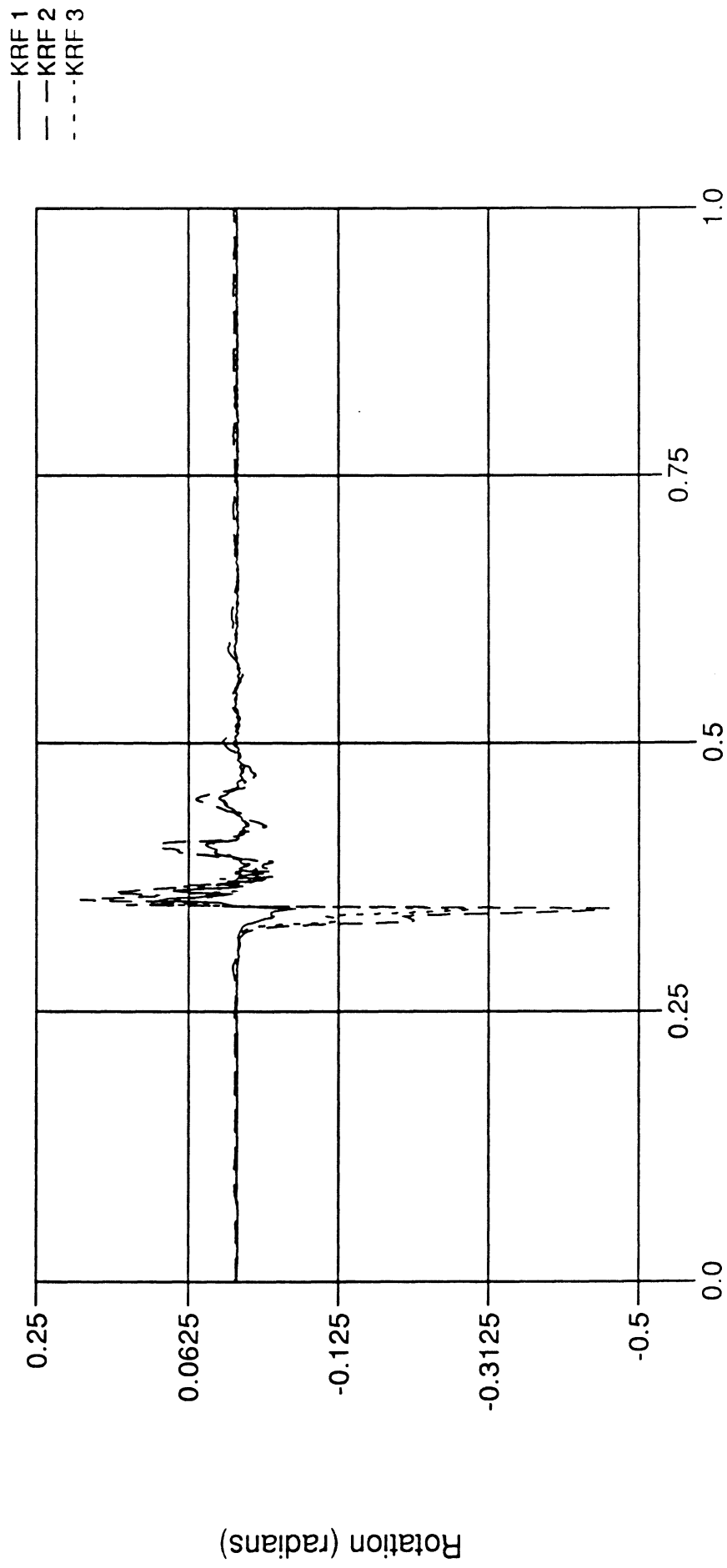
Time (sec.)

Figure 47

DN101 Flexible LCA, Default Mass Lumping

rotation of KRF's about global Z-axis

KRF 1
KRF 2
KRF 3

Rotation (radians)
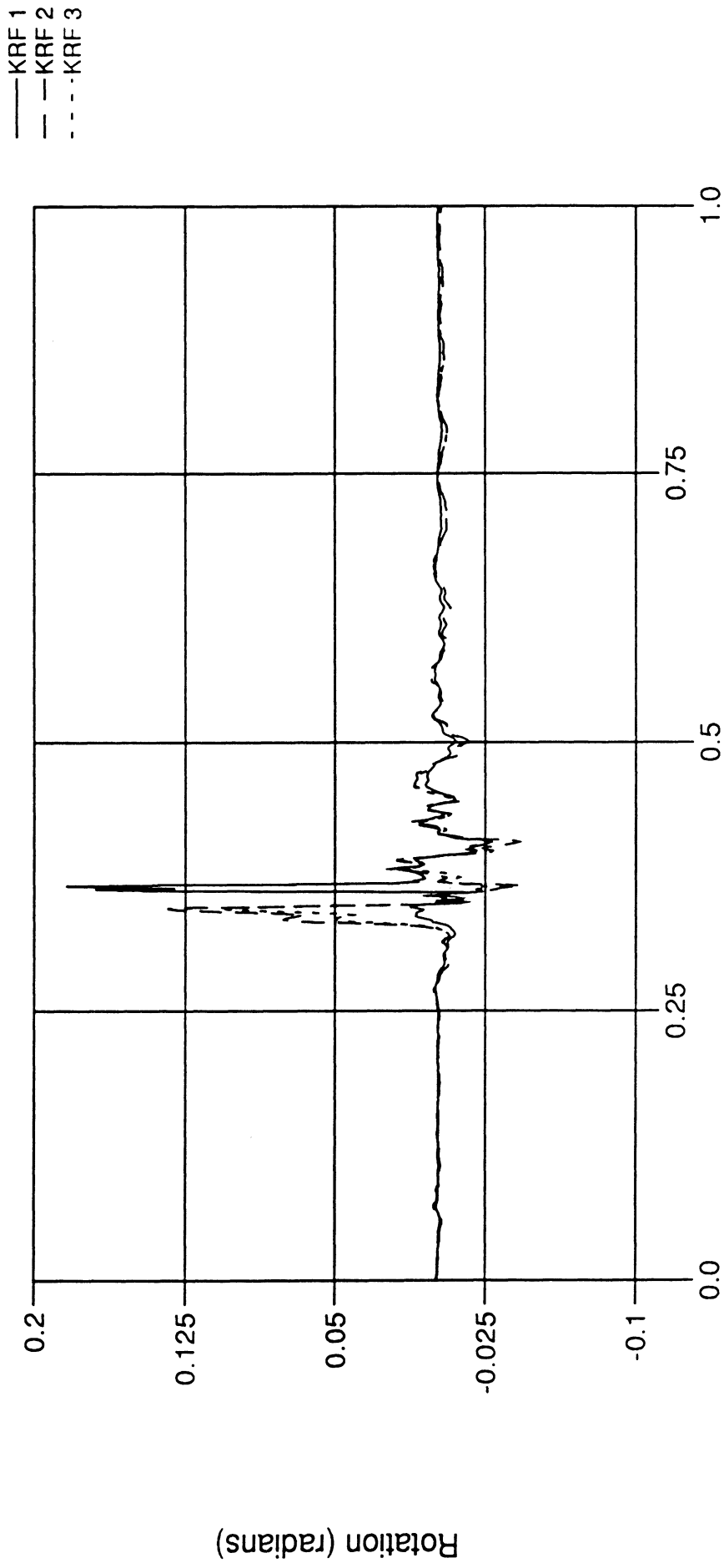
Time (sec.)

Figure 48

DN101 Flexible LCA, Concentrated Mass Method
ball joint displacement along the fore-aft direction

3-KRF's
- - - 1-KRF

Displacement (mm)

25.0
6.25
-12.5
-31.25
-50.0

0.0   0.25   0.5   0.75   1.0
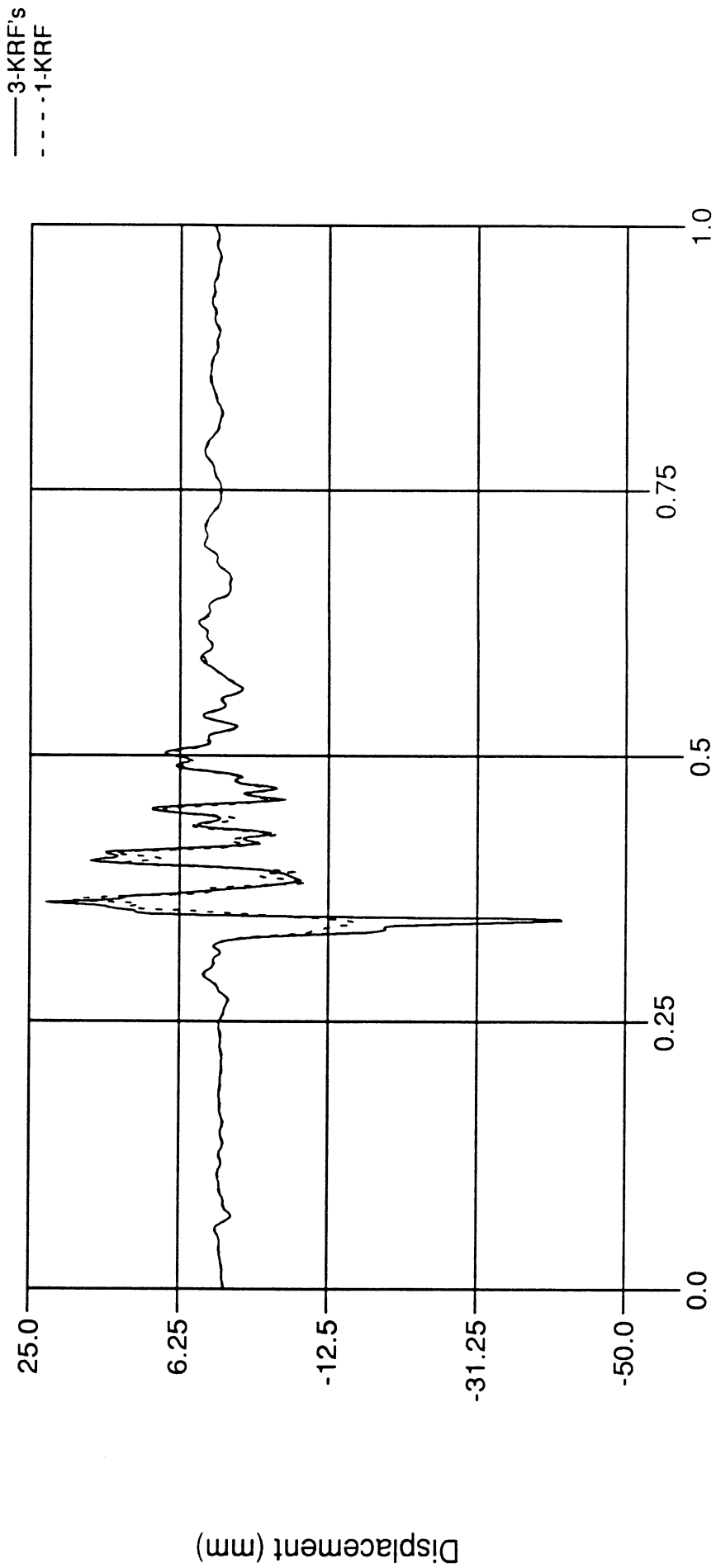
Time (sec.)
Figure 49

DN101 Flexible LCA, Concentrated Mass Method
ball joint displacement along the lateral direction

3-KRF's
1-KRF
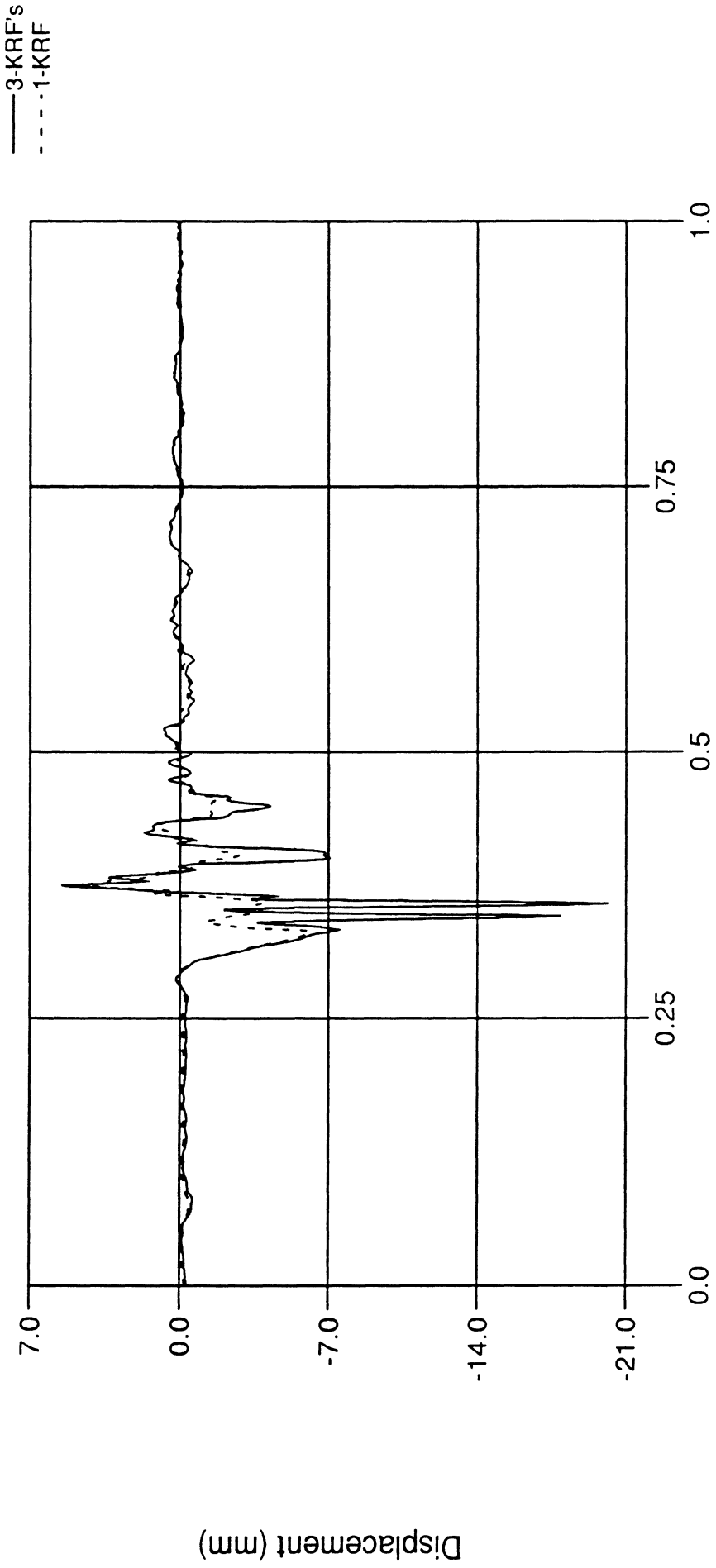
Displacement (mm)

Time (sec.)

Figure 50

DN101 Flexible LCA, Concentrated Mass Method
ball joint reaction along the vertical direction
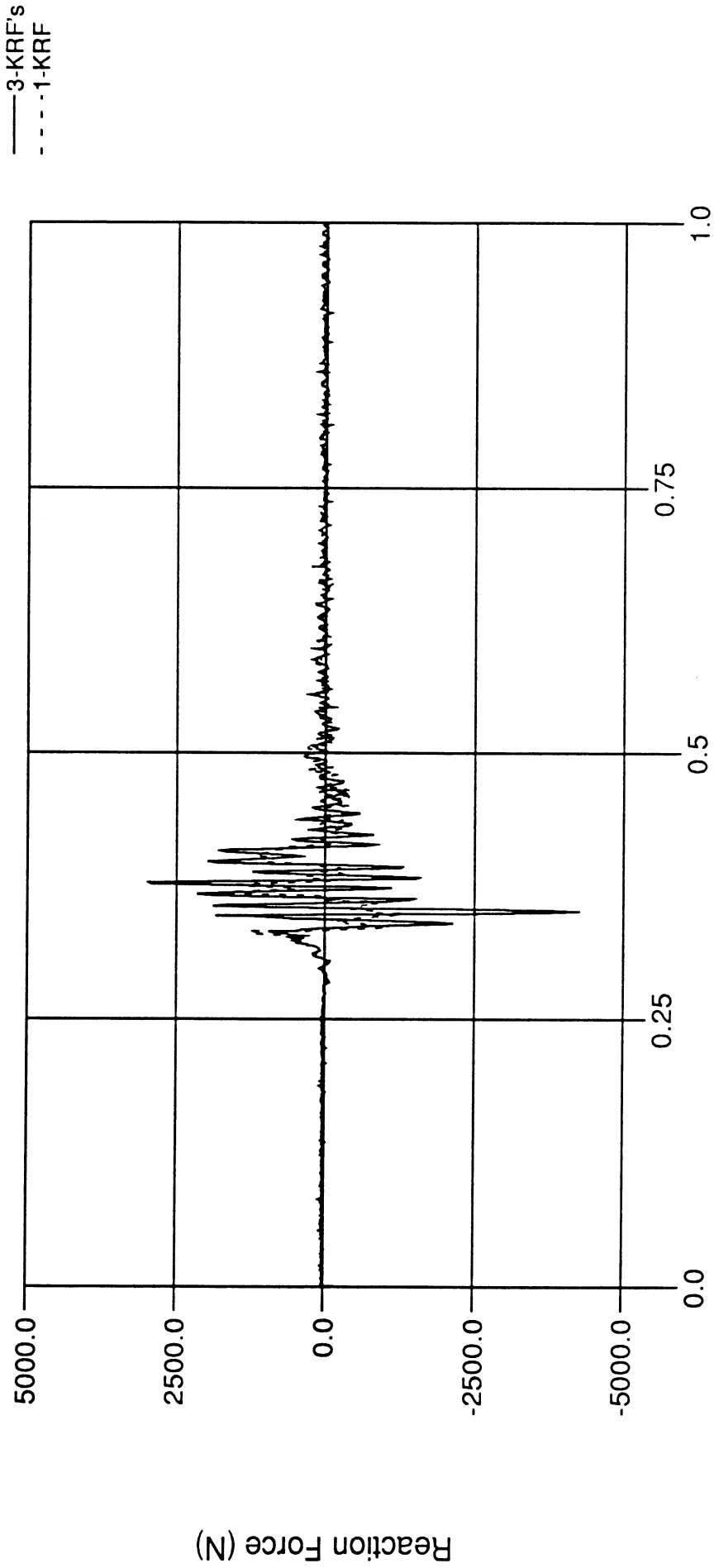
Reaction Force (N)

Time (sec.)

Figure 51

———— 3-KRF's
- - - 1-KRF

DN101 Flexible LCA, Concentrated Mass Method

displacement of front bushing along local x-axis

3-KRF's

1-KRF

Time (sec.)

Figure 52

Displacement (mm)

DN101 Flexible LCA, Concentrated Mass Method
displacement of front bushing along local y-axis

3-KRF's
1-KRF
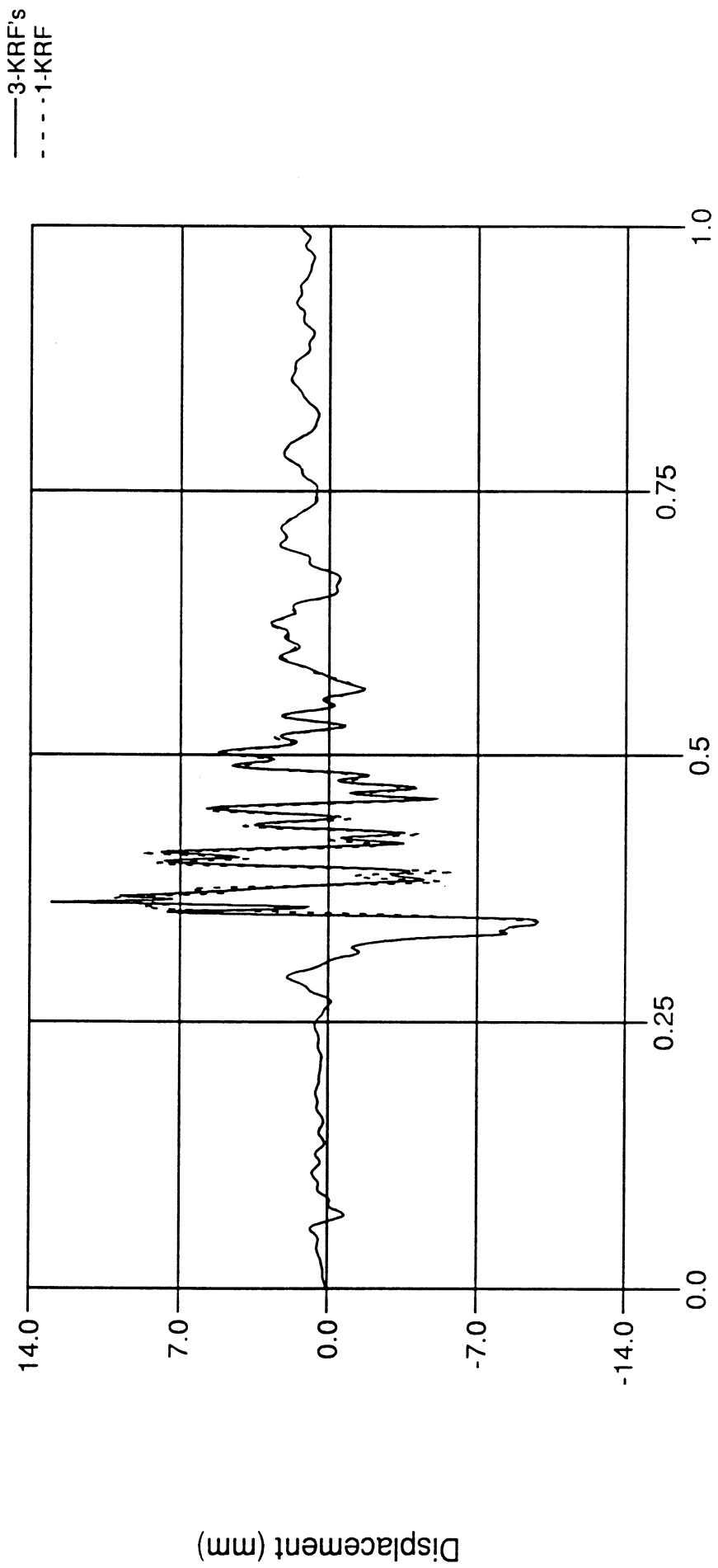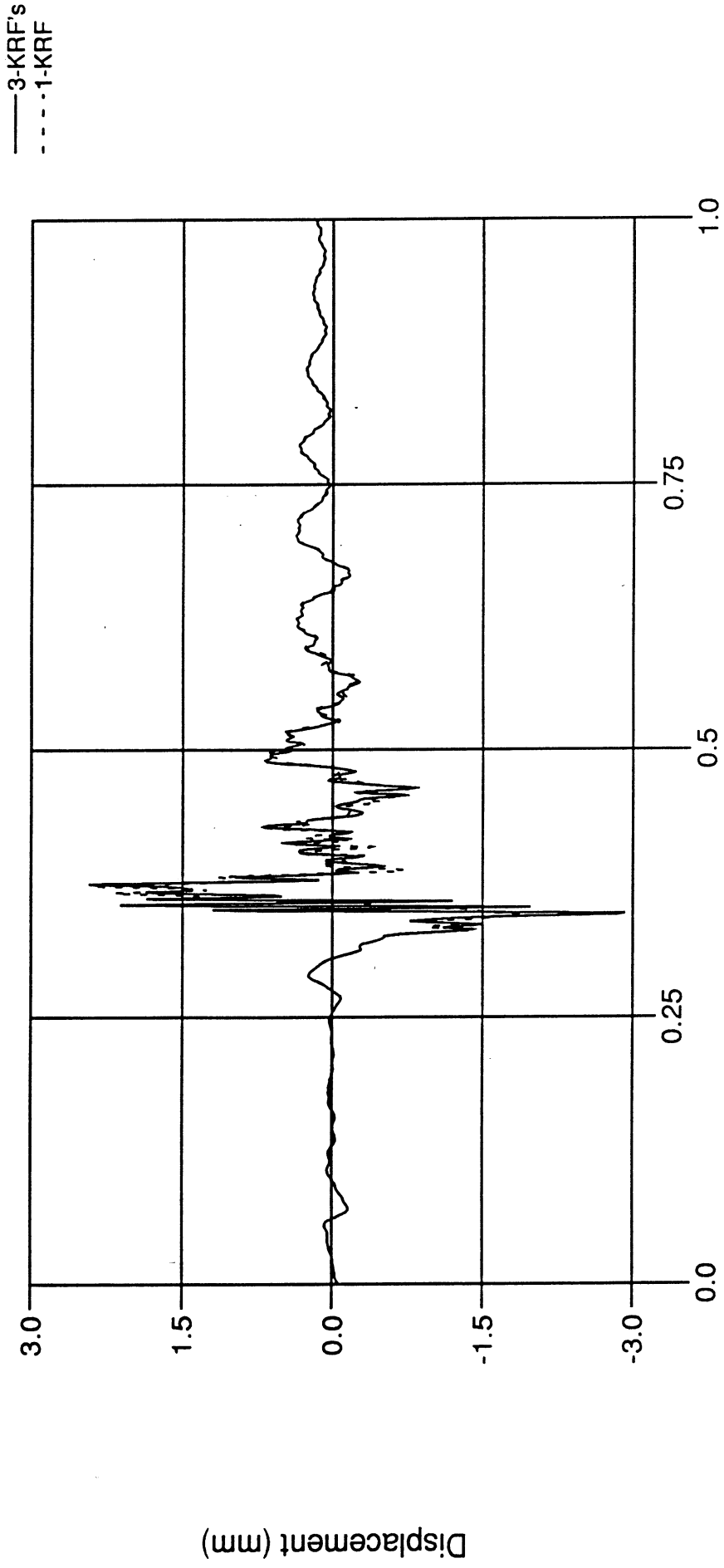
Displacement (mm)

Time (sec.)

Figure 53

DN101 Flexible LCA, Concentrated Mass Method
displacement of front bushing along local z-axis
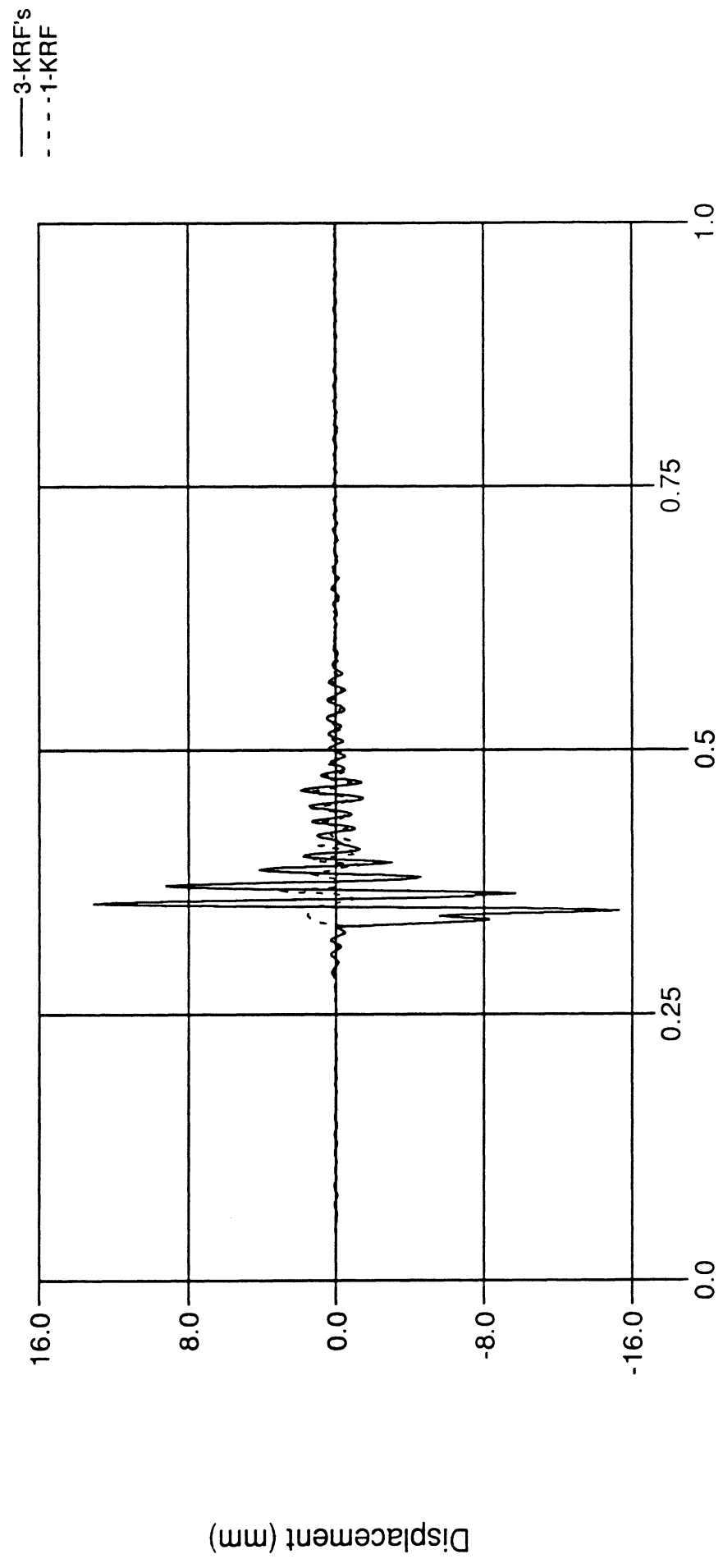
Figure 54

DN101 Flexible LCA, Concentrated Mass Method

front bushing radial force along local x-axis
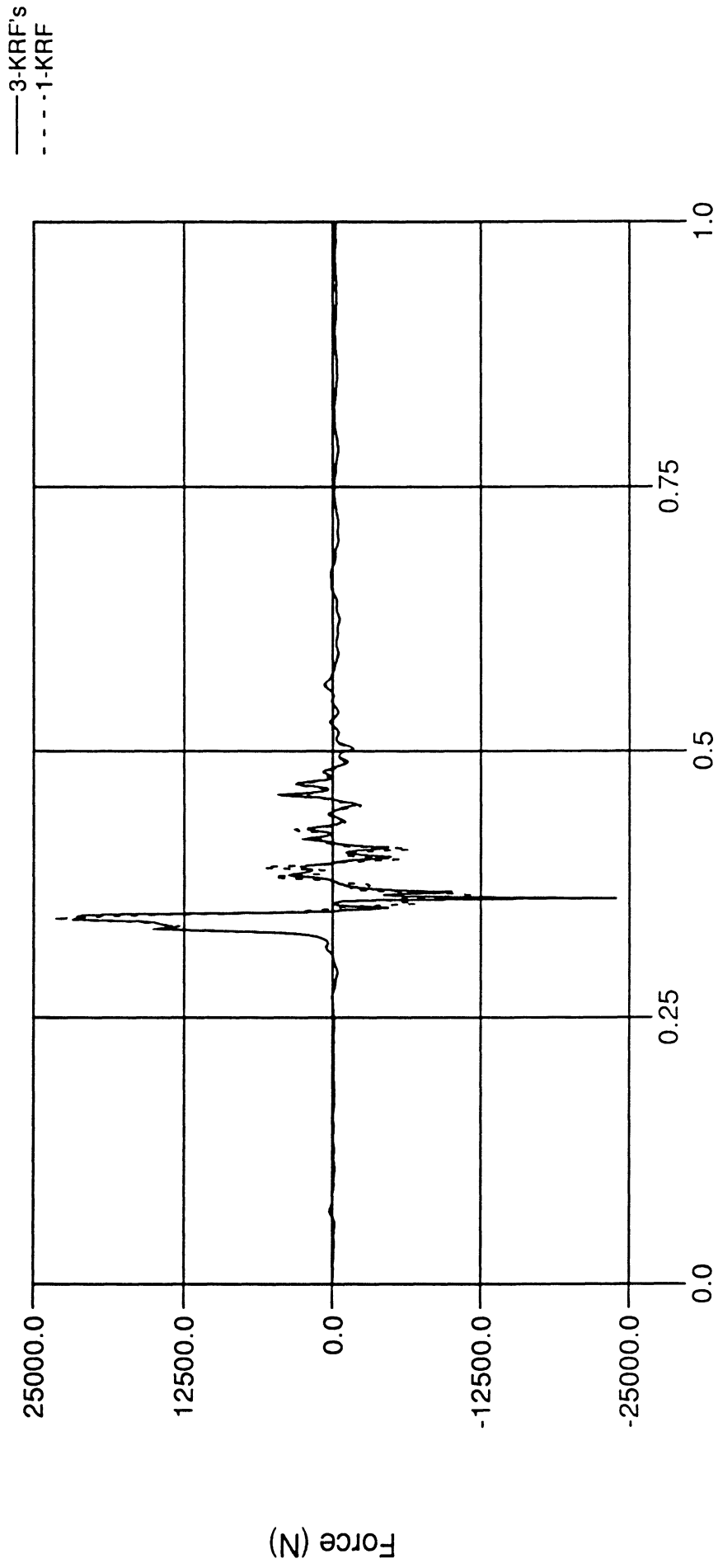
Time (sec.)

Figure 55

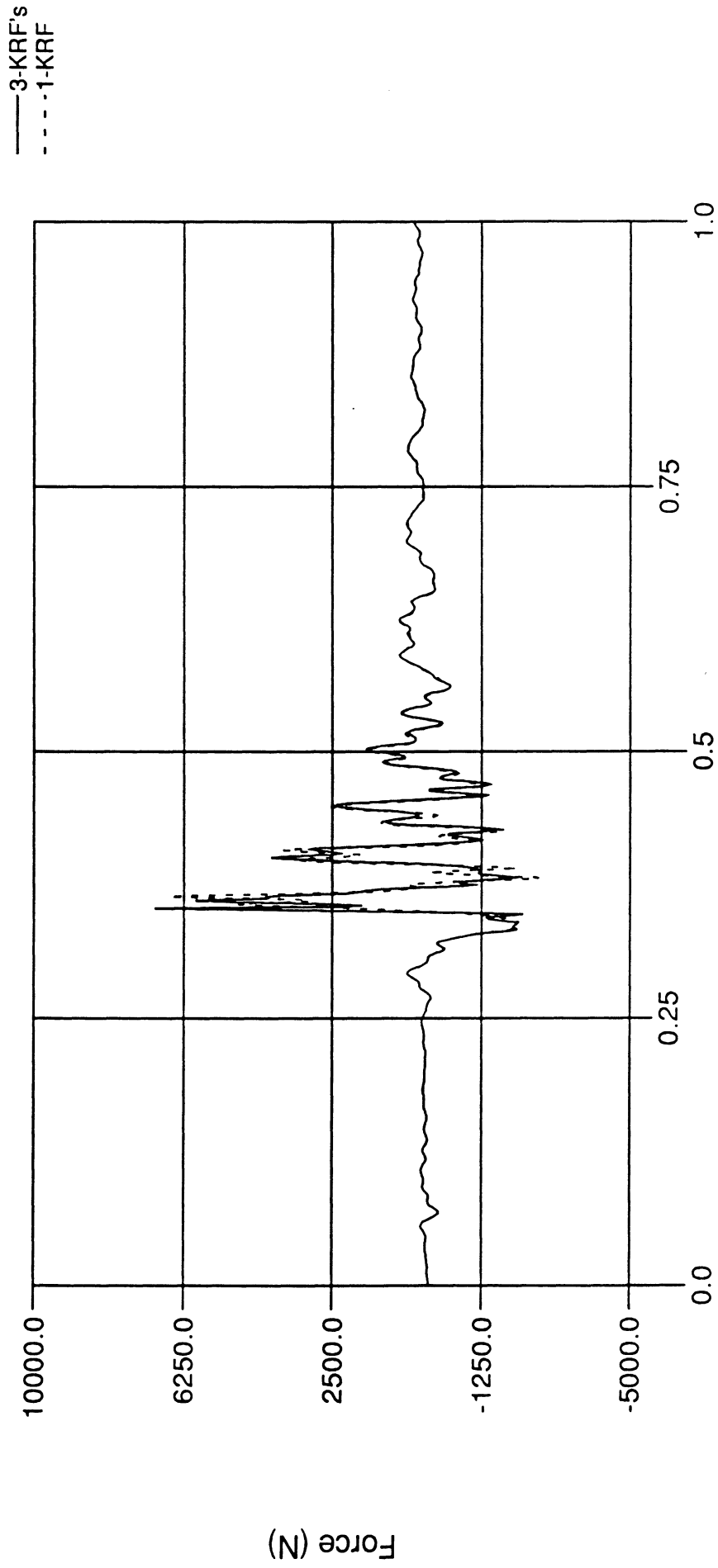DN101 Flexible LCA, Concentrated Mass Method
front bushing radial force along local y-axis

Time (sec.)
Figure 56

DN101 Flexible LCA, Concentrated Mass Method
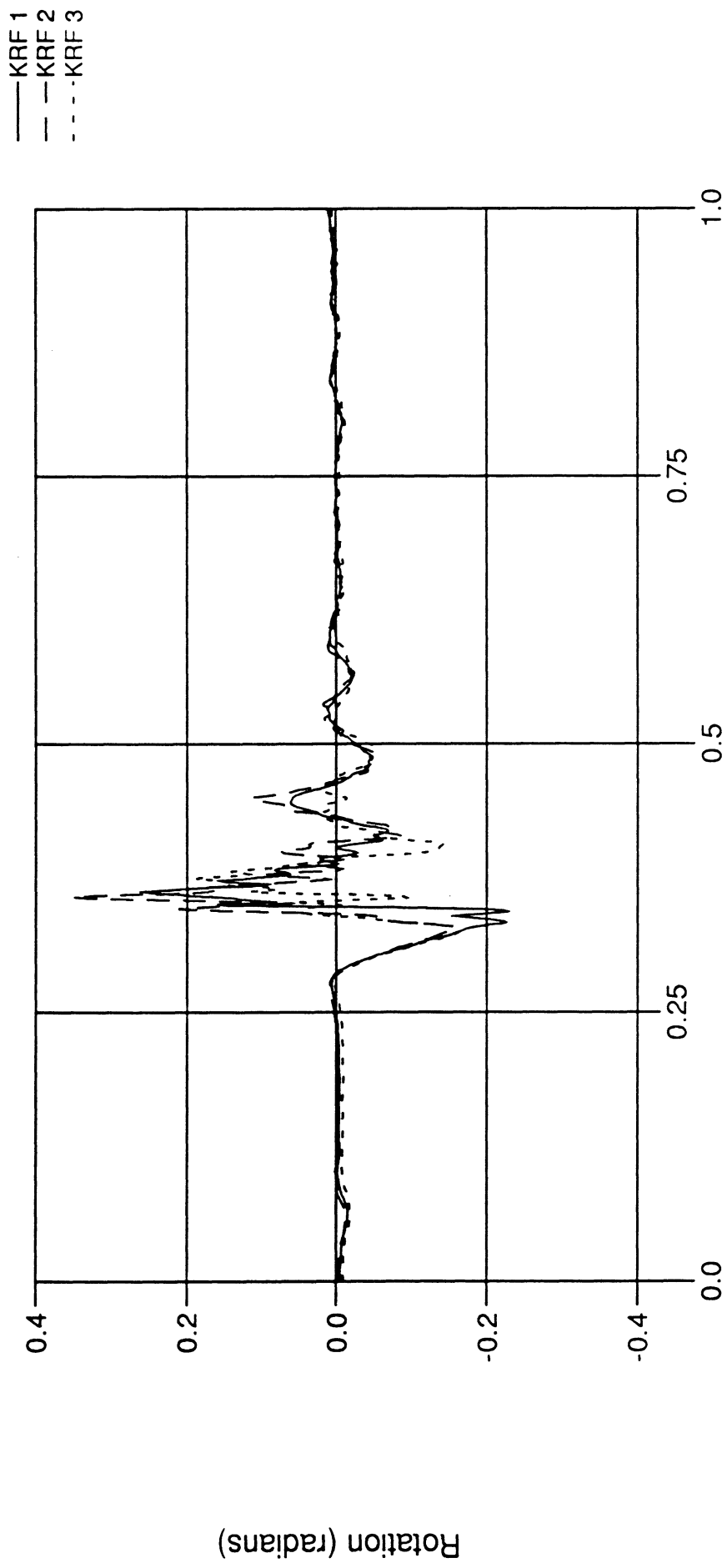
front bushing axial force along local z-axis

3-KRF's
- - - -1-KRF

Force (N)
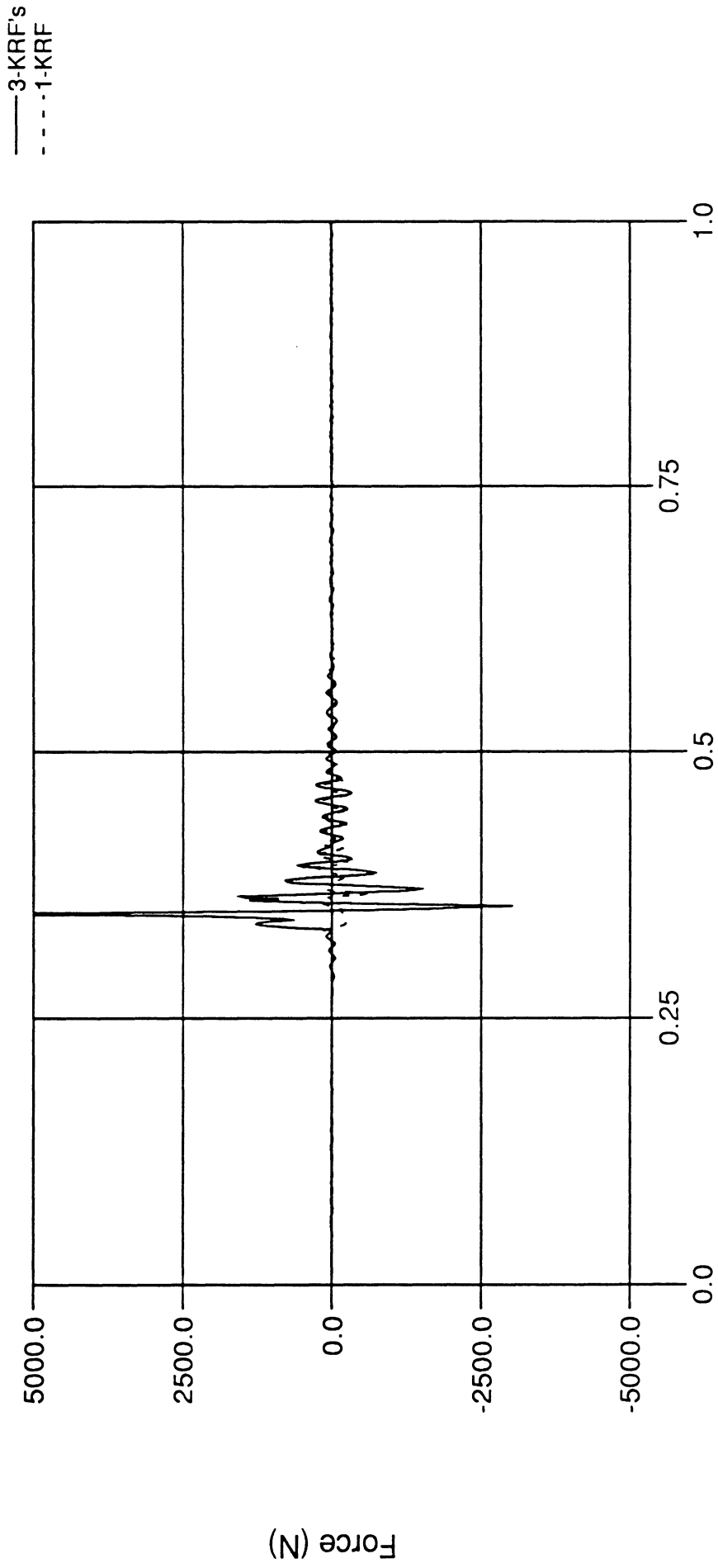
Time (sec.)

Figure 57

DN101 Flexible LCA, Concentrated Mass Method

displacement of rear bushing along local x-axis

Time (sec.)

Figure 58

Legend:
- 3-KRF's
- 1-KRF

DN101 Flexible LCA, Concentrated Mass Method

displacement of rear bushing along local y-axis

Time (sec.)

Figure 59

Legend:
3-KRF's
1-KRF

DN101 Flexible LCA, Concentrated Mass Method

displacement of rear bushing along local z-axis

Time (sec.)

Figure 60

Displacement (mm)

3-KRF's
1-KRF

DN101 Flexible LCA, Concentrated Mass Method

rear bushing radial force along local x-axis

Force (N)

Time (sec.)

Figure 61

3-KRF's
- - - -1-KRF

DN101 Flexible LCA, Concentrated Mass Method

rear bushing radial force along local y-axis

Time (sec.)

Figure 62

Legend:
- 3-KRF's
- 1-KRF

Force (N)

Y-axis values: 5000.0, 3125.0, 1250.0, -625.0, -2500.0

X-axis values: 0.0, 0.25, 0.5, 0.75, 1.0

DN101 Flexible LCA, Concentrated Mass Method
rear bushing axial force along local z-axis

Time (sec.)

Figure 63

Force (N)

——— 3-KRF's
- - - 1-KRF

DN101 Flexible LCA, Concentrated Mass Method

rotation of KRF's about global X-axis

KRF 1
KRF 2
KRF 3
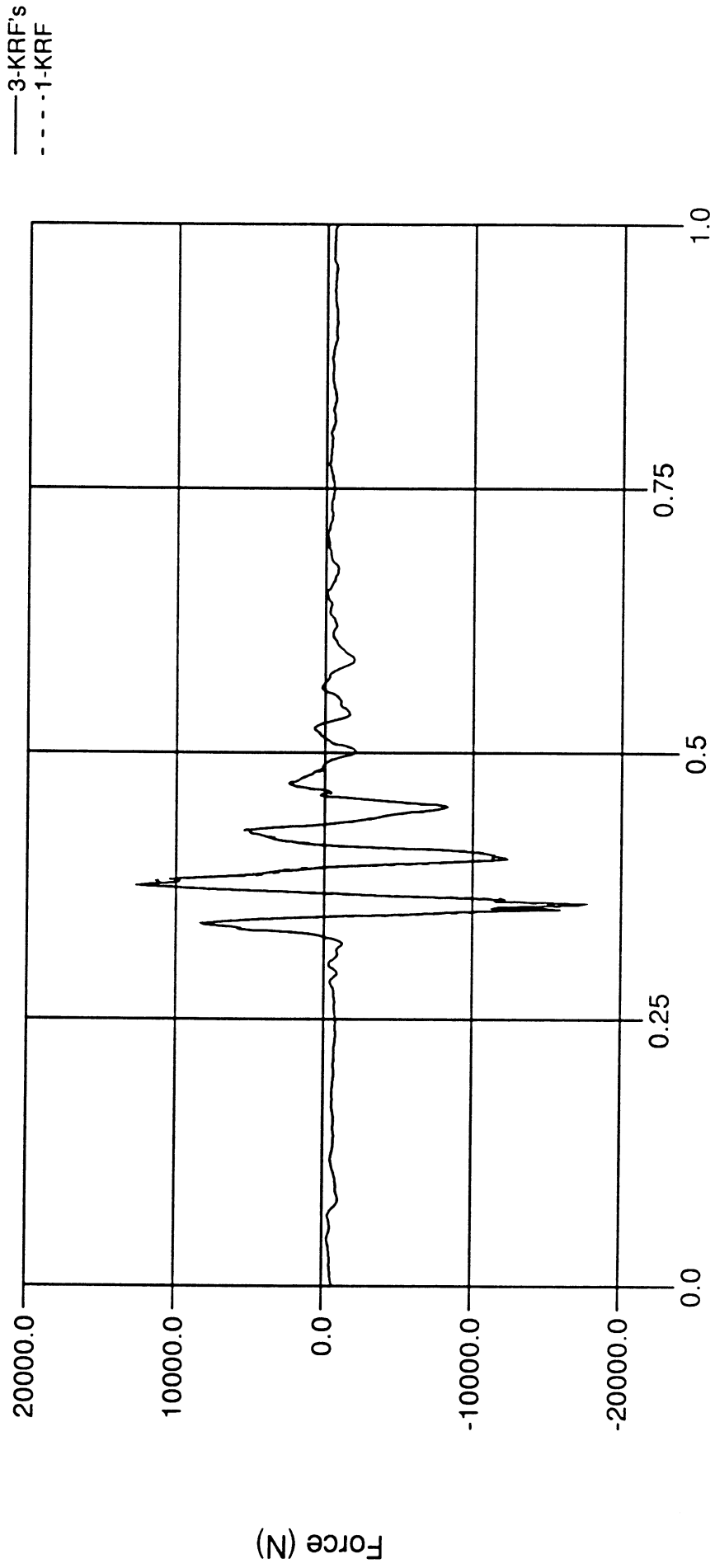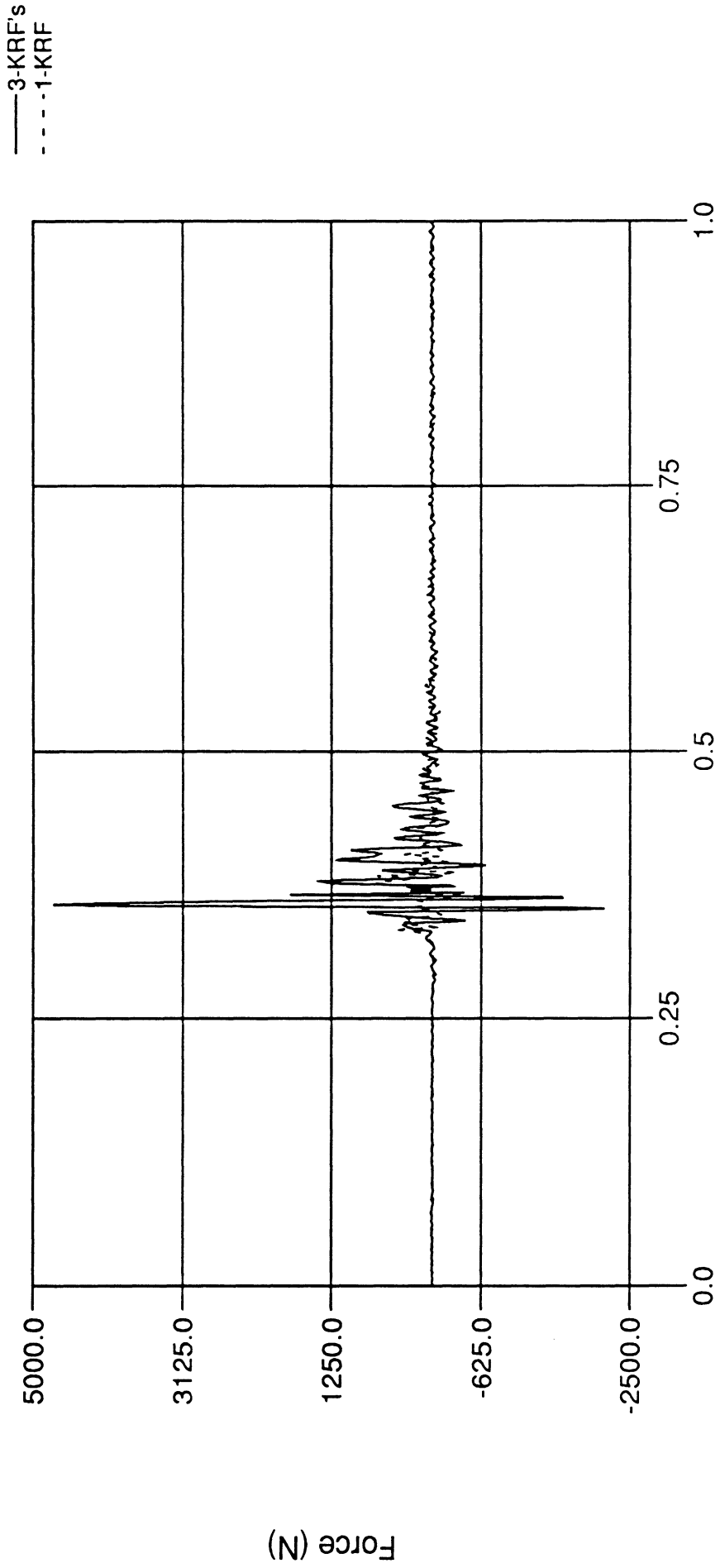
Rotation (radians)

Time (sec.)

Figure 64

DN101 Flexible LCA, Concentrated Mass Method

rotation of KRF's about global Y-axis

KRF 1
KRF 2
KRF 3

Rotation (radians)

0.25

0.0625

-0.125

-0.3125

-0.5

0.0   0.25   0.5   0.75   1.0
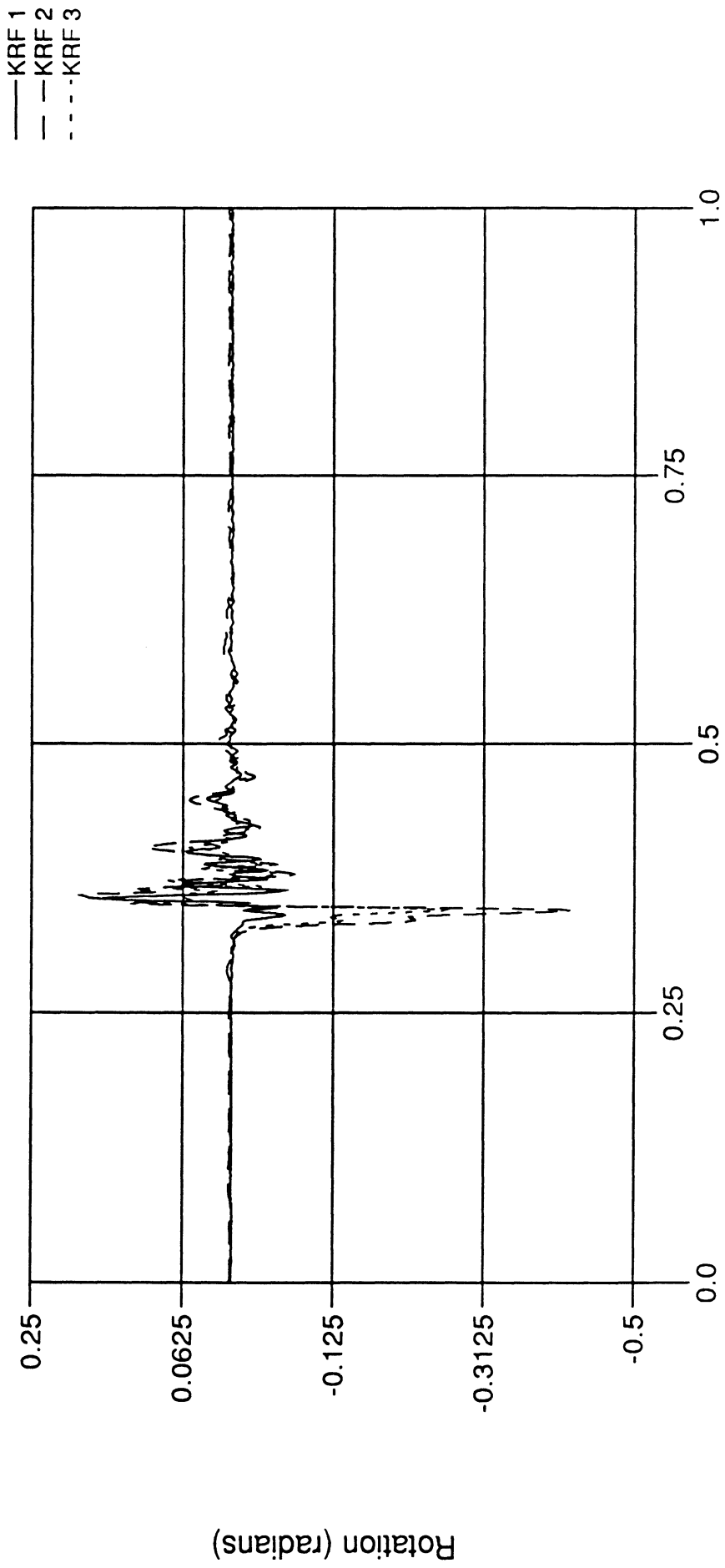
Time (sec.)

Figure 65

DN101 Flexible LCA, Concentrated Mass Method
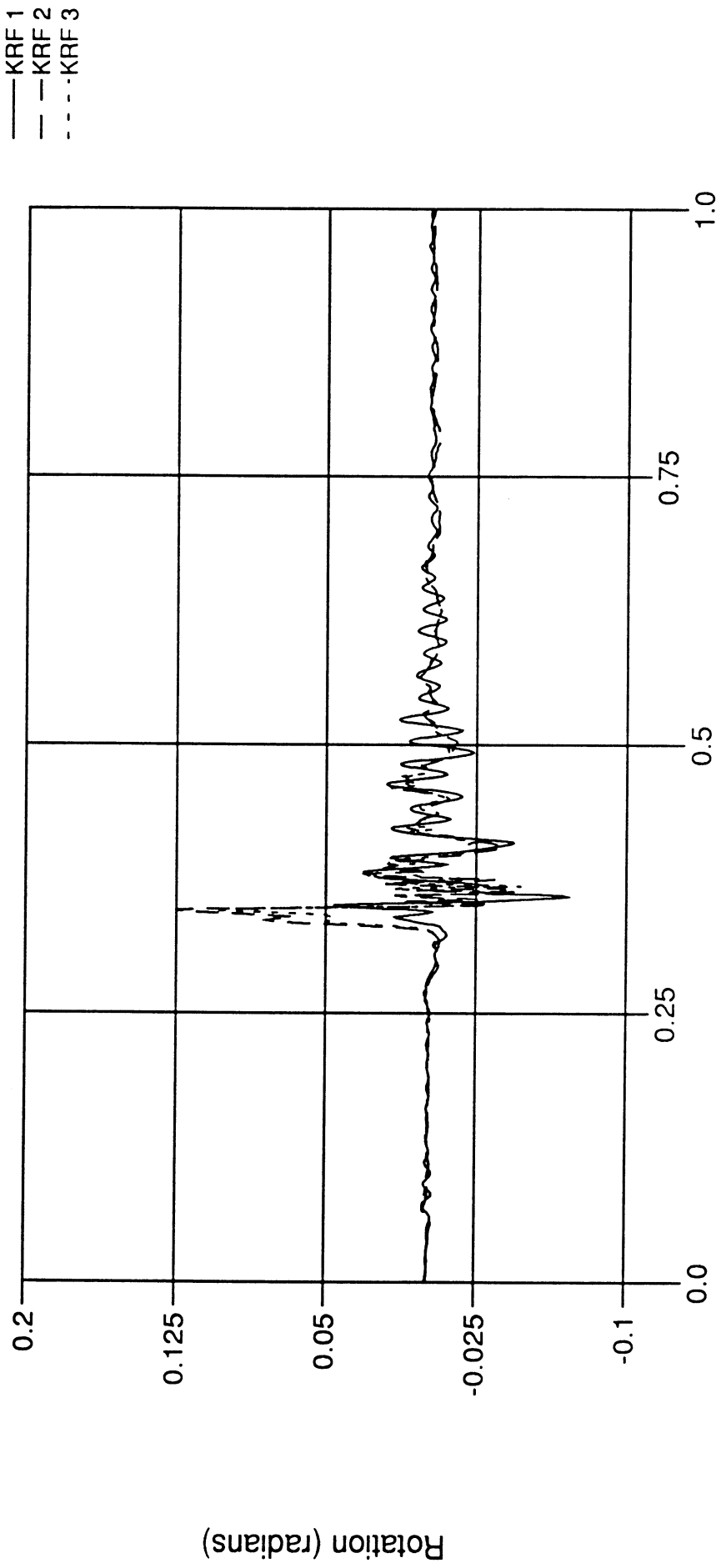
rotation of KRF's about global Z-axis

KRF 1
KRF 2
KRF 3

Time (sec.)

Figure 66

Rotation (radians)

DN101 LCA Mounted on Nonlinear Elastic Bushings

ball joint displacement along the fore-aft direction

flexible
- - - - rigid
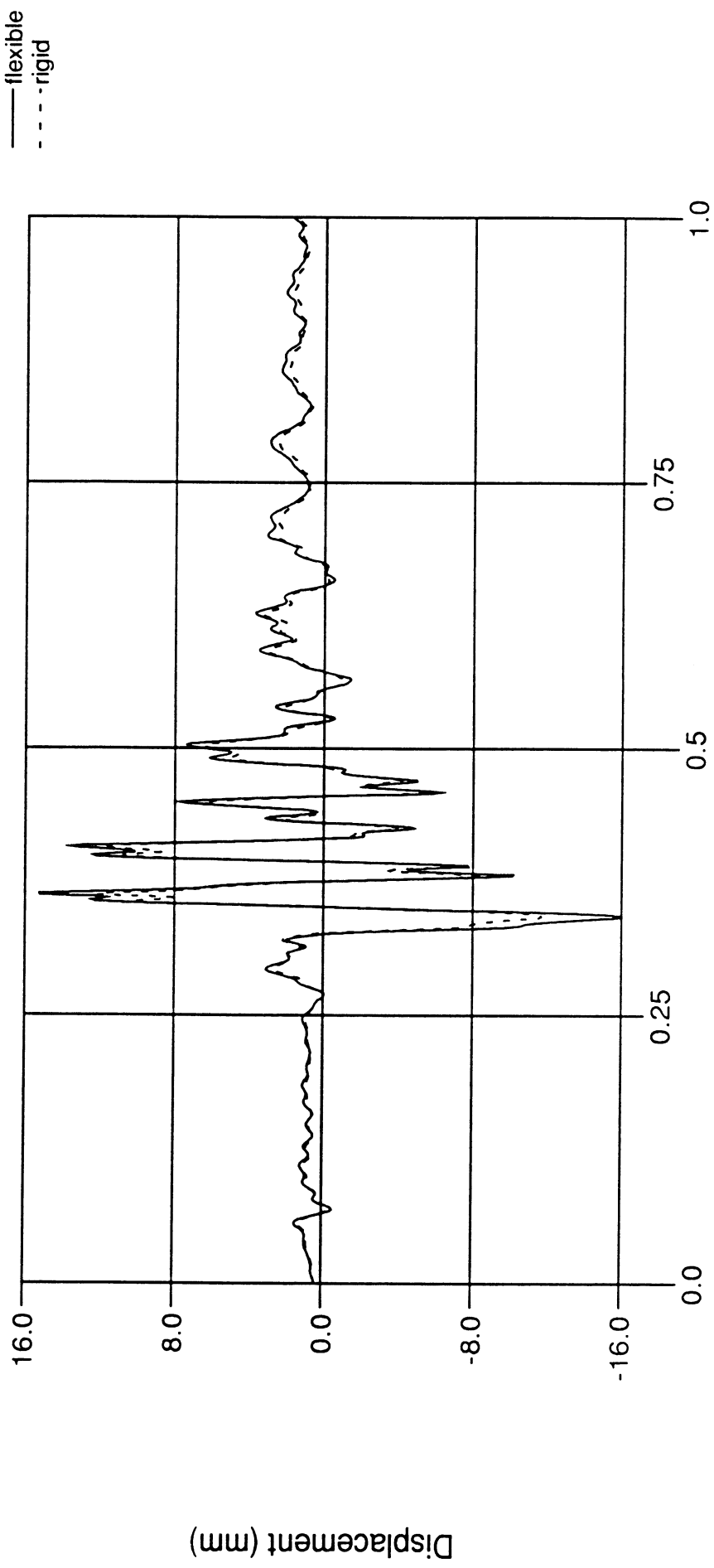
Displacement (mm)

Time (sec.)

Figure 67

DN101 LCA Mounted on Nonlinear Elastic Bushings
ball joint displacement along the lateral direction
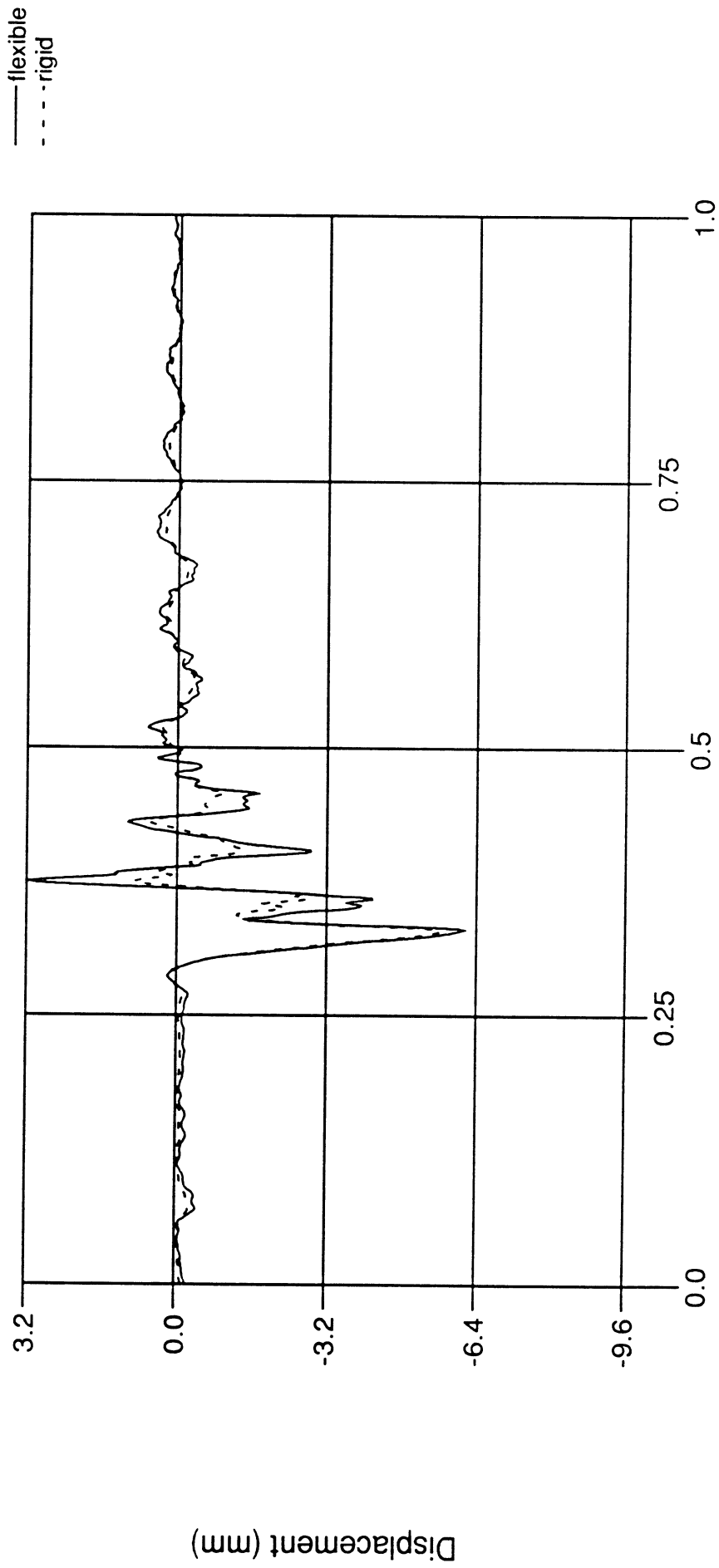
Time (sec.)

Figure 68

DN101 LCA Mounted on Nonlinear Elastic Bushings

ball joint reaction along the vertical direction
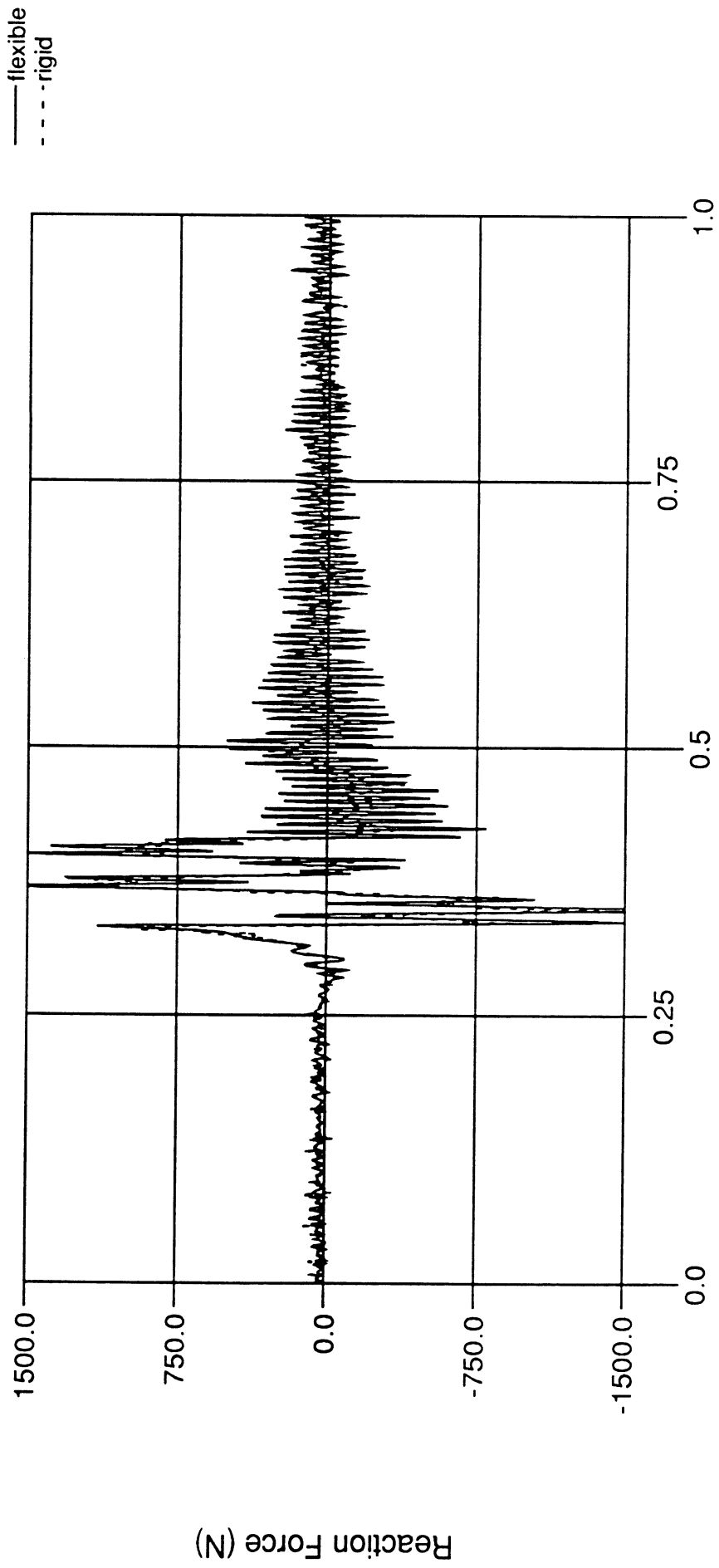
Reaction Force (N)

Time (sec.)

Figure 69

flexible

- - - rigid

DN101 LCA Mounted on Nonlinear Elastic Bushings
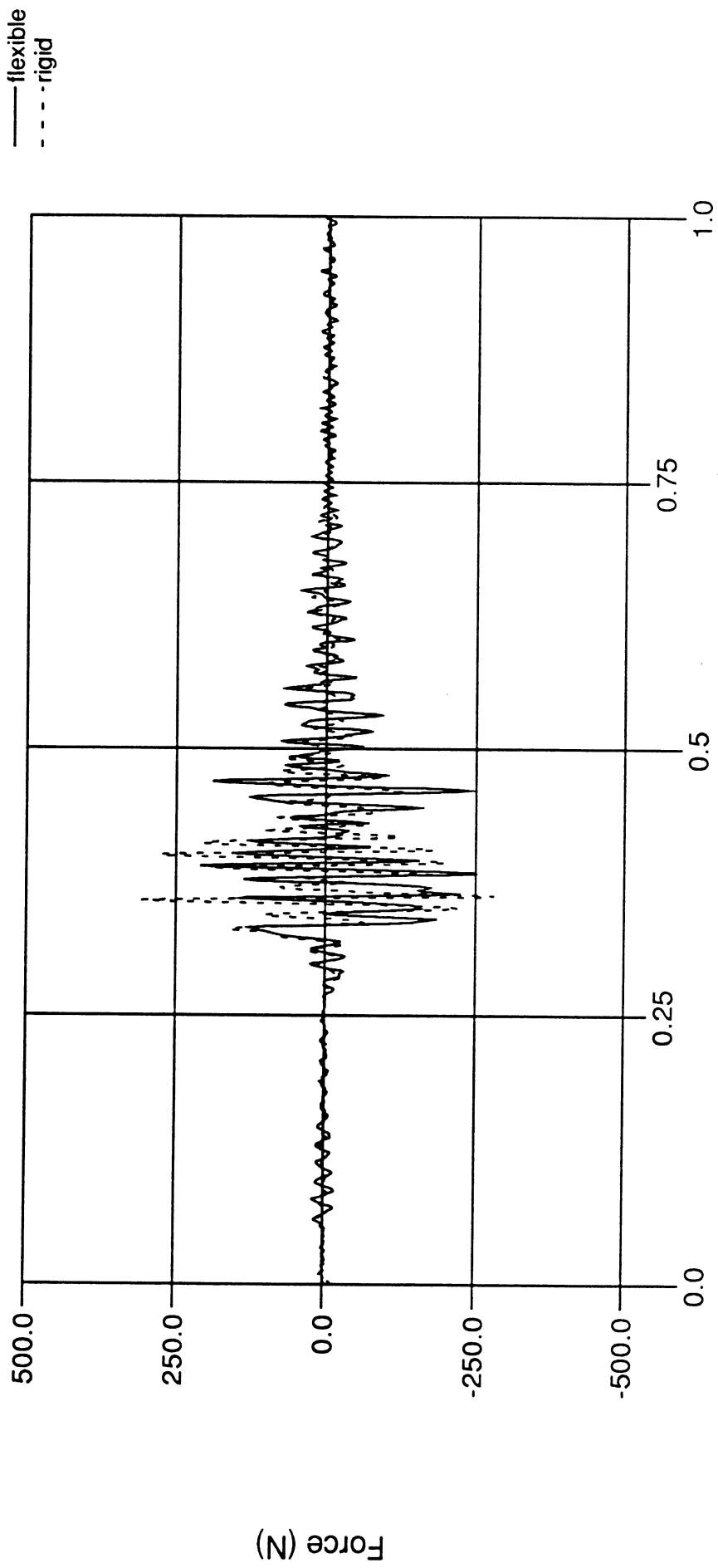
displacement of front bushing along local x-axis

Time (sec.)

Figure 70

Displacement (mm)

flexible

- - - rigid

DN101 LCA Mounted on Nonlinear Elastic Bushings
displacement of front bushing along local y-axis

flexible
- - - rigid
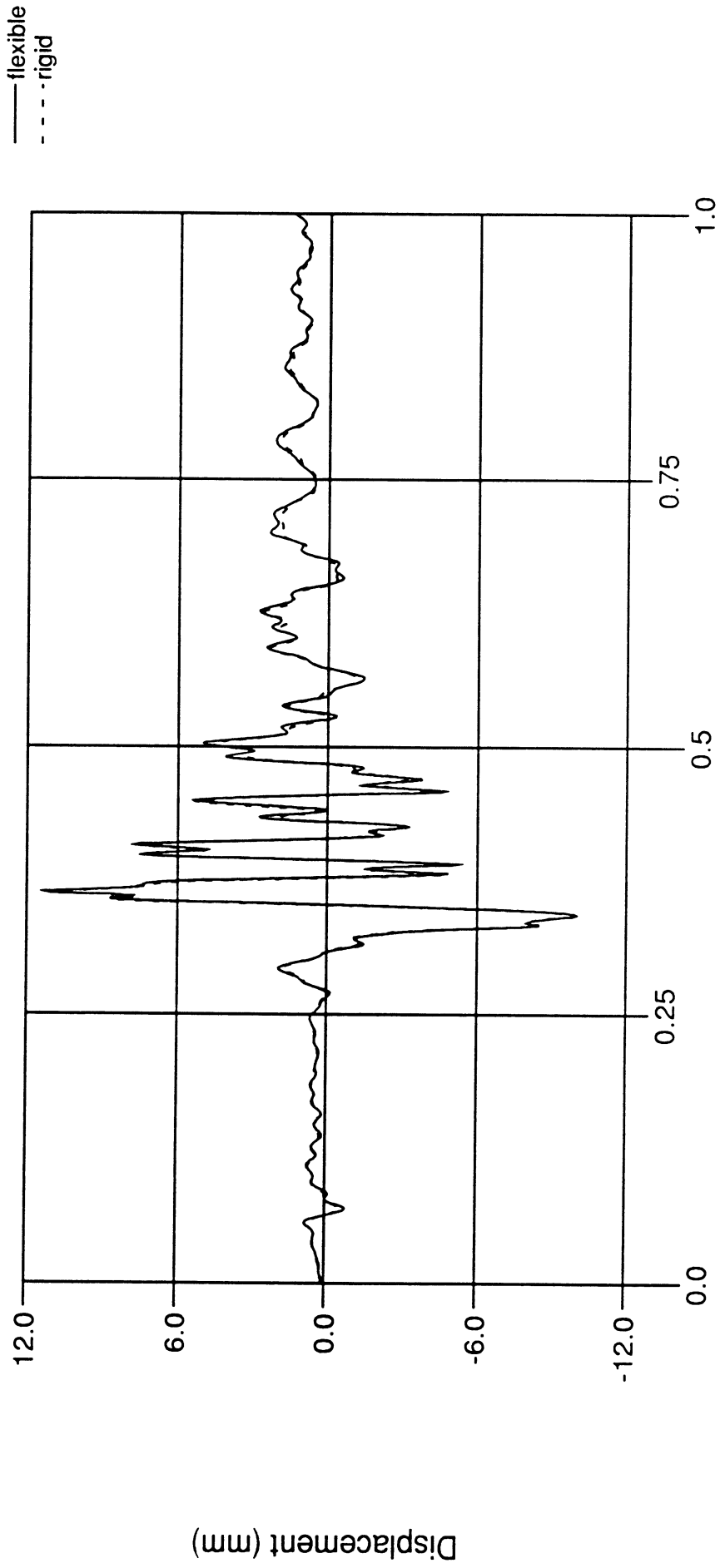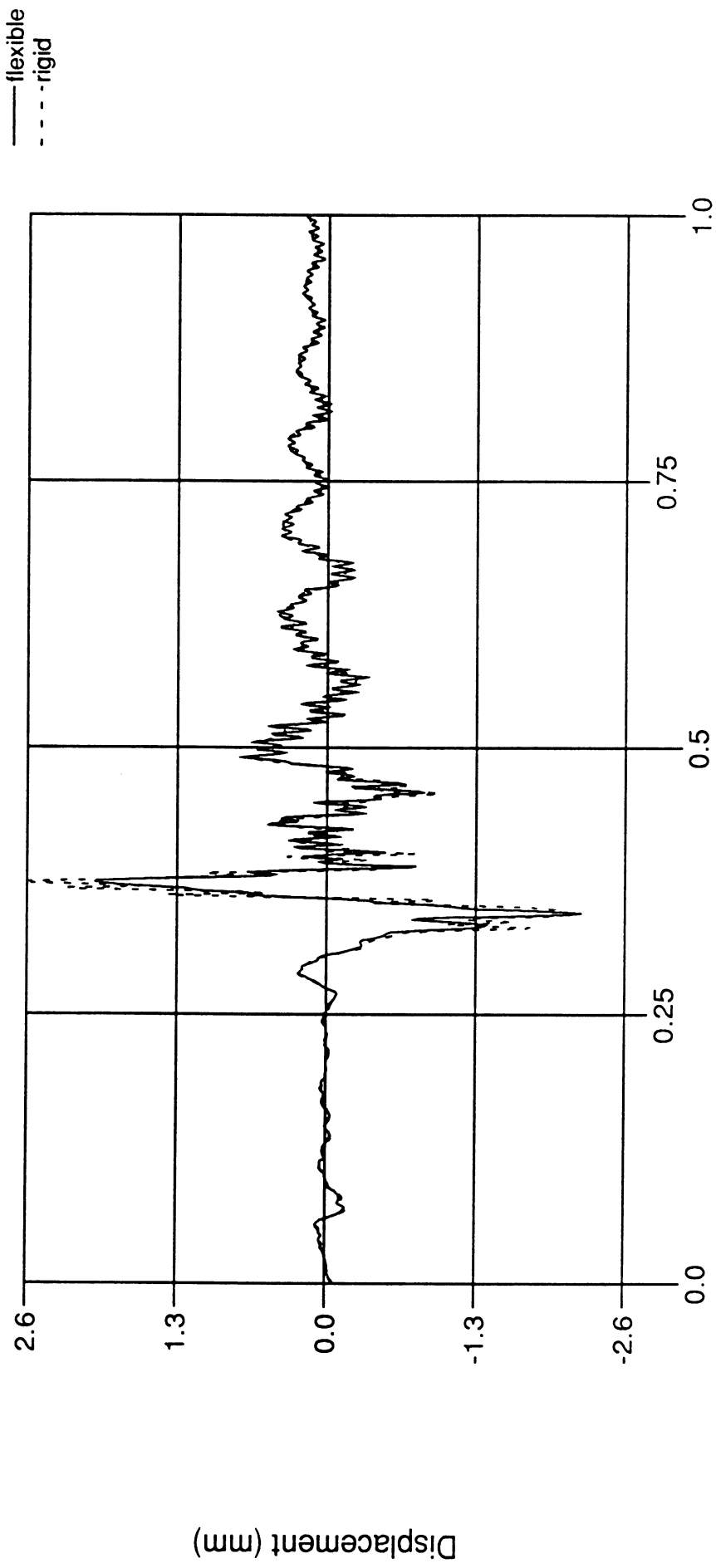
Displacement (mm)

Time (sec.)
Figure 71

DN101 LCA Mounted on Nonlinear Elastic Bushings

displacement of front bushing along local z-axis

flexible
- - - rigid

Displacement (mm)
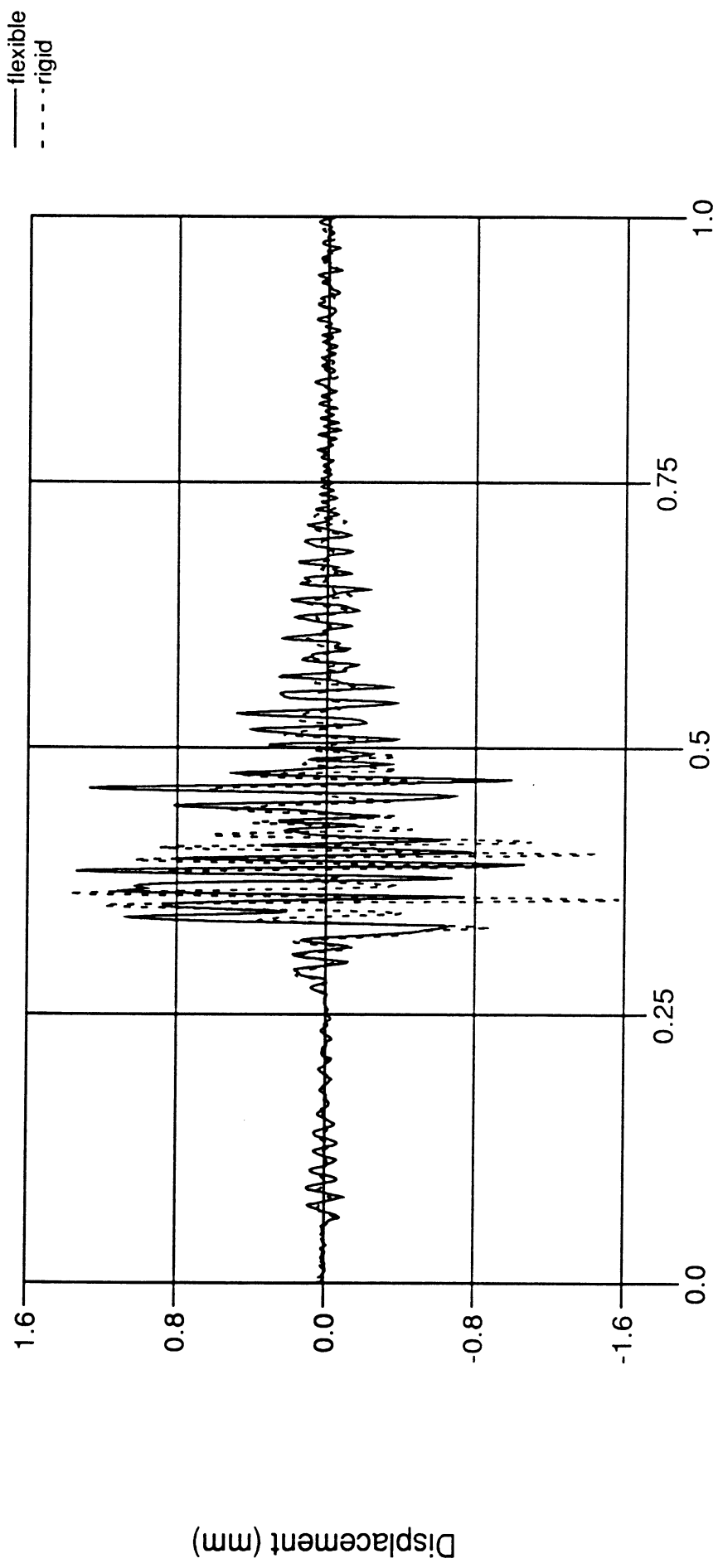
Time (sec.)

Figure 72

DN101 LCA Mounted on Nonlinear Elastic Bushings

front bushing radial force along local x-axis

flexible
- - - rigid
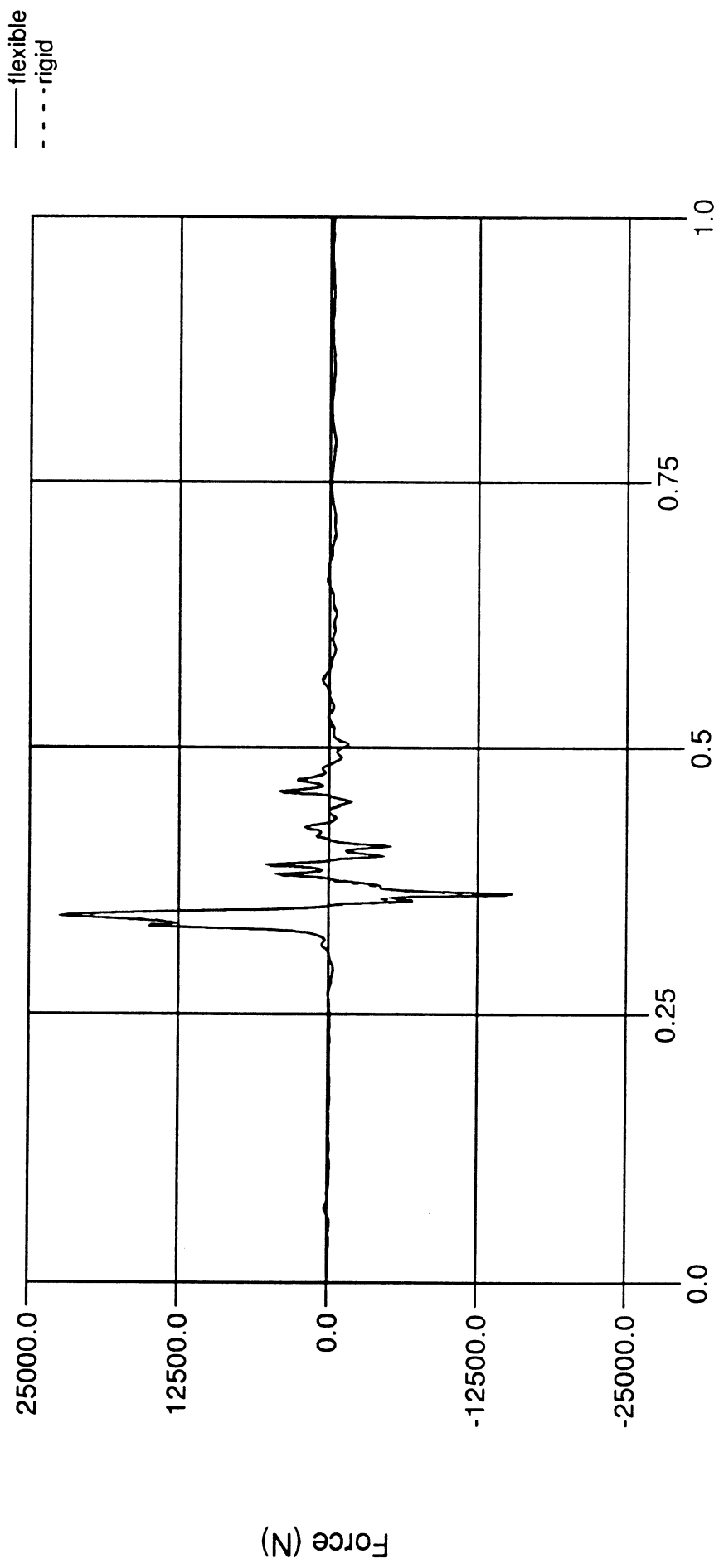
Time (sec.)

Force (N)

Figure 73

DN101 LCA Mounted on Nonlinear Elastic Bushings

front bushing radial force along local y-axis

flexible
rigid
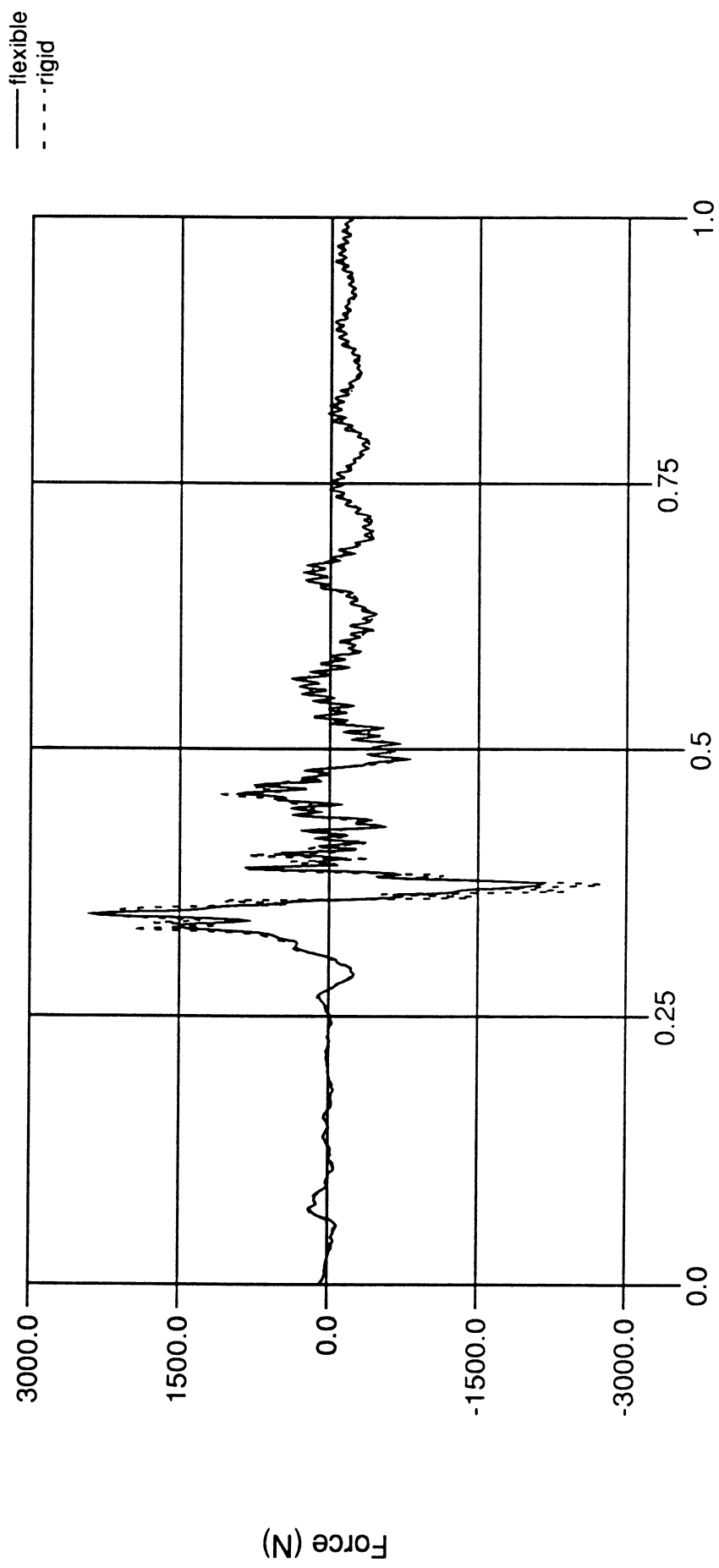
Force (N)

Time (sec.)

Figure 74

DN101 LCA Mounted on Nonlinear Elastic Bushings
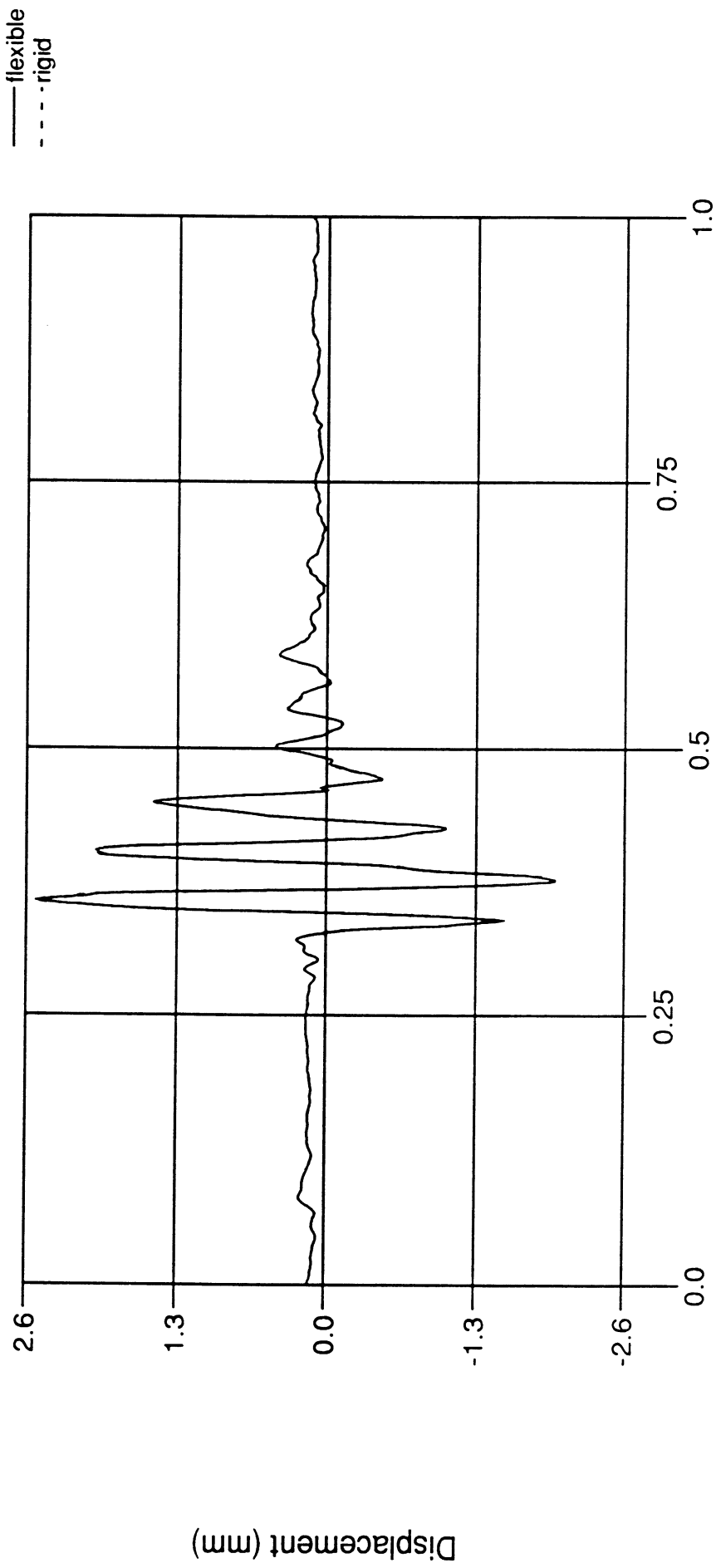
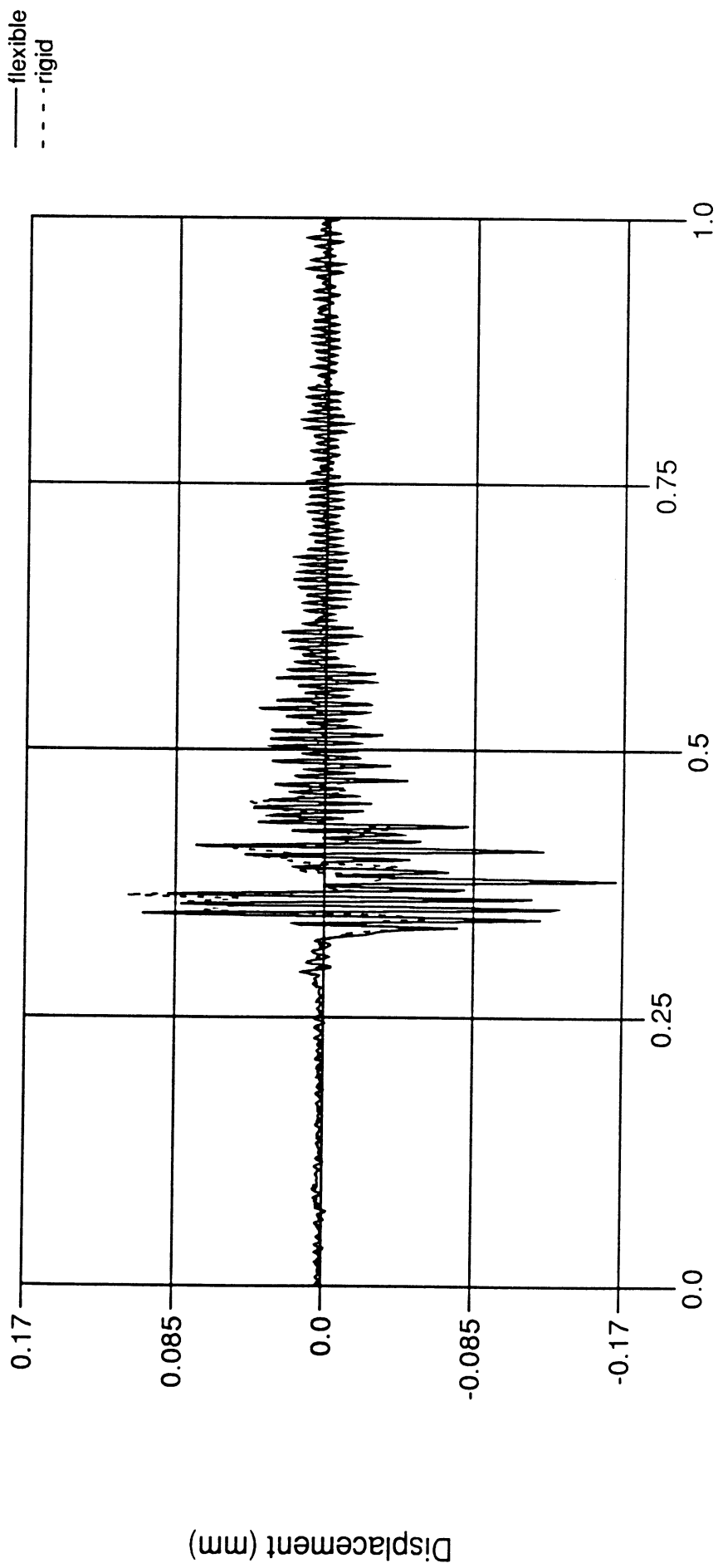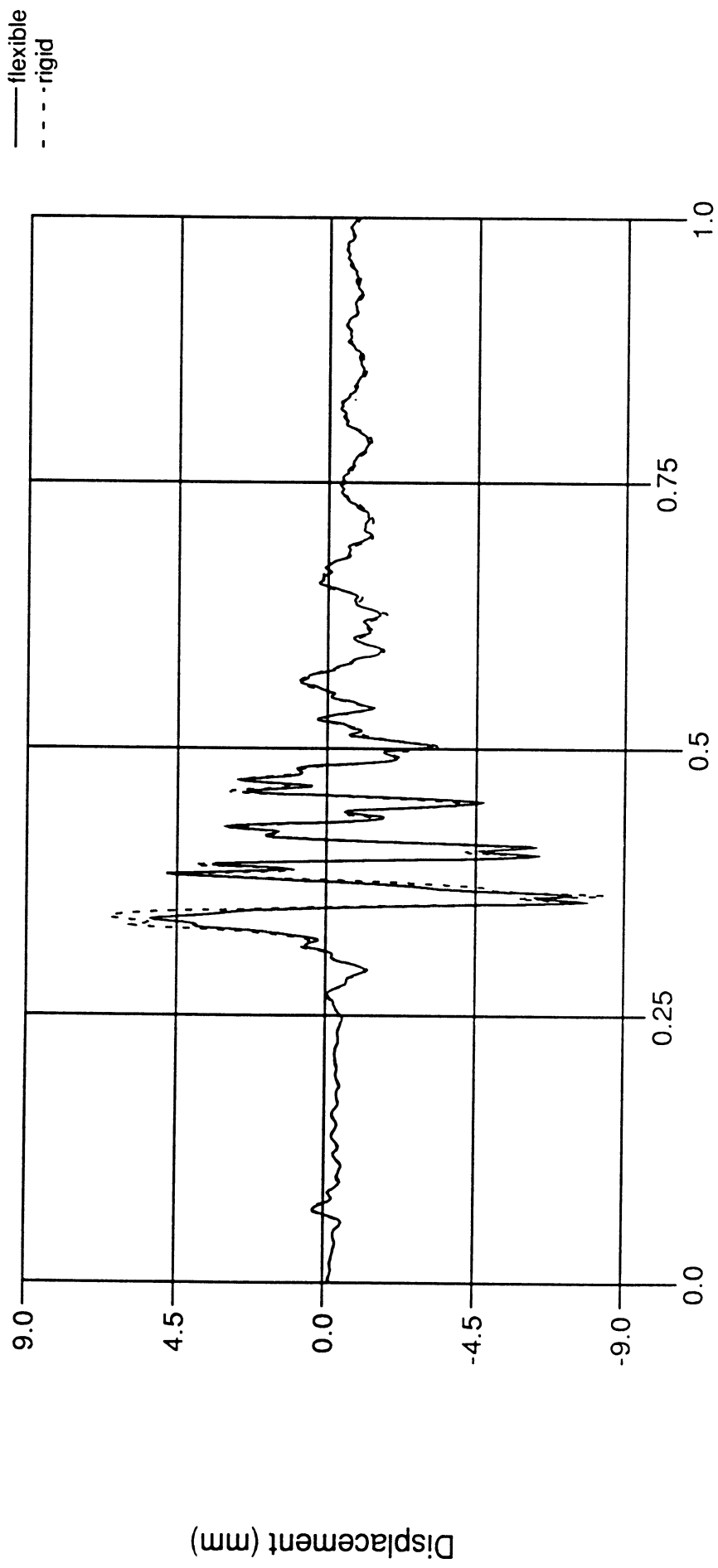front bushing axial force along local z-axis

flexible
- - - rigid

Force (N)

Time (sec.)

Figure 75

DN101 LCA Mounted on Nonlinear Elastic Bushings

displacement of rear bushing along local x-axis

Time (sec.)

Figure 76

Displacement (mm)

flexible
- - - rigid

DN101 LCA Mounted on Nonlinear Elastic Bushings

displacement of rear bushing along local y-axis

flexible
- - - rigid

Displacement (mm)

0.17
0.085
0.0
-0.085
-0.17

0.0   0.25   0.5   0.75   1.0

Time (sec.)

Figure 77

DN101 LCA Mounted on Nonlinear Elastic Bushings

displacement of rear bushing along local z-axis

Time (sec.)

Figure 78

flexible
- - - rigid

Displacement (mm)

DN101 LCA Mounted on Nonlinear Elastic Bushings

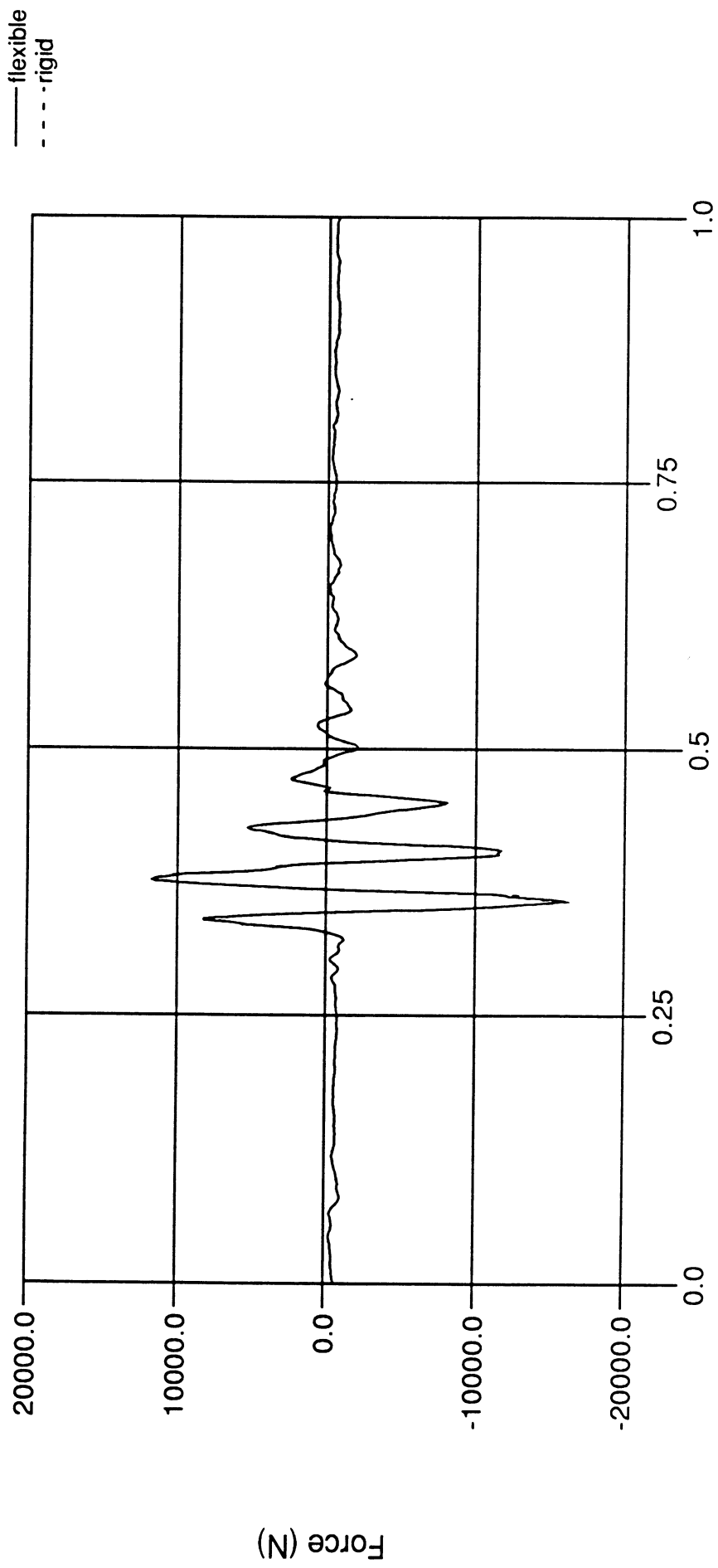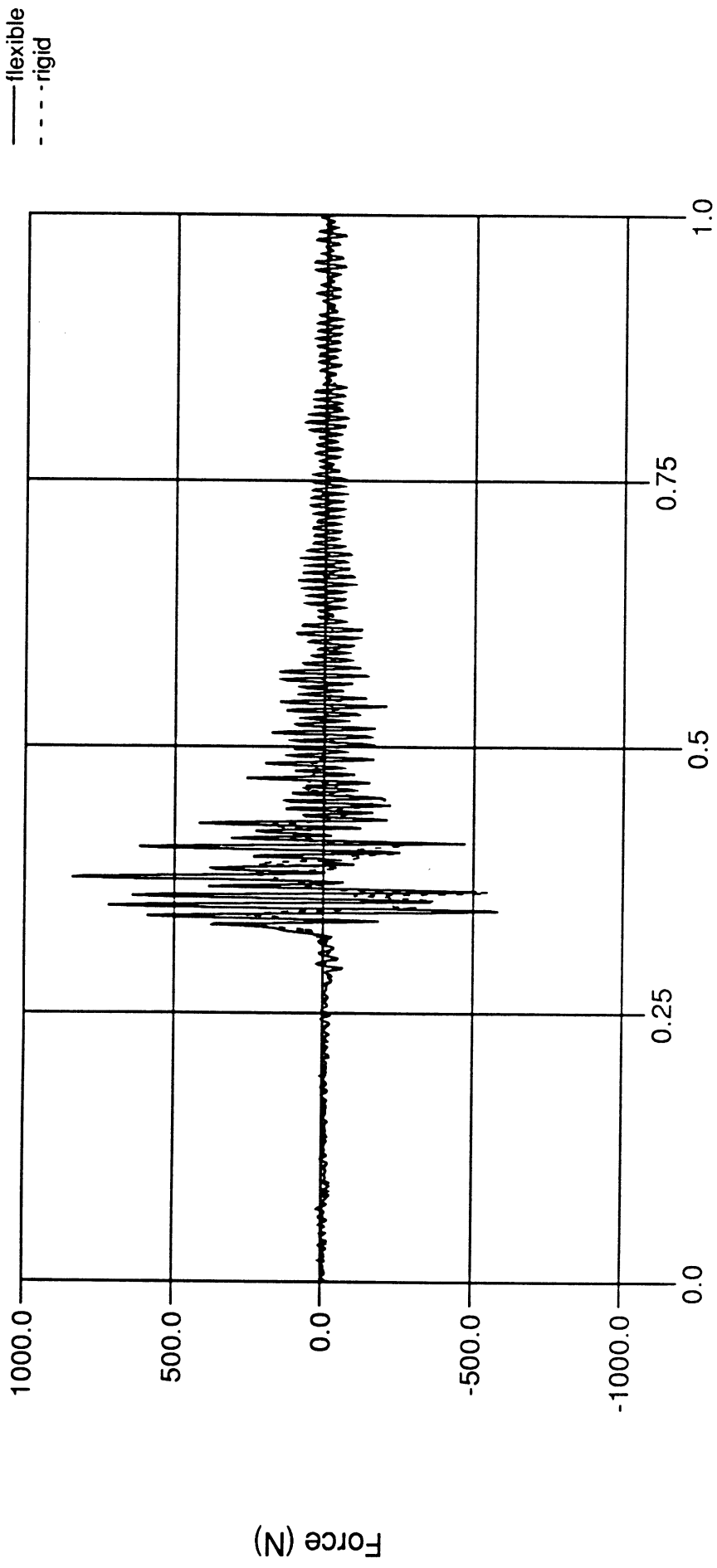rear bushing radial force along local x-axis
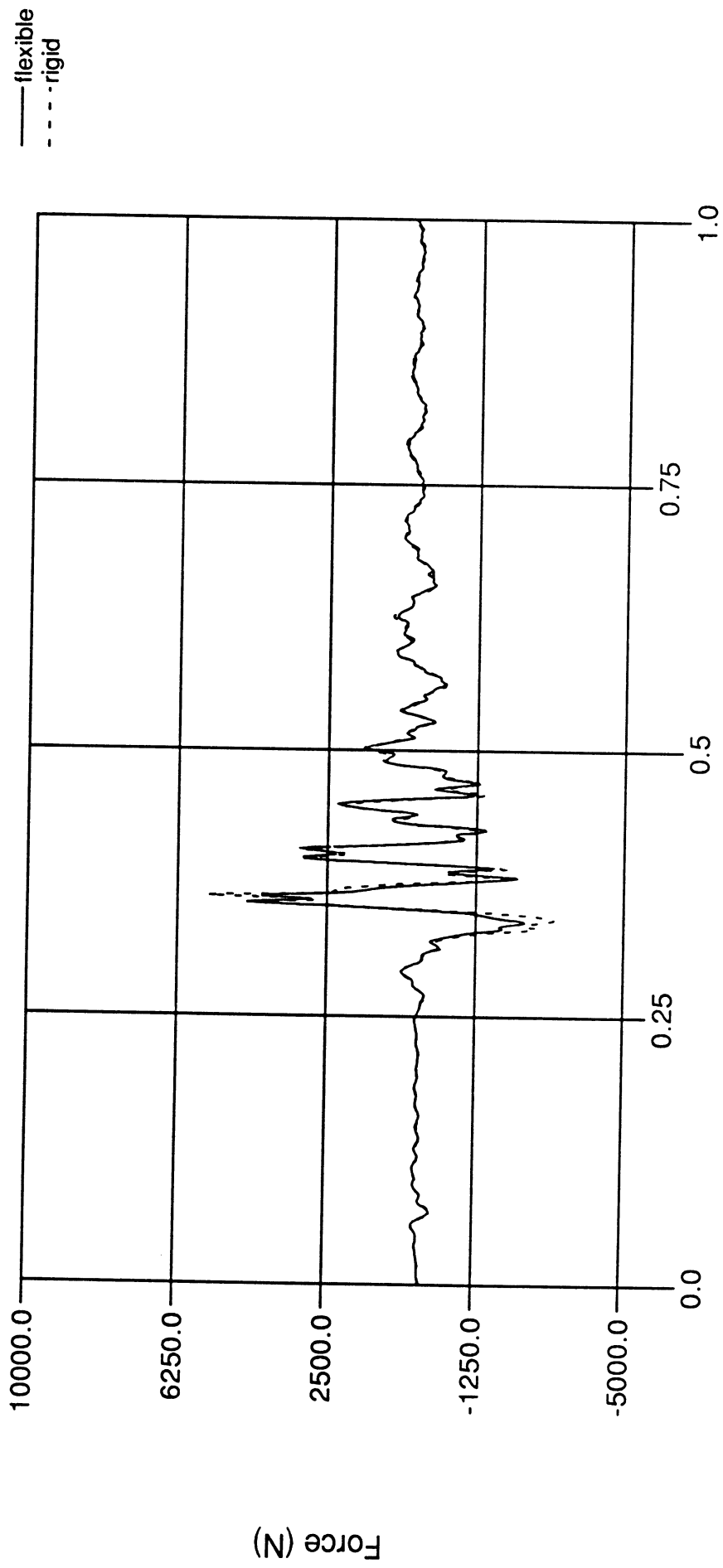
flexible
- - - rigid

Force (N)

Time (sec.)

Figure 79

DN101 LCA Mounted on Nonlinear Elastic Bushings

rear bushing radial force along local y-axis

Time (sec.)

Figure 80

flexible
- - - rigid

DN101 LCA Mounted on Nonlinear Elastic Bushings

rear bushing axial force along local z-axis

Time (sec.)

Figure 81

flexible
rigid

Force (N)